Università degli Studi di Genova - Physics Department

Doctorate in Physics
XXXVI Cycle

Ph.D. Thesis in Physics

STUDY OF THE IRRADIATION EFFECTS ON SUPERCONDUCTING FILMS OF IRON BASED SUPERCONDUCTORS

SUPERVISOR
Dr. Valeria Braccini

SUPERVISOR
Prof. Marina Putti

CANDIDATE
Iebole Michela

Academic Year 2023/2024

Contents

Chapter 1

Introduction

It is evident nowadays that the demand of energy is growing rapidly, therefore the need of a powerful and cost effective way to produce energy is strong. One appealing option of power generation could be found in fusion power.

Nuclear fusion plants generate electricity by using heat developed from nuclear fusion reactions; moreover, fusion processes require an environment suited to create and confine a plasma in which fusion can occur. In order to achieve fusion, the following conditions must be fulfilled: very high temperature to provoke high energy collisions, sufficient plasma particle density to increase the number of such collisions, and sufficient confinement time to hold the plasma in a defined volume. In order to contain, shape and hold the plasma, very high magnetic fields are needed, which are only possible to be reached with the use of superconductors.

Different superconductors can be used for the magnetic confinement, which have different performances, are at a different stage of technological development and present different peculiarities.

Iron-based superconductors have looked like a good candidate for this type of application since their discovery with LaOFeP in 2006 [1], and especially since 2008, when it became clear that superconductors with a high critical temperature could be obtained. What makes them so attractive is their high critical magnetic field, together with the competitive critical current density and relatively high critical temperature. Those properties make iron based superconductors good competitors of the well-established Nb_3Sn and the performing cuprates superconductors.

This thesis aims at the study and development of iron based superconductors for high field applications, in particular for fusion. It is financed by Eni SpA within the Joint Research Agreement with CNR. In particular the Joint Research Center on Fusion has as goal the development of skills and technological know-how, innovative techniques and validation methodologies for nuclear fusion, through the integration of skills of the CNR centers of excellence with Eni. CNR Spin Institute has as task the development of alternative superconductors for the magnetic confinement. In addition, this work was carried out in collaboration with the MIUR-founded PRIN Hibiscus project (High performance - low cost Iron BaSed Coated condUctorS for high field magnets).

Within these two projects I had the opportunity to collaborate with many researchers from different Italian Universities and Research Centres. In particular, the two projects were carried out in collaboration between the Department of Physics of the University of Genova and the CNR Spin Institute in Genova and Salerno, ENEA, University of Roma Tre, Politecnico di Torino and CNR IMM Institute in Catania.

I also had the opportunity to participate to a fellowship with Shibaura Institute of Technology (SIT), Japan, and won a paper-based project with the aim of using a new technique, Spark Plasma Sintering (SPS), to fabricate targets.

We focused on the development of Iron Based Superconductors (IBS) for high field applications and, among them, on the Fe(Se,Te) (11 phase), which is very interesting because it has the simplest structure and it also does not contain the poisonous Arsenic. It also has a good critical current density, around 10^6 A/cm2 for thin films.

This work can be summarised in two main objectives:

1. Make the phase Fe(Se,Te) useful for high field applications and therefore produce a real conductor from it.

2. Understand whether this Fe(Se,Te) coated conductors can be used in a nuclear fusion power plant.

Fe(Se,Te) phase is well suited to the production of a simple coated conductor. A coated conductor is a type of technical metallic template designed

for ReBCO (Rare-earth barium copper oxide), consisting of a metallic tape with a series of buffer layers and the superconducting film on top. The buffer layers are there to optimise the epitaxiality of the substrate to allow the growth of a perfectly oriented superconductor. This is necessary for ReBCO because the superconducting properties deteriorate if the grains are not oriented within 3 degrees in plane. Fe(Se,Te) also needs to be very well oriented to have good transport properties, but the condition is less strict: it is sufficient if the grains are oriented within 9 degrees. Technical substrates designed for ReBCOs have been used to produce Fe(Se,Te) coated conductors and other iron-based conductors with optimum results. Our aim is to reduce the number of buffer layers to one when making a Fe(Se,Te) coated conductors, to reduce complexity and therefore cost of the final conductor.

If the final aim is to make magnets for plasma confinement, it will inevitably be placed very close to it and will therefore be bombarded by a lot of the radiation the plasma produces. We will focus on the effects that different types of radiation can have on Fe(Se,Te).

The thesis is organised as follows.

The first chapter begins with a brief introduction to the state of the art in nuclear fusion reactors, both with regard to the niobium-based superconductors (NbTi, Nb_3Sn) and the innovative high-temperature superconductors. A brief excursion into iron-based superconductors is then presented, starting with their discovery in 2008; their characteristics and properties are reported. Next, the state of the art of the Fe(Se,Te) phase, which is the phase I studied in this thesis, is reviewed. Focusing on why it might be interesting for applications, and in particular why one might attempt to make a simple coated conductor out of it. Finally, a section reports on the progress made on this phase over the last few years at the CNR Spin Institute.

The second chapter describes the steps necessary to move towards to the fabrication of a coated Fe(Se,Te) conductor. The target preparation (through classical method, used at the CNR Spin Institute, and spark plasma sintering, implemented at the SIT) is presented. It then focuses on the preparation of thin films on different substrates. The ultimate goal was to be able to deposit this material on metal templates with a single buffer layer. First, the properties of the phase on the simplest possible substrates (single crystals) are described. Then the study of the deposition on the buffer layer

chemically grown on single crystals is presented. The last part is the study of the deposition of Fe(Se,Te) on a metal tape covered by the buffer layer. ENEA was responsible for the deposition and characterisation of the buffers deposited both on single crystals and on metal tape. The structural and superconducting characterisation of the samples was carried out partly at the SPIN, partly at the Università di Genova and partly at ENEA. Finally, the TEM characterisation was carried out at IMM. My role has been in the deposition of the films on all the different substrates and in the characterization of some of them.

The third chapter summarises the effects of irradiation on iron-based superconductors, depending on the type of particle used. A special focus is given to the literature on Fe(Se,Te) irradiation.

The fourth chapter presents the different types of irradiations that we have carried out on our thin films. In particular, I personally took part in some of the irradiations described, always in collaboration with the Politecnico di Torino, which also took care of the simulation study and the magneto-optical analysis. The best way to simulate the effects of irradiation in a reactor is certainly to irradiate the samples with neutrons, but it is difficult to obtain sufficient energies and fluxes, so it is often necessary to resort to irradiation with charged particles, at different energies. My samples were irradiated with both charged particles, such as protons or gold ions, and with neutrons. In order to better study the effects of irradiation on the structural properties, I took the samples for a measurement run at the Bessy II synchrotron in Berlin. The transport characterisation of the irradiated samples was carried out partly at the CNR Spin Institute in Genoa, partly at the CNR Spin Institute in Salerno and partly at the ENEA laboratories.

Finally, the conclusions of my work are presented.

Chapter 2

Iron Based Superconductors for Fusion applications

2.1 Superconductors for fusion: state of the art

Superconductors technology has always been a part of the dream of achieving nuclear fusion by magnetic confinement, pre-dating even the discovery of the best-performing magnetic confinement design, the tokamak, in the 1960s [2]. Steady progress has been made in the use of superconductors in a range of superconducting magnetic confinements device, starting with **T-7** in 1979, shown in figure 2.1, and culminating with the construction of the ITER tokamak.

ITER is he world's largest tokamak, a magnetic fusion device designed to prove the feasibility of fusion as a large-scale and carbon-free source of energy based on the same principle that powers the Sun and stars. The main goal of ITER is the investigation and demonstration of burning plasmas. ITER will also test the availability and integration of technologies essential for a fusion reactor such as superconducting magnets, remote maintenance, and systems to exhaust power from the plasma [3].

The confidence in fusion by magnetic confinement is giving rise to a series of proposals for post-ITER machines, that will be capable of producing net nuclear power. We can divide them into two categories, the first named **big machines**, which are DEMO-type fusion reactors based on the ITER design

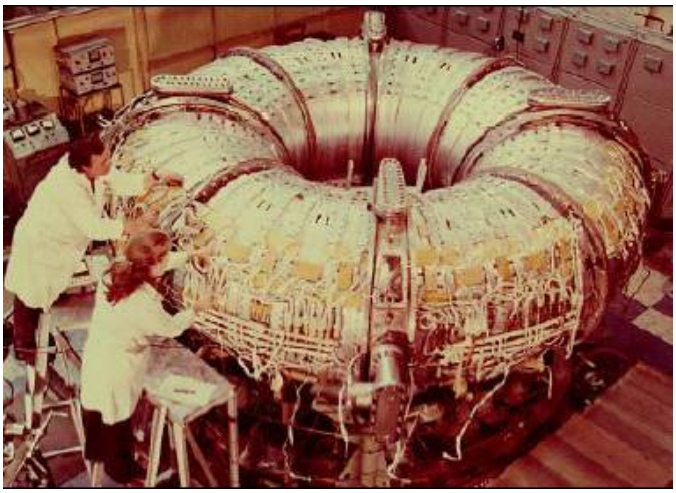

Fig. 2.1: T-7 tokamak, Kurchatov Institute,Moscow, 1979, with NbTi TF coils [4].

concept and technologies. The second category is the **compact machines**, based on more advanced superconductive technology.

The first generation of magnetic confinement devices to use superconductivity was based on $NbTi$ and Nb_3Sn strand technology. T-7 Kurchatov (1979, figure 2.1) had $NbTi$ coils, following prototypes, such a the Mirror Fusion Test Facility (MFTF) (1984), used a combination of $NbTi$ and Nb_3Sn coils while the latest generation, starting from TRIAM-1M Kyushu University (1986) uses Nb_3Sn coils [5].

Figure 2.2 shows three of the most common forms of magnetic confinement devices. The most famous, which is also the one with the best plasma confinement performance, is the tokamak, with its three basics sets of coils: the toroidal field coils **TF**, the central solenoid coils **CS** and the poloidal field coils **PF**. The stellaretor appears in two forms, one with descrete but three-dimensional coils and the other with largely toroidally wound spiral coils [5].

The main driver of magnetic confinement for fusion is of course the plasma physics and confinement. Modeling of plasma core suggests that there are windows for 'compact' machines, which can exploit the high field or very low aspect ratio (or both) to achieve a higher power density than the ITER-like machines. Progress in high temperature superconductors (HTS) has made available a new material with improved operational ranges in temperature and field.

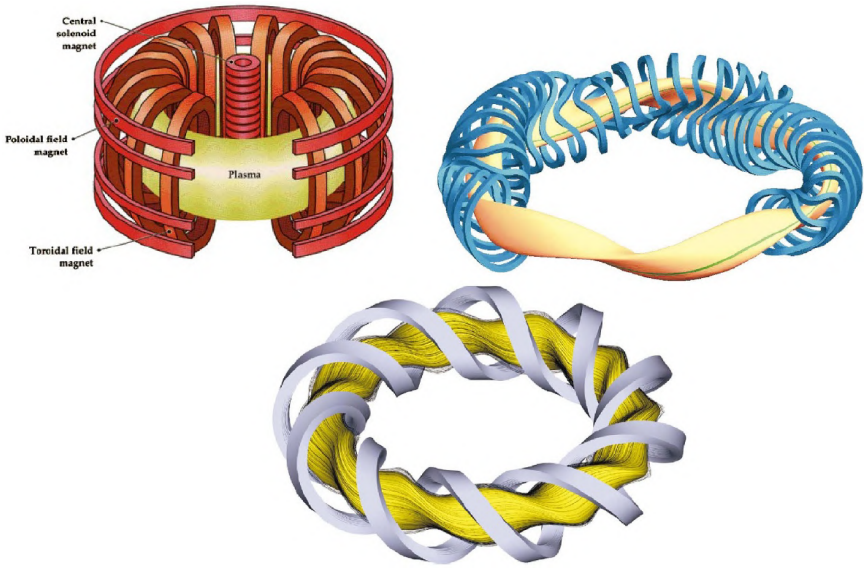

Fig. 2.2: Diagrams of the coil systems needed for magnetic confinement. Top left: general tokamak, top right and below: two different forms of stellarator. [5].

From the 1960s to the 1990s, the triple product of tokamaks increased by four order of magnitude. As the name suggests, the triple product is the product of three attributes of a fusion plasma:

- η the density of ions in the plasma (ions/m2);
- T the temperature of those ions (keV);
- τ_E the energy confinement time (seconds) [6].

By the 1990s, improvement in the triple product stalled, as copper magnets ran into resistive power-loss limits, and low temperature superconductors (LTS) critical field limits necessitated ever-larger and more expensive devices. This was true for both tokamak and non-tokamak devices. The advent of the commercially available REBCO HTS, capable of maintaining large critical current at high magnetic fields is breaking this stalemate. REBCO is particularly impactful because the triple product scales with the cube of the on-axis field, allowing for energy break-even in compact devices.

Today, at least three private fusion companies are leveraging these benefits across multiple device classes. They include standard aspect ratio tokamak, low aspect ratio, or spherical, tokamak, and stellarators.

REBCO has certainly proven to be attractive for the construction of the next generation of fusion power plants, but several critical challenges remain for REBCO tape to make fusion its killer application. For example, AC losses are still a significant challenge for REBCO coils, but certainly one of the main problems is the still very high cost of manufacture: the impact of higher volume production on cost is beginning to be felt, but significant further reductions in coil cost will be required before widespread application to commercial fusion can be achieved. Furthermore, to realise their potential impact on fusion devices, HTS magnets need to be scaled up to high fields (more than 20 T on-coil) and large bores (greater than 1 m). This poses several structural and integration challenges, including the management of large Lorentz forces, strip quality assurance, cryogenics and fabrication. To realise their potential impact on climate change, these innovations will then need to be scaled up to production volumes in excess of thousands of magnets per year. Continuous high volume mass production of high field magnets is a new challenge that will require new materials, manufacturing, integration and testing methods.

Commonwealth Fusion Systems (CFS) and the Massachusetts Institute of Technology (MIT) are jointly developing a high field compact tokamak called SPARC ("Smallest/Soonest Possible ARC"), which aims to achieve fusion energy break-even. Using the same conservative plasma physics basis used to design ITER, SPARC will use high-field HTS magnets build with today's commercially available REBCO tape, and achieve an on-axis magnetic field of 12.2 T with a major radius of 1.85 m. CFS will follow SPARC with ARC, a commercial fusion pilot plan, to be commissioned in the early 2030s (see figure 2.3).

The TF model coil will be a high-field, DC, large-bore magnet, while the CS model coil will be a high-field, fast ramping magnet. SPARC is challenging the industry to improve costs and volumes, and ARC will implement demountable magnets so that its vacuum vessel can be periodically replaced.

Spherical tokamak (STs) offer significant advantages for commercial fusion power plants: higher thermal power per unit plasma volume and significant bootstrap current. These benefits enable smaller, more efficient machines to be developed, accelerating development timescales and reducing recycled power. Progress in understanding the physics of STs is continuing around

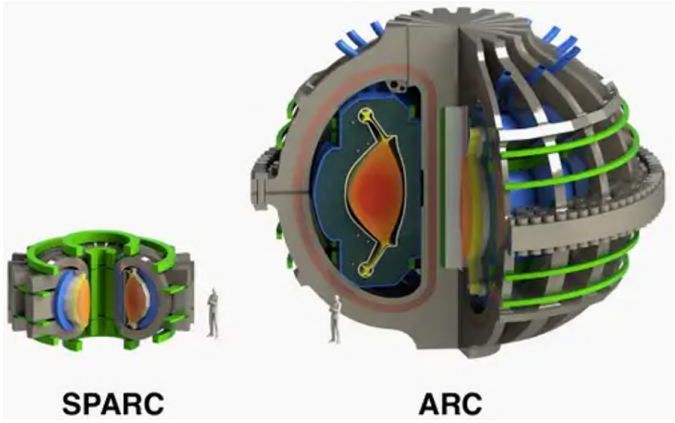

Fig. 2.3: SPARC and ARC scheme comparison. [7].

the world on experimental devices. The recent commercial availability of high-performances REBCO-coated conductors for multiple suppliers makes a high-field ST feasible at smaller scale than a conventional aspect ratio tokamak using LTS. [5]

REBCO coated conductors are promising candidates to make high field, low aspect ratio tokamak possible. In these reactors, a strong magnetic field is needed to confine the plasma, but the physical space for the magnet winding is restricted. The thickness of neutron shielding is also limited by design, cost and lifetime considerations, meaning that the superconductor will inevitably be exposed to higher fluxes of fast neutrons than in larger tokamaks. It is therefore important to consider the effect oh high energy neutron irradiation on the superconducting properties of coated conductors.

The fusion reaction between deuterium and tritium in a tokamak plasma emits neutrons with energies between 12 and 20 MeV, therefore fusion relevant neutron spectra need to contain a significant fraction of high energy neutrons. Since there are currently no sources of neutrons of an appropriate flux with these energies, previous experimental work has focused on determining the effects of irradiation damage on the superconducting properties of CC using fission spectrum neutrons, heavy ions or light ions/protons. These experiments show, except in low magnetic fields, that there is an initial improvement in J_c with increasing irradiation dose, followed by a decrease in both J_c and T_c and eventual complete loss of superconductivity.

Mimic the damage that will be experienced by HTS coil windings in future

fusion reactor magnets, REBCO Coated Conductors have been ion irradiated *in-situ* by W Iliffe et al [8] using energetic ions as a proxy for fast neutrons. A linear decline in T_c with dose rate is observed; moreover, irradiated samples showed a systematic degradation in self-field J_C values. An interesting observation in these experiments is an improvement of both T_c and I_c values of the cold-irradiated samples after extended annealing at room temperature, an improvement that is not mirrored in the room temperature irradiated samples. This suggest that damage-recovery processes that did not occur during the timeframe of the *in-situ* experiment can occur during the *ex-situ* experiments or once cold irradiated samples are annealed for extended periods at room temperature.

Following these observations, experiments to measure superconducting properties *in-situ* during ion beam irradiation were carried out by the same group, using 2 MeV He^+ irradiation. Evaluating the critical current density during *in-situ* irradiation, it is evident that the properties of REBCO CC are strongly affected during irradiation. This is even clearer when comparing the J_c during the irradiation (beam on, black line in figure 2.4) and immediately after the beam has been switched off (blue line) [9].

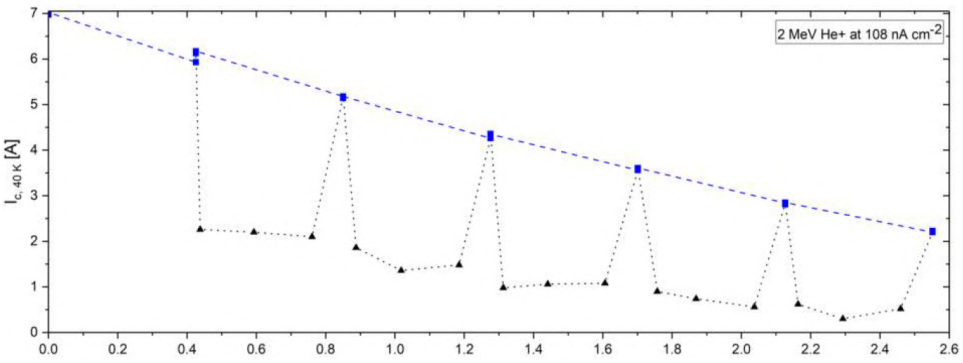

Fig. 2.4: Critical current measurements during *in-situ* irradiation, both with beam on (black) and immediately after turning it off (blue) [9].

Several irradiation experiments carried out on REBCO superconductors (single crystals, thin films and coated conductors) have shown that these materials are very sensitive to radiation, which calls into question their suitability for use in fusion devices.

My work is focused on an alternative to REBCO-type superconductors for fusion applications, proposing to produce coated conductors with simpler

structures, using the iron-based superconductors (IBS). Such materials, although their critical temperatures are lower than HTS, show very high critical fields below 20 K as shown in figure 2.5, and are therefore potentially promising for fusion applications. My aim is to demonstrate the feasibility of a much simpler coated conductor with the use of iron based superconductor, to reduce cost production and to make scalability to an industrial process more advantageous.

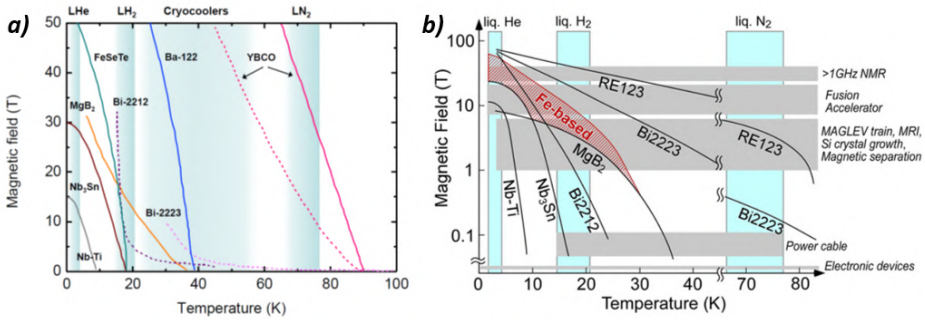

Fig. 2.5: (a) Comparative $H-T$ phase diagram for representative cuprates, Fe-based superconductors (IBS), and conventional superconductors, where the solid and dashed lines show, respectively, $H_{C2}(T)$ and $H_{irr}(T)$ parallel to the *c-axis* [10]; (b) $H-T$ graph comparing field and temperature application areas of IBS, cuprates and niobium-based superconductors.

2.2 Iron Based Superconductors

For years it was believed that iron, given its high magnetic moment, would have been harmful to the emergence of superconductivity, basically for the competition between the ordering of electron spins and the dynamic formation of Cooper pairs. In 2008, the discovery of Iron Based Superconductors (**IBS**) by the Hosono group in the Tokyo Institute of Technology marked the coming of the 'iron age' of high-Tc superconductivity (after the 'copper age' marked by cuprate superconductors). IBS were discovered in the course of exploration of magnetic semiconductors as an extension of research on transparent p-type semiconductors. The study was about LaT_MPnO (T_M= 3d transition metal, Pn= pnictogen), which has the same crystal structure as LaCuOCh (Ch=chalcogen) composed of an alternate stack of $(\mathrm{Cu}Ch)^-$ and $(\mathrm{LaO})^+$ layers. This first compound [1], however, presented very low T_c, and had been recognized by only a small community, interested in ex-

otic new superconductors. High-T_c superconductivity was discovered for $LaFeAsO_{1-x}F_x$ with T_c=26 K (x=0.08) in February 2008. Then, a T_c of 43 K was reached under a high pressure of 4 GPa, in April 2008. It was widely believed that elements with a large magnetic moment were harmful to the emergence of superconductivity, because the magnetism arising from the static ordering of magnetic moments competes with superconductivity, which is needed for the formation of Cooper pairs (dynamic pairing of two conducting electrons with opposite spin). Because Iron and Nickel are representative magnetic elements, these discoveries were accepted with surprise by the condensed matter physics community.

IBS can be categorized into several types, such as '1111' type (e.g., $LaFeAsO_{1-x}F_x$ and $SmFeAsO_{1-x}F_x$), '122' type (e.g., $Ba_{1-x}K_xFe_2As_2$ and $Sr_{1-x}K_xFe_2As_2$), '111' type (e.g., $LiFeAs$) and '11' type (e.g., $FeSe$, $FeSe_{1-x}Te_x$), according to different chemical compositions and crystal structures; they all have layered crystal structure and small coherence lengths (the characteristic exponent of the variations of the density of superconducting component, one parameter in the BCS theory $\xi_{BCS} = \frac{\hbar v_f}{\pi\Delta}$, where v_f is the Fermi velocity, and Δ the superconducting energy gap), showing high upper critical fields (B_{C2}). Two compounds classes gained some interest recently: the 1144 structures, which show high J_c values in high magnetic field, and $(Li, Fe)OHFeSe$, an intercalated structure which can be grown as thin films with excellent structural and superconducting properties [13]. Though the T_cs of iron-based superconductors (up to 38 K for '122' system and 56 K for '1111' system) are not as high as those of cuprate superconductors, their anisotropy ($\gamma = B_{C2}^{\|ab}/B_{C2}^{\|c}$), is remarkably lower [10].

These materials contain a common building block of a square lattice of Fe^{2+} ions with tetrahedral coordination with the Pn (P and/or As) or Ch ions. A lot of parent compounds are known, and each crystal structure can be derived from the insertion of ions and/or building blocks between the Fe$Pn(Ch)$ layers. Figure 2.6 shows the structure of some parent materials of IBS. [14]

Because the Fermi level of each parent compound is primarily governed by five Fe 3d orbitals, iron plays a primary role in the superconductivity; this is in sharp contrast to that in cuprate superconductors, in which only one 3d orbital is associated with the Fermi level. These five 3d orbitals dominating

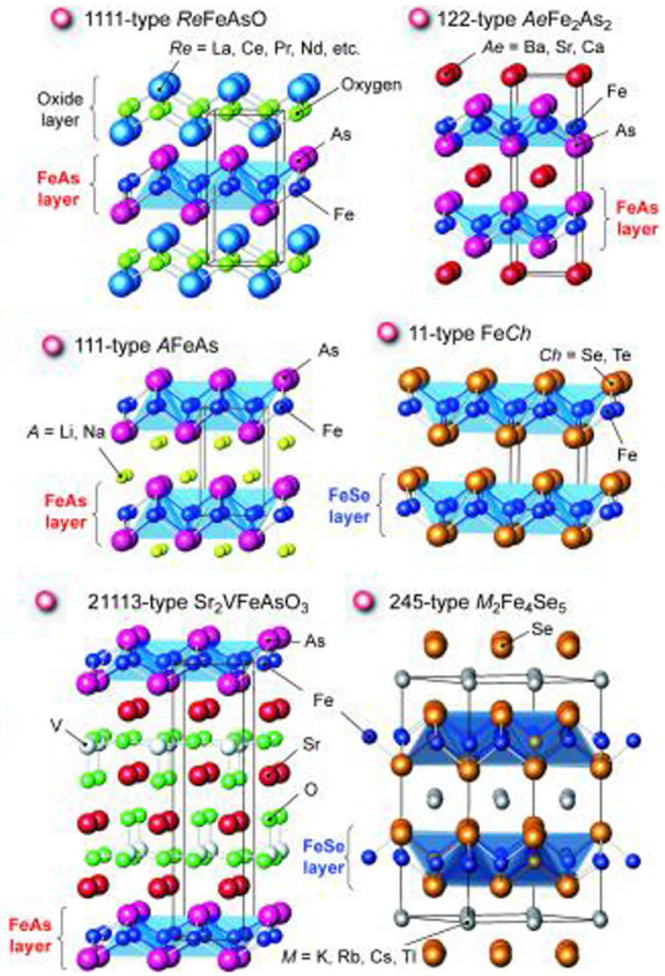

Fig. 2.6: Various parent materials of IBSCs [14].

the Fermi level render these compounds multiband superconductors [13].

All the IBS have similar phase diagram, as the one presented in figure 2.7(a). Superconductivity can be induced in all IBS materials by chemical doping or pressure, or a combination of both, as long as the result is the suppression of magnetism. In contrast to copper oxides, none of these system is truly two dimensional. This is beneficial in terms of practical applications, because in polycristalline two dimensional materials, superconductivity can be destroyed by a relatively small current.

In cases in which the Fermi surface has been mapped by angle-resolved photoemission spectroscopy (ARPES), two sets of Fermi surfaces roughly separated by the same wavevector, have been revealed. It is tempting to

assume that the features that IBS have in common reflect a common origin from the observed superconductivity. It can be concluded that proximity to a magnetic quantum critical point signals that magnetic spin fluctuations play an important role. Note that two electrons in a singlet Cooper pair have the same charge, but opposite spins. A corollary of this is that magnetic excitations lead to pairing only if the corresponding wavevector spans parts of the Fermi surface with order parameter (that is, the pair wavefunction) of opposite sign. Noting that there are two sets of Fermi surfaces that are roughly separated by the same wavevector, the so called s_{+-} superconductivity is derived, in which the sign of the order parameter is switched between the two sets of Fermi surfaces [15].

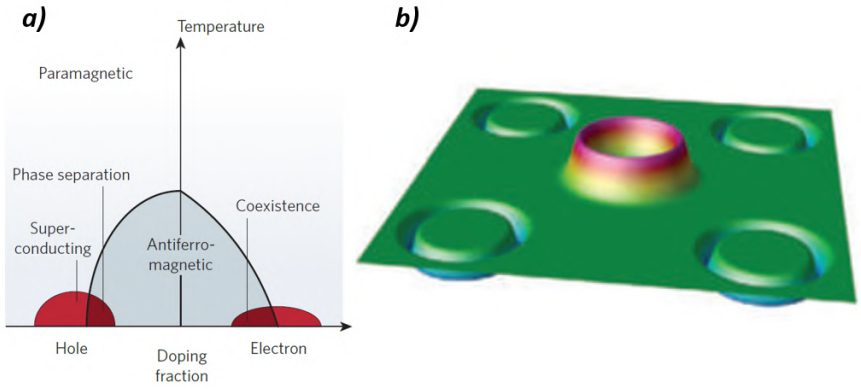

Fig. 2.7: (a) Schematic phase diagram for the 122 family of iron-based superconductors. (b) A schematic representation of the superconducting order parameter in $s_{\pm}$ *wave*. The Fermi surface is approximated by a small circle in the centre (the first band) surrounded by four larger circles (to comply with the tetragonal symmetry; the second band). In all cases, the height of the 'rubber sheet' is proportional to the magnitude of the order parameter (including its sign) [15].

Tanks to the different order parameter symmetry of IBS with respect to HTS, some of the unconventional pairing drawbacks affecting HTS are less unfavorable in IBS. As a first example, the effect of impurities is detrimental to Tc in HTS, whereas in IBS the same amount of artificial defects do not affect, or can eventually improve, the superconducting properties. A second example is the supercurrent blocking due to a misalignment between grains. The high upper critical fields (B_{C2}) and low anisotropy ($\gamma = B_{C2}^{\|ab}/B_{C2}^{\|c}$) make iron-based superconductors quite attractive for high-field applications; in fact, they can work between 5 and 20 K, they show, in the form of thin films, high critical current density (meaning $J_c > 1MA/cm^2$ at $10T$ and

	1111	**122**	**11**	YBCO	Nb_3Sn
T_c (K)	55	38	21	93	18
$B_{C2}(0)$ (T)	60	60	55	60	30
ξ_{ab} (nm)	2.5	3	1.5	2.2	10
γ	5	2	2	5-7	1
λ_{ab} (nm)	200	200	490	180	50-100
Ginzburg number G_i	4×10^{-4}	2×10^{-5}	1×10^{-3}	10^{-3}	10^{-5}
Critical GB angle	$\sim 9°$	$9°$	$9°$	$3°$	

Table 2.1: Properties of the iron based that are most appealing for applications, compared to $YBCO$ and Nb_3Sn

$4K$), and an average J_c of $1.3 \times 10^4 A/cm^2$ for a 100-m-class-length wire. [14]

Table 2.1 summarises the properties of the iron-based materials that are most attractive for applications, together with those of YBCO, as a representative of HTS, and Nb_3Sn, as a representative of low temperature superconductors (LTS). The anisotropy factor γ is quite low in IBS, with 11 and 122 compounds being almost isotropic. The coherence length ξ, which is related to the amplitude of B_{C2}, is quite small in all IBS, similar to that of YBCO. The longer the coherence length, the greater the ability of supercurrents to cross grain boundaries; on the other hand, a small coherence length implements pinning mechanisms and thus favours current transport. The Ginzburg number G_i combines all the above superconducting parameters to parameterise the amplitude of the thermal fluctuations. It is lower in IBS than in YBCO, which is a notable advantage in terms of applications. Another advantage for applications is the critical angle between the grain boundaries. To evaluate this, in the case of Fe(Se,Te), thin films have been deposited on a bicrystalline substrate with a single well-defined grain boundary. The inter-grain J_c across a grain boundary tilted of 45° is around one order of magnitude lower than the intra-grain J_c [16]. Therefore, we can say that, even if the decay of the critical current density is not as impactful as for cuprates, still at high angle the suppression is significant. Figure 2.8 compares the misorientation dependence of inter-grain J_c for different IBS, and for YBCO and Bi2212.

Comparing figures 2.8(a) and (b), it appears that, for iron based superconductors, the critical misorientation angle θ_{GB} is $\sim 9°$, while the critical misorientation angle for REBCO cuprates is around 3°.

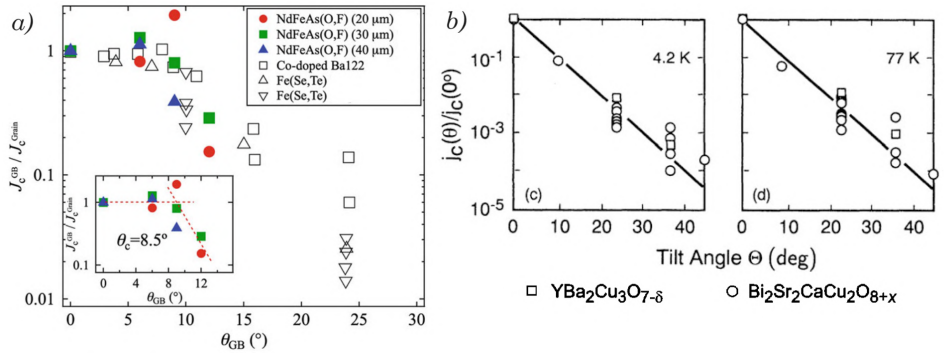

Fig. 2.8: Angle dependence of the reduced intra-grain critical current density (J_c^{GB}/J_c^{Grain}) for $NdFeAs(O,F)$ bicrystal junctions (full symbols), $Ba(Fe,Co)_2As_2$ (squares) and $Fe(Se,Te)$ (triangles) [18]. (b) Angle dependence of the reduced critical current density across [001]-tilt grain boundaries in YBCO (squares) and Bi2212 (circles) at 4.2 and 77 K. [19].

2.2.1 Thin Films

Thin films are good platforms for both fundamental and applied superconductivity research. Iron based superconductors have been deposited as thin films using a variety of methods and substrates; high J_c have been reached as shown in figure 2.9.

The main criteria for the selection of substrate and buffer layer materials are:

1. Small lattice mismatch between films and substrates;
2. No chemical reaction between films and substrates.

Depending on the desired application, other properties of the substrates might become important as well, such as flexibility, mechanical strength, magnetic and dielectric behaviour as well as costs and availability. The in-plane lattice parameters of iron-based superconductors are in the range between 3.77 and 4.02 Å. For 001-oriented epitaxial films, the most commonly used are: (pseudo-) cubic or perovskite $YAlO_3(110)$ (YAO), $LaAlO_3(001)$ (LAO), $(LaAlO_3)_{0.3}(Sr_2TaAlO_6)_{0.7}(001)$ (LSAT), $SrTiO_3(001)$ (STO) and $MgAl_2O_4(001)$ (MAO) as well as Fe and CeO_2 layers, which are relatively close to the in-plane lattice parameters of IBS. However, $MgO(001)$ and r-cut sapphire, $Al_2O_3(1102)$, with a large lattice misfit have also been used and IBS films (11, 122 and 1111) on MgO are grown epitaxially. $Fe(Se,Te)$

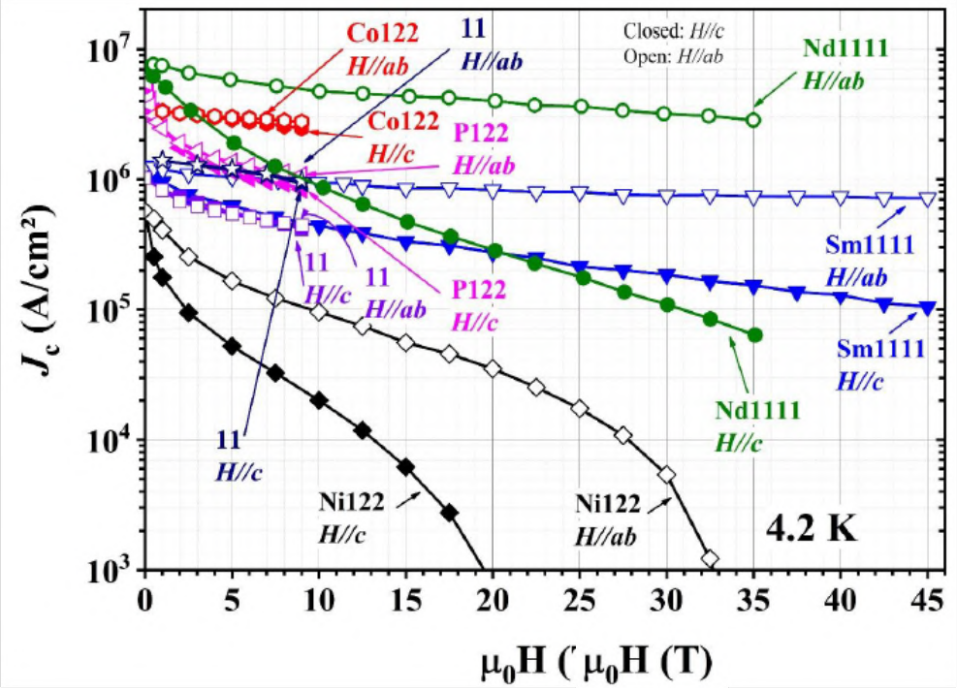

Fig. 2.9: Comparison of J_c(H) for different iron based deposited on single crystals [20].

and $Ba(Fe_{1-x}Co_x)_2As_2$ epitaxial thin films have been realized on STO. Finally, it has been reported that fluoride substrates such as CaF_2(001) (CaF) and SrF_2(001) are very suitable templates for epitaxial growth of various IBS with good crystalline quality as well as superconducting properties. It is general consensus that CaF_2 seems to be the best template for iron-based superconductors; however, one has to keep in mind that CaF_2 is extremely brittle, which makes it hard to handle.

There are two main deposition techniques that have been employed for the deposition of Iron Based Superconductors, usually in UHV:

- PLD: Pulsed Laser deposition is a very versatile deposition method, in which a target, excited by a high-intensity laser, releases a plasma plume towards the substrate.
- MBE: Molecular Beam Epitaxy is a suitable method for producing thin films containing volatile elements. Sublimed elements condense on the substrate, where they can react with each other.

PLD is mainly used for 11 and 122 compounds, while MBE for 1111 com-

pounds, 122 compounds with volatile elements and ultra-thin FeSe films. Many other methods, such as sputtering and chemical deposition (chemical vapour deposition CVD, chemical transport deposition CTD, electrochemical deposition ECD) have been employed for FeSe and Fe(Se,Te). Most of these techniques need further optimization [13].

2.3 Fe(Se,Te)

Among all the iron based superconductors, FeSe (so-called 11 family) is very interesting for the absence of arsenic, and for its simple structure. FeSe has a critical field up to 50 T and a critical temperature of 9K, but an enhancement of the T_c was observed with the substitution of Te for Se, for which the T_c increased up to 75%.

T. Taen et al [21] have been able to grow FeSeTe high quality single crystal, reporting a critical temperature $T_c \sim 14K$, and a critical current density J_c above $1 \times 10^5 A/cm^2$ at 5K zero field.

2.3.1 Artificial Pinning

$Fe(Se_{0.5}Te_{0.5})$ is a promising material for high field application but, still, its properties might be enhanced. It has been shown that the maximum achievable J_c value is 30% of the depairing current density J_d [22]. The depairing current density is that at which the kinetic energy of the superconducting carriers equals the binding energy of the Cooper pair, and hence is the current threshold above which the superconductivity of the superconductor is totally destroyed. In [23] K. Iida et al. point out that we are able to reach only up to $\sim$ 10% of the depairing current density J_d in thin films deposited on single crystals suggesting room for further improvement. The critical current density can be enhanced adding pinning centers to the phase: increasing the possibility to pin the vortex, and hence the pinning force, allows more current to flow in the material. Since the coherence length of IBS is in the order of few nm (and for Fe(Se,Te) specifically is $\sim$ 1.5 nm), nano-sized defects can strongly pin the vortex.

There are two strategies to insert artificial pinning centers in superconducting material: doping (with compounds or nanoparticles/nanowires) or irra-

diating with high energy particles (protons or heavy ions).

$YBa_2Cu_3O_7$ thin films have been successfully doped with $BaZrO_3$, so the same strategy has been employed to enhance pinning in Ba-122 thin films [24], using the doping as powders, nanoparticles or nanopillars. For what concern irradiation, different particles lead to different type of defect, and therefore result in different effect on supeconducting properties. Not only the particle type and energy play a role, also the interaction with the substrate is important.

2.3.2 Wires and tapes

The above-mentioned properties of Fe(Se,Te) make it extremely interesting for high field applications. For this to be possible, it is necessary to obtain a conductor, typically a wire or a tape. The Powder in Tube (PIT) technique is widely used to make superconducting wires (e.g. for Nb_3Sn or MgB_2), as it is easily scalable to industrial production and quite inexpensive. It is therefore natural that a first attempt to make Fe(Se,Te) wires was indeed made by PIT: a metallic tube was filled with Fe(Se,Te) powders and cold worked through drawing and groove-rolling process to obtain round (or square) wires (typical diameter of 1 mm) [25]. Several metallic sheaths were tested, with the aim to establish which metal or alloy could be more suitable in terms of mechanical and chemical properties for this kind of superconductor. Tubes of Cu, Ag, Nb, Ta, Ni, Fe, cupro-nickel 90-10 and brass have been tested. Although all the cited metal sheaths are largely used in superconducting wire production, almost all of them react with the phase inside the wire, damaging it. Iron is the only metal compatible with the phase, however, regardless the amount of iron in the starting powders, an iron excess in the superconducting core was found, which dramatically affects the superconducting properties.

It seems that the manufacture of Fe(Se,Te) wires is not trivial, since no sheath has yet been found that gives good performance. An alternative way to obtain conductors with this phase is to make iron-chalcogenide coated conductors: thin Fe(Se,Te) films deposited on technical substrates, consisting of a metallic tape covered by one or more buffer layers.

An essential feature to check in order to be able to manufacture coated conductors is the J_c transparency across the grain boundary.

As shown in section 2.2, for Fe(Se,Te) the critical misorientation angle θ_{GB} is $\sim 9°$, while the critical misorientation angle for REBCO cuprates is around 3°. To be suitable for application, REBCO supeconductors must be grown via chemical or physical routes on coated conductor structure: a metallic template (that can be oriented, as for RABiTS templates, or not, as for IBAD templates) covered with many buffer layers, with the dual purpose of increasing the epitaxiality and working as a chemical barrier. The advantage of FeSeTe is that this material could be grown on much simpler coated conductors: we do not need to protect metallic tape from oxidation as the growth of the phase occurs in UHV,and as explained the misorientation is not that strict. Our aim is a single buffer layered metallic template. Thanks to that, the cost can be reduced together with the complexity, making a FeSeTe coated conductor a worthy competitor for REBCO coated conductors.

Towards a coated conductor

Several groups reported the growth on technical substrates, both IBAD-MgO and RABiTS templates, shown in figure 2.10.

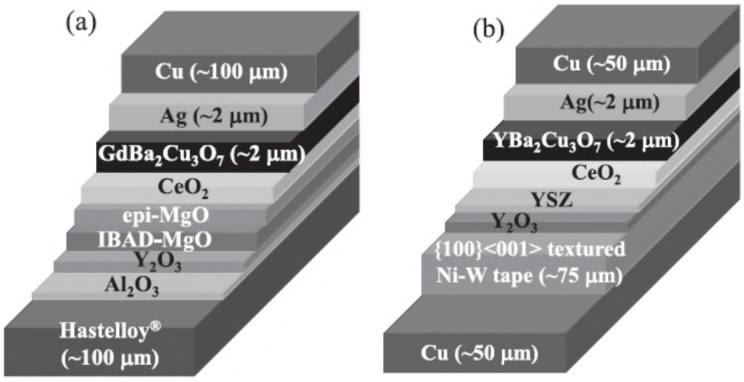

Fig. 2.10: Schematic representation of typical coated conductor: IBAD-MgO (a) and RABiTS (b).

Despite the large lattice mismatch between Fe(Se,Te) and MgO ($a_{FST} = 3.81$Å, $a_{MgO} = 4.21$Å), thin films were successfully fabricated on IBAD-MgO templates. Weak-link behaviour is absent in these samples; the lower T_c (11K) of that film compared to the films on single crystals is mostly ascribed to the large lattice misfit. The sample on IBAD-MgO showed an almost isotropic J_C over 10^4 A/cm^2 at $25T$ and $4.2K$. To further improve

$J_C - H$ properties of Fe(Se,Te) on technical substrate, thin films have been fabricated on CeO_2-buffered RABiTS. The lattice parameter of CeO_2 almost perfectly matches the in-plane lattice parameter of the phase. Given to that, the film showed a higher onset T_C of over $20K$, with a sharp transition of $1K$ width. The sample showed a nearly isotropic $J_C \sim 0.1MA/cm^2$ at $4.2K$ and $30T$. [23] Figure 2.11 compares the J_c behaviour in field for different iron based superconductors deposited on technical substrate. We can conclude that CeO_2 buffer layer is a good buffer for achieving high T_c.

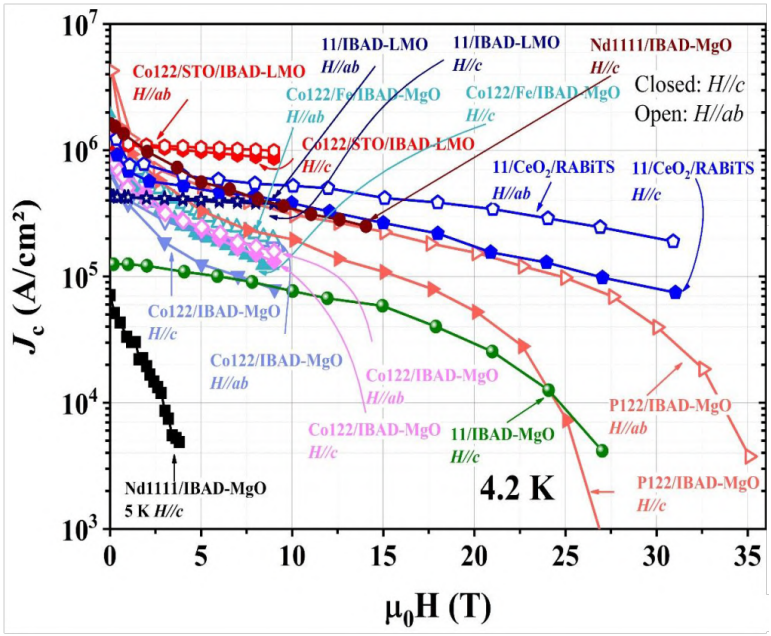

Fig. 2.11: Comparison of $J_c(H)$ for different iron based deposited on technical substrates [20]

Anyway, iron selenium tellurium can be a competitor for REBCO coated conductors only if a significant cost reduction is available. This can be achieved with a considerable simplification of the buffer layer structure: our aim is to reduce the buffer layer to a single Zr:CeO_2, to improve orientation of the substrate and to act as chemical barrier.

G. Sylva et al. [26], [27] demonstrated that a single CeO_2 buffer layer grown via PLD on an oriented metallic template can successfully be employed as substrate for the growth of $FeSe_{0.5}Te_{0.5}$ superconducting thin films. It acts as chemical barrier, other than improving the orientation of the film, avoiding the poisoning of the superconductor. In order to reduce cost production

on such templates, we focused on the employment of chemically grown buffer layer.

2.4 Background - Fe(Se,Te) thin film at CNR Spin Institute

At CNR Spin Institute, epitaxial thin films are grown in ultra high vacuum atmosphere via pulsed laser deposition.

Figure 2.12 illustrates the $\theta - 2\theta$ XRD pattern of a typical film grown on a STO single crystal substrate: this pattern shows only $(00l)$ reflections of the film, indicating the the excellent purity of the phase, in addition to the optimum *c-axis* alignment growth. Typical ω scan on these samples of $(00l)$ peaks show rocking curve with full width at half maximum (FWHM) around $1°$, and the *c-axis* values extracted from the $(00l)$ peak positions are around $5.84 - 5.89$ Å.

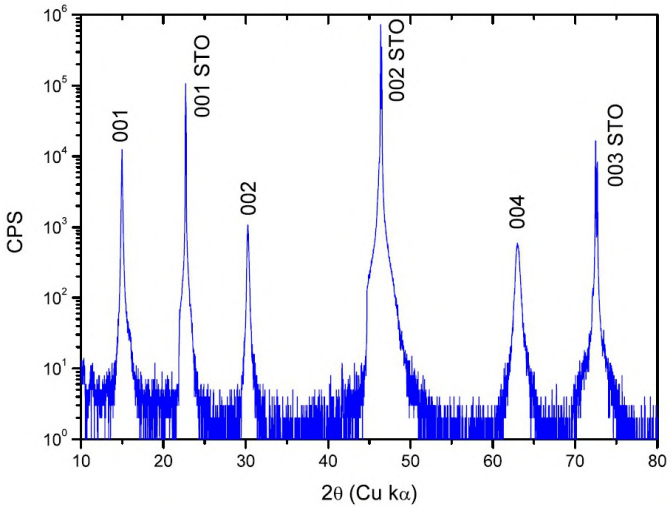

Fig. 2.12: XRD $\theta-2\theta$ scan of Fe(Se,Te) film deposited on $SrTiO_3$. Only the $00l$ reflections of the film and substrate are detectable [30].

Average critical temperature T_c is $\sim 18K$, with a record of $T_c = 21K$ reported from E. Bellingeri et al. in [31] on a 200 nm thick film grown on $LaAlO_3$.

$FeSe_{0.5}Te_{0.5}$ thin films can be grown on many different oriented substrates, but the type and quality of the substrate play an important role: it's been

found that the superconducting properties are related to the in-plane lattice constant of the substrate on which they are grown. There is a non-trivial dependence on lattice mismatched substrates, and strain affects both the enhancement of the critical temperature and the pinning mechanism. In [32], the authors compared the properties of thin films grown on different substrates, all with a slightly different lattice paramenter. The substrates used were: magnesium oxide (MgO,a=4.217 Å), strontium titanate ($SrTiO_3$, a=3.905 Å),lanthanum aluminate ($LaAlO_3$, a=3.789 Å), yttria stabilized zirconia (YSZ, a=3.637 Å), calcium fluoride (CaF_2, a=5.462 Å) and lithium fluoride (LiF_2, a=4.020 Å).

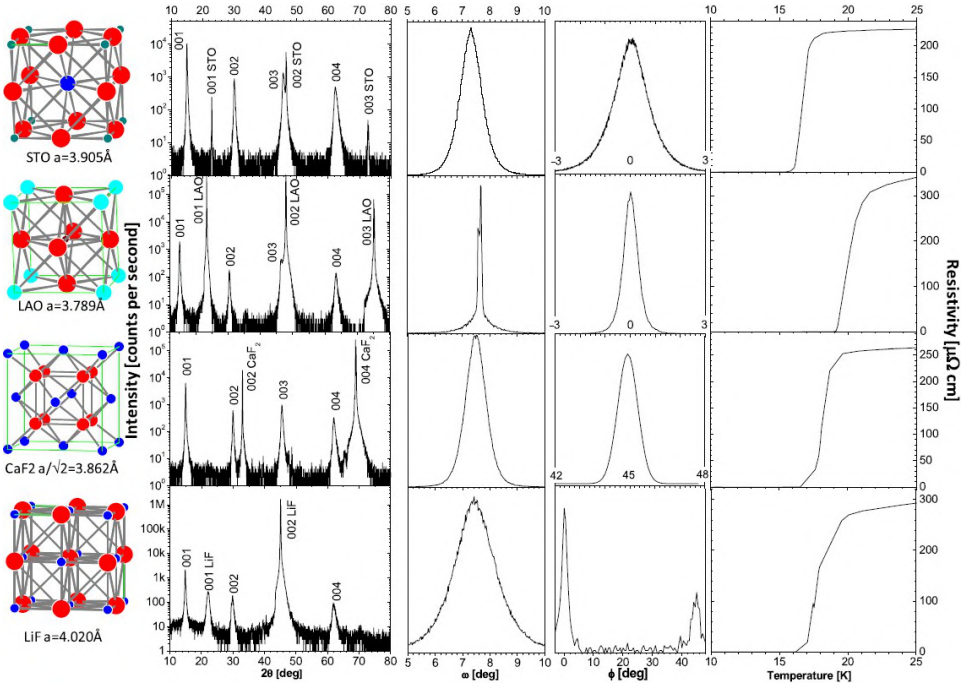

Fig. 2.13: Properties of thin films grown on different substrates: $SrTiO_3$, $LaAlO_3$, CaF_2, LiF_2. The first column shows the substrate structure, the second the $\theta - 2\theta$ scans, the third the rocking curve of the 001 reflections, the fourth the ω scans, and in the last we report the detail of the superconducting resistive transition for the optimal samples on that particular substrate [32].

Figure 2.13 summarizes some of the results obtained in [32]. For all the substrates available, the high quality of the films in confirmed by XRD patterns (second column), in which all the peaks shows the (00l) reflections of $FeSe_{0.5}Te_{0.5}$ films and substrates. The last column of figure 2.13 shows the critical temperature of these films: T_c depends on the substrate.

What the authors noticed is that the accumulated strain is affected by the substrate, and it affects the superconducting properties. From these observations, CaF_2 appears to be a very suitable substrate for the growth of $FeSe_{0.5}Te_{0.5}$ thin films, allowing high crystalline quality, excellent epitaxy and a clean interface, other than allowing the introduction of strain with a related enhancement of the critical current density, to values similar at those reported on $LaAlO_3$ [31]. For this reason, CaF_2 is the mainly single crystal substrate for FeSeTe thin films.

Anisotropy

An important shortcoming of cuprates is the large anisotropy γ: the superconducting properties of the phases are strongly related to the direction of the applied magnetic field (whether it is parallel or perpendicular to the ab plane). The anisotropy becomes very important when considering a material suitable for high field applications. Generally, iron selenide is, thanks to its simpler structure, much less anisotropic than cuprates. However, for FeSeTe thin films, the choice of the substrate is affecting the value of γ. In [33] $FeSe_{0.5}Te_{0.5}$ thin films are grown via PLD on three different substrates: $SrTiO_3$ (001), $LaAlO_3$ (001) and CaF_2 (001).

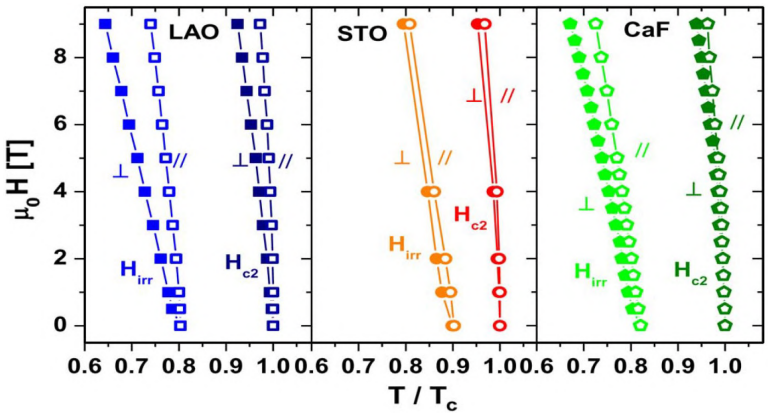

Fig. 2.14: Hc_2 and H_irr versus T/T_c for magnetic field up to 9 T for thin films deposited on LAO, STO, and CaF substrates [33].

In figure 2.14 the upper critical field H_{C2} and the irreversibility lines H_{irr} as a function of the reduced temperature T/T_c, both on parallel and perpendicular configurations, up to 9 T, for films deposited on LAO, STO and CaF_2 are shown. From this comparison, it appears that while films grown

on LAO present quite significant anisotropy, films on CaF_2 show a little one and films on STO are practically showing none. Adding the higher critical temperature observed for films grown on CaF_2 compared to those on STO, CaF_2 results promising for $FeSe_{0.5}Te_{0.5}$ films.

The good quality of CaF_2 as a substrate for Fe(Se,Te) is confirmed by V. Braccini et al. in [34], where FeSeTe thin films on CaF present a critical temperature of 20 K, and a critical current density of $1.1MA/cm^2$ at 4K in self field, with a very weak magnetic field dependence and high isotropy.

2.4.1 Natural Pinning

A combination of high resolution imaging (STEM) and transport measurement, made in function of the magnetic field orientation, together with a pinning model can correlate the microstructure to the type of pinning. [35] $Fe(Se_{0.5}Te_{0.5})$ thin film deposited on a CaF_2 single crystal has been deeply studied.

Nanostructural analysis

Transmission Electron Microscopy (TEM) was performed on the $Fe(Se_{0.5}Te_{0.5})$ thin film along the [110] direction (in plane view) and the [001] direction (out of plane view). This characterization points out that the film is highly epitaxial, moreover the predominant in-plane orientation was found to be the $[110]Fe(Se,Te) \parallel [100]CaF_2$.

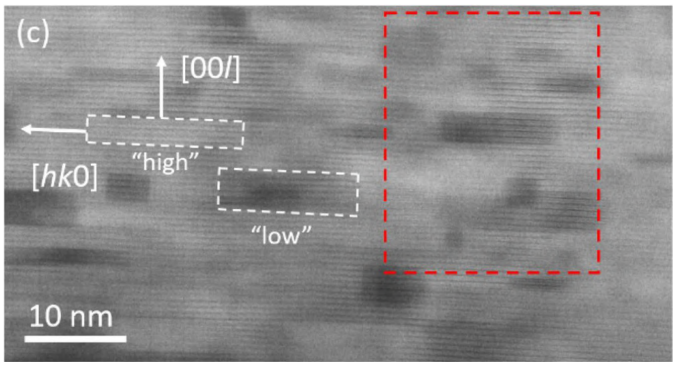

Fig. 2.15: Electron microscopy view of the Fe(Se,Te) film, indicating high- and low-atomic mass grains [35].

The experimental conditions of figure 2.15 were properly chosen to minimize the contribution from diffraction contrast, therefore the domains with different contrast can be ascribed to a different average atomic mass, suggesting the presence of domains with different stoichiometry: dark and bright regions mark out the shape of some grains with low- and high-atomic mass respectively. The typical grain is a rectangular shape $15 - 20$ nm wide and $3 - 5$ nm high.

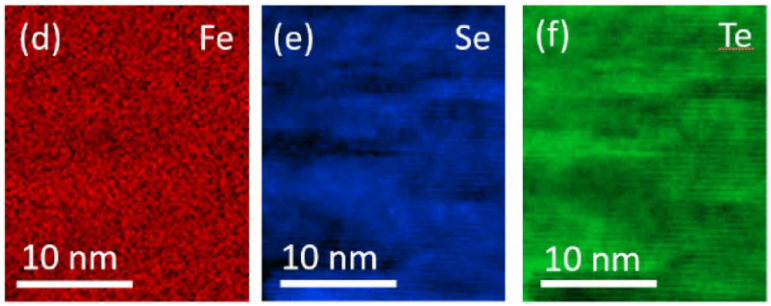

Fig. 2.16: Corresponding EELS elemental maps of the portion indicated by a red dashed line in figure 2.15 [35].

The elemental maps in 2.16 confirm the different stoichiometry in the grains: in particular, Te-rich grains correspond to bright regions in the Z-contrast image. Se and Te contents are complementary since they occupy the same lattice site, while the Fe content is quite uniform.

Cross-view STEM measurements with atomic resolution were made in order to investigate the atomic structure of the various grains.

From figure 2.17 it is clear that the grains are generally [110] oriented, parallel to $[100]CaF_2$ substrate. The intensity modulation among grains highlights the different stoichiometry of grains. The presence of Te-rich and Se-rich domains generates a lattice mismatch between grains; that implies also that grains are not properly aligned with the main [110] direction. From electron diffraction measurements emerged that grains with other in-plane orientation are present together with the dominant [110]-aligned ones. the interface between a rotated grain and an aligned one determines two dimensional defect at the grain boundaries (GB); this defect can be divided in two types: "$(GB) \parallel ab$" if they are at the top-bottom of a rotated grain, or "$(GB) \perp ab$" if they are at the side.

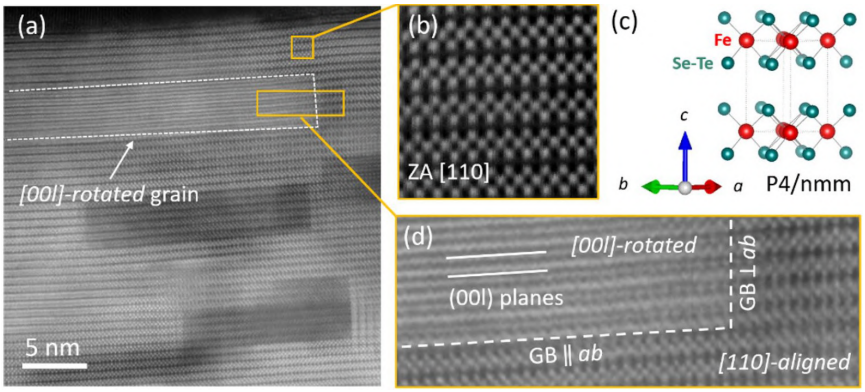

Fig. 2.17: Structure of the Fe(Se,Te) film at high-resolution. (a) High-resolution Z-contrast STEM image of the [110]-oriented $FeSe_{1-x}Te_x$ film. (b) Enlarged view of the atomic lattice and corresponding 3D atomic model of the $P_{4/nmm}$ unit cell in (c). (d) Detail of grain boundaries between a rotated grain and a not-rotated one [35].

Pinning Properties

Figure 3.11 shows the behaviour of the critical current density J_c for three different temperature (4.2, 8 and 12 K in particular), in applied magnetic field, parallel to ab plane in 3.11 (a), and perpendicular to that in 3.11 (b). Comparing the panels, is evidenced the low anisotropy of the Fe(Se,Te).

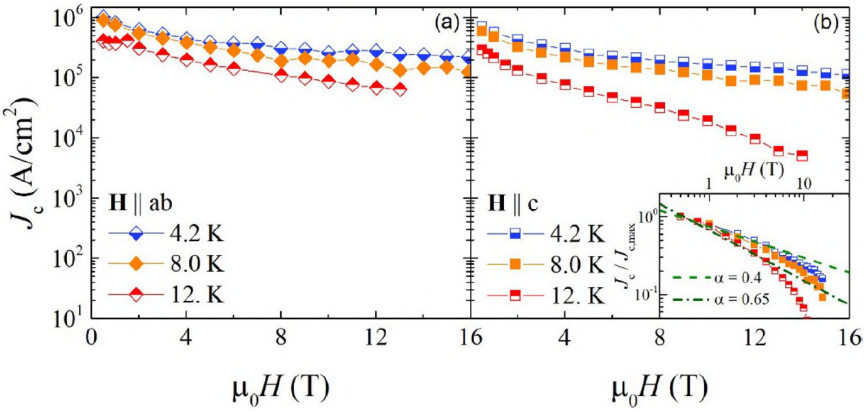

Fig. 2.18: Critical current J_c as a function of magnetic field at different temperatures of 4.2, 8 and 12 K with field parallel (a) and perpendicular (b) to the ab planes [35].

In order to understand the type of pinning that comes into play, the pinning force $f_p = J_c \times B$ was extracted from the J_c measurements. Applying the *Dew-Huges model* [36], it is possible to link the shape of the normalized pinning force plotted in respect to the reduced field, and the position of the peak, to the nature and dimensions of the pinning centers.

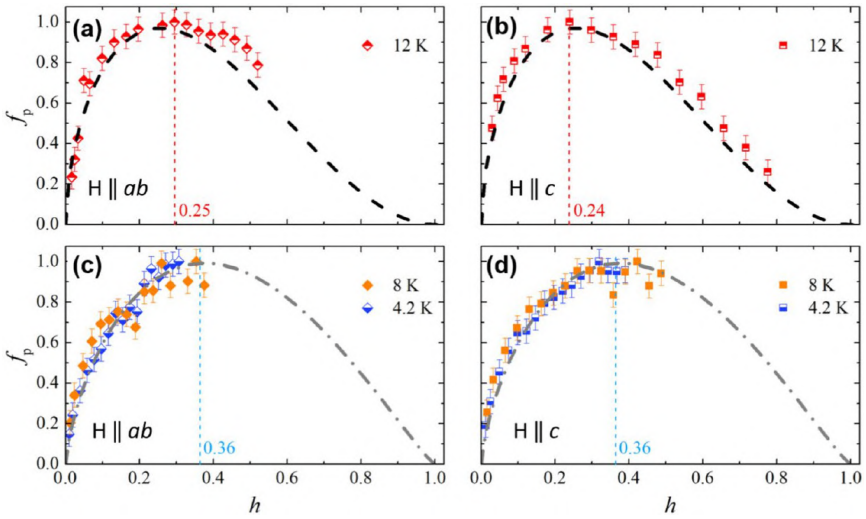

Fig. 2.19: Normalized pinning force as a function of the reduced field $h = H/H_{irr}$ at different temperatures of 4.2, 8 and 12 K, with field parallel (a,c) and perpendicular (b,d) to the ab planes. Dashed and dot-dashed lines come from Dew-Hughes fitting procedure [35].

In the plot in figure 2.19 the normalizing field H_{irr} was estimate as the value at which the $J_C^{1/2}(\mu_0 H)$ curve is linearly extrapolated to zero.

The different shape, together with the different position of the peak, of the pinning force at low and high temperature, suggest that different pinning mechanism are active in different temperature regimes. These mechanism can be identified using the *Dew-Huges model*.

A change of pinning mechanism is identified above and below $T_c/2$: at higher temperature the Dew-Huges model suggest the presence of both 2D δl and 1D δl pinning centers, while at lower temperature the model predicts a single pinning contribution of a ΔT_c-type pinning. In simple terms, while at lower temperature the pinning is strongly related to the different domains with different stoichiometry (leading to different critical temperatures), at higher T the pinning due to the 2D and 1D defects in the lattice structure is predominant.

Figure 2.20 shows the full angular dependence of the critical current density $J_c(\theta)$ measured at a fixed temperature of 8K, for fields of 2 an 16 T. The anisotropy factor is confimed to be very low, between 2 and 3, both at low and high applied field. Moreover, a huge peak is observed for the orientation of the applied field in the ab plane of the superconducting film, which is the

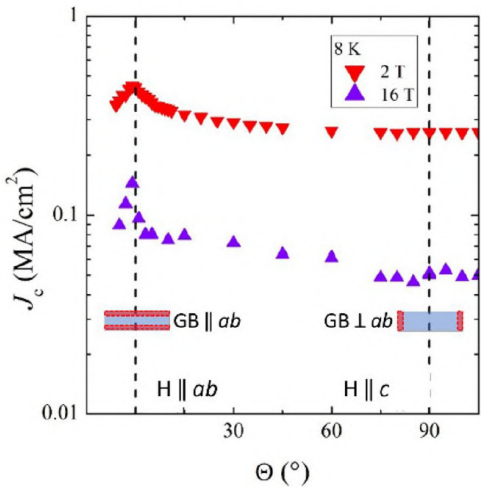

Fig. 2.20: Angular dependence of the critical current density $J_c(\theta)$ in semi-log scale measured at 8 K and in fields of 2 and 16 T [35].

signature of the pinning mechanism related to the layered microstructure of this material and to the 2D GB $\parallel$ *ab* defects.

Chapter 3

Films and Coated Conductors

One aim of my work is deposition of Fe(Se,Te) from thin films on single crystals to coated conductors. A coated conductor is a high-tech superconducting tape consisting of a metallic substrate covered with several buffer layers, typically oxides, that help improving the texture of the substrate but also play as chemical barrier, to avoid poisoning of the superconductor. The metallic substrate can be textured, as NiW in RABiTS ("rolling assisted biaxially textured substrates"), or not, as hastelloy in IBAD-MgO ("ion beam assisted deposited MgO"). This type of substrates have been widely developed in the last decades for the fabrication of REBCO Coated Conductors [38]; it is essential due to its low critical misorientation angle between grain boundaries θ_{GB}. As mentioned in section 2.3.2, one advantage of Fe(Se,Te), in respect to ReBCO, is the larger tolerance on the critical misorientation angle between grain boundaries ($\theta_{GB} \sim 9^\circ$ for Fe(Se,Te) against $\theta_{GB} \sim 3^\circ$ for YBCO). Thanks to that, Fe(Se,Te) could be deposited on much simpler coated conductor: one buffer layer can be enough to assure a good orientation of the film, other than acting as chemical barrier.

My work was carried out as part of the PRIN Hibiscus project and the JRA agreement with ENI. My main role has been the optimization of the growth of FeSeTe thin films using the pulsed laser deposition (PLD) technique on different substrates and templates, followed by their structural and transport properties characterization. First, I optimized the growth of thin films on single-crystalline substrates such as CaF and STO. Then, with the final aim to fabricate a simplified coated conductor, I studied the

deposition of FST thin films on single crystals with a chemically deposited Buffer Layer (namely, YSZ + MOD Zr-doped CeO2 deposited in ENEA). Finally, I studied the possibility of depositing films on a metallic template made by biaxially textured NiW with Zr-doped CeO_2 buffer layer. I then worked on the structural characterisation, using X-ray diffractometry, and the superconducting properties, using transport (resistivity as a function of temperature, critical current) and magnetic measurements. Structural analyses of the buffer, deposited both on single crystals and on metal substrates, together with EBSD analyses of the buffer and Fe(Se,Te) films, were carried out at ENEA. Finally, TEM analyses were carried out at the IMM Institute of the CNR. The best samples were characterised at both SPIN and ENEA and irradiated in several facilities as will be described in the next chapters.

$Fe(Se, Te)$ epitaxial thin films are grown via pulsed laser deposition (PLD). Inside a ultra high vacuum chamber, a target with the proper stoichiometry $FeSe_{0.5}Te_{0.5}$ is excited using a pulsed laser; atoms of the target are therefore released as a plume, as shown in figure 3.1. Those atoms reach the substrate, placed under the target and heated up to give atoms enough energy to rearrange, forming an organized lattice.

Fig. 3.1: PLD chamber and plume

Many parameters can be tuned in order to optimize the growth of samples in the PLD:

- Frequency of the laser;
- Distance target-substrate;

- Temperature of the substrate;
- Density and homogeneity of the target;
- Laser energy and frequency;
- Laser focus and spot dimensions.

To grow our samples, I used a Nd:YAG laser with a wavelength $\lambda = 1064$ nm, focused on a 2 mm^2 spot on the target with a fluency of 2 Jcm^{-2}, and frequency of 3 Hz. The substrate is maintained at $300°C$, at 5 cm from the target. The base pressure is $\sim 5 \times 10^{-9}$ $mbar$, which increase of about one order of magnitude during the deposition.

3.1 Target preparation

The quality of the targets strongly influences the properties of thin films, therefore, using high quality targets is essential. Most of the targets used during this thesis have been prepared at Department of Chemistry, University of Genova. The preparation starts with the synthesis of $Fe(Se_{0.5}, Te_{0.5})$ powders by solid state reaction method. High purity powders of Fe (3N+), Se (5N) and Te (5N) are mixed together following the stoichiometry of the phase, in controlled atmosphere. Then, the mixed powders are sealed in a pyrex glass tube and slowly heated up to $500°C$ and kept for 100 hours. After such a long time, we can be sure that the reaction has taken place. The result is homogeneous black powders, as shown in figure 3.2. [39]

Fig. 3.2: $FeSe_{0.5}Te_{0.5}$ reacted powders, in a pyrex glass tube.

XRD analysis performed on powders (figure 3.3) show the presence of a main PbO-type crystal structure, with small trace of compositional neighbouring compounds.

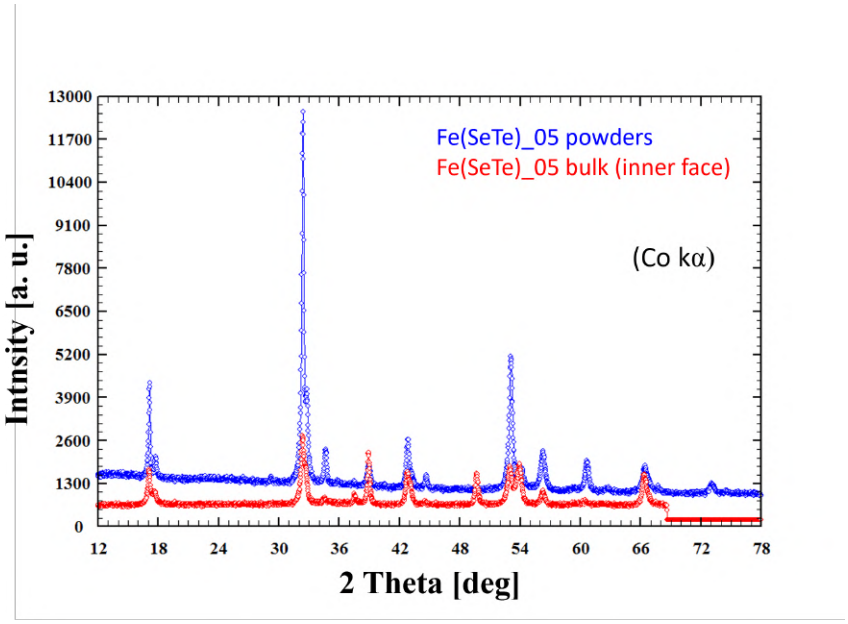

Fig. 3.3: XRD pattern of $FeSe_{0.5}Te_{0.5}$ powders (blue) and a $FeSe_{0.5}Te_{0.5}$ target (red).

These powders are then processed, in order to obtain a dense pellet. More in detail, they are pressed in an alumina crucible, enclosed in an alumina tube, which, after a series of washing with argon gas, is pumped under vacuum. This tube is than inserted in a tubular furnace, and kept at $1000°C$ for 30 minutes. Finally, the pellet is quenched by extracting it from the furnace. The resulting target is shown in figure 3.4.

Fig. 3.4: $FeSe_{0.5}Te_{0.5}$ target as prepared and after many depositions

Compared to the "standard" sintering technique, this process has proven to improve homogeneity and density of the samples, parameters that, as mentioned above, strongly affect the quality of the films obtained through pulsed laser deposition. Figure 3.3 shows XRD patterns of both powders (blue curve) and a target (red curve) prepared as above described. In both

patterns, principal peaks of the phase are visible, meaning that the phase is well grown.

Scanning electron microscope (SEM) analysis exhibit the global stoichiometry as $FeSe_{0.4}Te_{0.6}$); moreover, the sample does not appear perfectly homogeneous on a local scale, as evident in figure 3.5. The darker regions are in perfect stoichiometry, $Fe_1(Se_{0.5}Te_{0.5})$, while the medium-dark color region presents a slight deficiency of selenium, with a stoichiometry of $Fe_1(Se_{0.36}Te_{0.64})$; the lighter parts present a lack of iron.

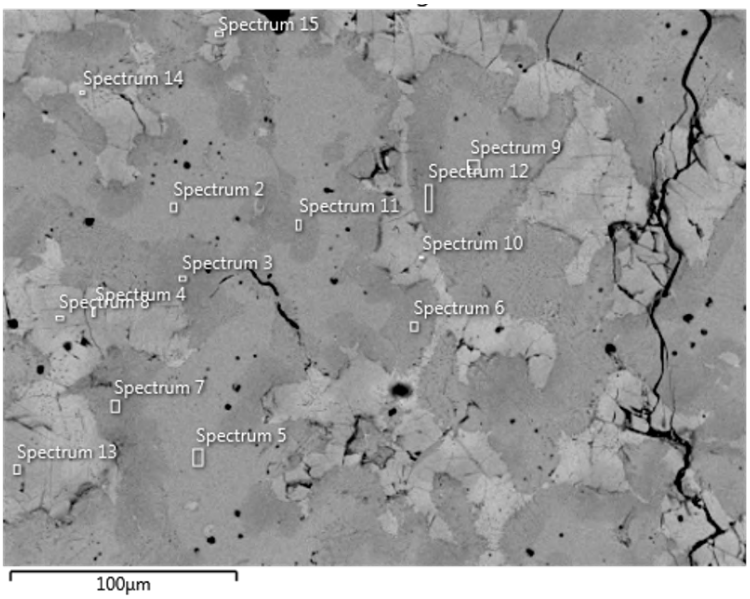

Fig. 3.5: SEM characterization of a Fe(Se,Te) target

We characterized the target with magnetic and transport measurements, with a 4 probe measurement. Figure 3.6 presents susceptibility and resistance: the temperature dependence of the ZFC susceptibility, together with the resistivity of the sample, highlight a critical temperature $T_c^0 = 12K$, comparable to what reported previously by our group, as in [39].

Targets prepared as described were successfully employed for the preparation of $Fe(Se_{0.5}, Te_{0.5})$ epitaxial thin films.

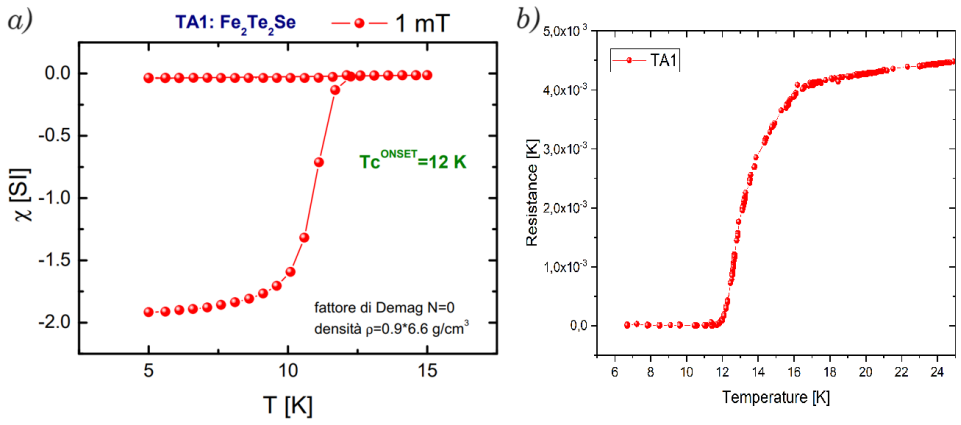

Fig. 3.6: *a)* Temperature dependency of ZFC-and FC susceptibility for a portion of a Fe(Se,Te) pellet measured at $\mu_0 H = 1\ mT$. *b)* Resistivity as a function of temperature of the same sample.

3.1.1 Spark Plasma Sintering

During my stay at Shibaura Institute of Technology in Japan, I had the possibility to use Spark Plasma Sintering (SPS) to prepare $Fe(Se,Te)$ targets. SPS is an innovative method that allows to obtain high-density bulk very rapidly (standard synthesis takes days, SPS can prepare samples in less than one our). The term Spark Plasma Sintering is generally used to identify a sintering technique involving the contemporaneous use of uniaxial pressure and high-intenisty, low-voltage, pulsed current (despite the name, no spark or plasma could be detected so far). This method can be used both to synthesize new compounds and to densify materials in one step. SPS is similar to hot pressing (HIP), but the way the heat is produced and transmitted to the sintering material is different. SPS consists of a mechanical loading system that, at the same time, acts as high power electrical circuit. The material used for tooling is typically highly conductive (we used graphite), so low voltages are able to produce high currents, leading to efficient Joule heating. Figure 3.7 displays a scheme of an SPS apparatus.

The compact geometry of dies and punches allows sintering cycles with heating rate as high as $1000°Cmin^{-1}$, reducing significantly the total duration of the process and thus energy costs. At the same time, the simultaneous application of an uniaxial mechanical pressure enhances densification. The process can take place under vacuum or protective gas at atmospheric pressure, and the process is controlled by temperature measurements (using

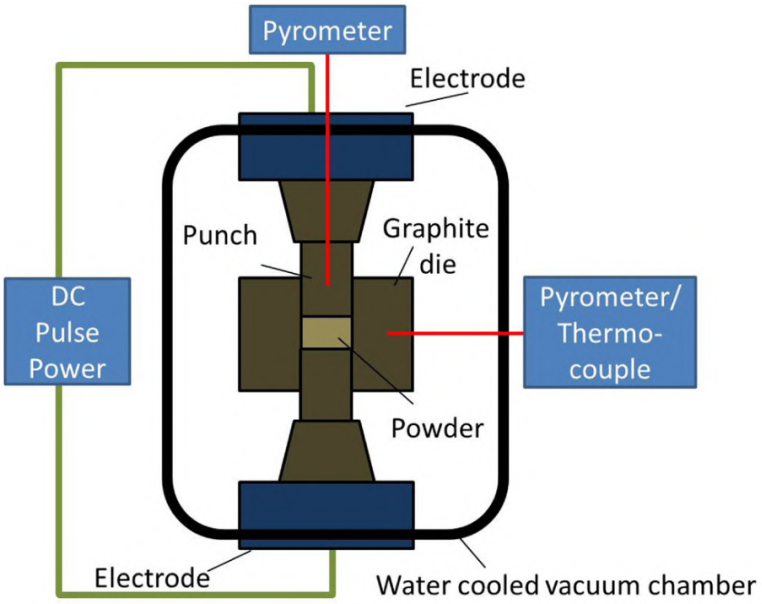

Fig. 3.7: Working schematic of a SPS apparatus. [40]

pyrometers or, as in our case, thermocouples), even if it can also be achieved by other methods, such as power or current control [40].

I prepared Fe(Se,Te) bulk samples starting from the powders described in the previous section. I filled the 1.5 cm diameter graphite die with $7g$ of powders (given the phase density of $7gcm^{-2}$) to obtain a cylindrical pellet of 1.5 cm in diameter and 0.5 cm high. A pressure of 45 MPa was applied, and the sample was the heated at $700°C$ for 15 min. The obtained pellets are very dense, and present a good magnetic transition, comparable with the target prepared as described in section 3.1, as shown in figure 3.8.

3.2 Fe(Se,Te) deposited on Single Crystal Substrates

First step to study iron selenium tellurium thin films, in view of fabbrication of coated conductors, is studying the phase deposited on single crystals: the simplest substrate. This is the simplest type of substrate because it is perfectly oriented (as we have seen, the material needs to be very well oriented in order to have good superconducting properties). The choice of single crystal substrate is related to the lattice parameter match between substrate and deposited phase. The most suitable are, as stated in sec-

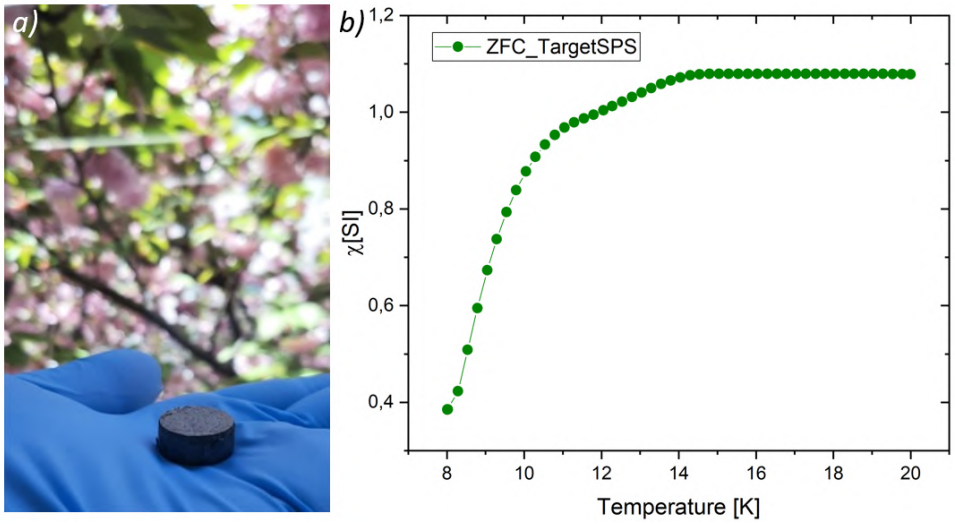

Fig. 3.8: *(a)* Picture of a Fe(Se,Te) target prepared via Spark Plasma Sintering and *(b)* Magnetic transition of Fe(Se,Te) bulk prepared via SPS.

tion 2.4, magnesium oxide (MgO, $a = 4.217$Å), strontium titanate ($SrTiO_3$, $a = 3.905$Å),lanthanum aluminate ($LaAlO_3$, $a = 3.789$Å), yttria stabilized zirconia (YSZ, $a = 3.637$Å), lithium fluoride (LiF_2, $a = 4.020$Å) and calcium fluoride (CaF_2, $a = 5.462$Å). The study of the growth of FST on such different substrates was already performed in previous works, as described in section 2.4. In this thesis I focused on the deposition on CaF_2 which resulted to be the best substrate for the grow of Fe(Se,Te): I obtain thin films (typically around 100 nm thickenss) with optimal superconducting properties, and very low anisotropy, as mentioned in section 2.4. I optimized the deposition condition, obtaining very reproducible samples. Typical XRD $\theta - 2\theta$ pattern is shown in figure 3.9*(a)*: only *(00l)* peaks are present, meaning that the film is oriented along the c-axis direction. Rocking curves performed on those samples show low full width half maximum (FWHM), implying that most of the grains are perfectly oriented (very low miorientation angles). Figure 3.9*(b)* plots the temperature dependence of the resistance on a thin film deposited on CaF_2 single crystal. Films are quite reproducible, and the T_c onset can be as high as 21 K with a delta T_c of less than 1 K.

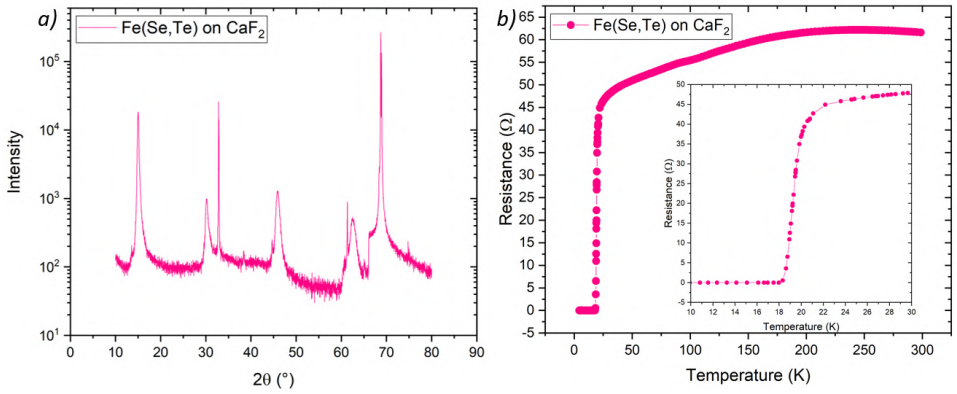

Fig. 3.9: (a) XRD $\theta - 2\theta$ pattern and (b) resistance-temperature measurements of a Fe(Se,Te) film grown on CaF_2 single crystal.

Optical photolitography

In order to carry out different measurements, such as magneto-optical analysis, resistivity, or critical current measurement, we realize special patterns on the surface of the sample in order to have a defined geometry. Sample portioning is also useful when samples are irradiated: partial sample irradiation allows us to evaluate the effect of the irradiation itself, without including possible effects on sample reproducibility. Figure 3.10 illustrates different patterns we impress on samples. Different geometries are intended for different purpose, for example, hall bars (of various shapes and sizes) are essential for resistivity calculation and critical current measurements (we need a thin bridge to assess critical current, with a very sharp geometry), while a pattern made of squares is very useful for magneto-optical analysis.

The typical Hall-bars employed in this thesis had a channel of $20 \times 50 \mu m^2$ and were obtained by thin film patterning based on UV photo-lithography, Thick photorestist (SPR220) was deposited by drop casting on top of the samples, followed by spin coating at 6000 RPM. Final resist thickness was about 4.5 µm. The resist was then hardened by soft backing at 115 C for 120s. Device geometries were transferred by UV mask lithography. Resist cross-linking in the exposed regions made it soluble in a ammonia-based developer, leaving parts of the film unprotected versus the following etching step. Thin film etching relied on Ar ion milling, a physical etching method which has the critical advantage of not having chemical selectivity, since the removal of the material is based on transferred momentum of the incoming

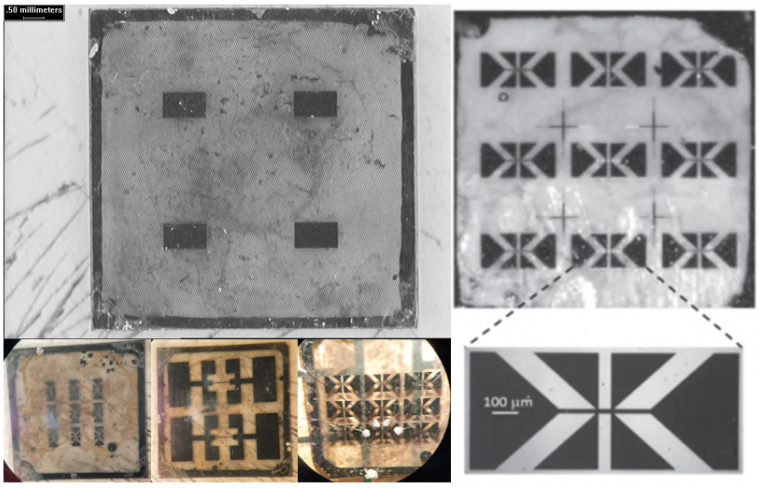

Fig. 3.10: Examples of different pattern, both for magneto-optical and transport measurements.

atoms. Ar ions are accelerated up to an energy of 500 eV, with a current flow of about 0.25 mA/cm^2. The typical etching time for a 100 nm film was of about 10 min. After the etching step the samples were cleaned in a acetone bath heated to 50°C to ease the removal of the resist residues. Finally, they were put soaking in pure ethanol and dried under nitrogen flow.

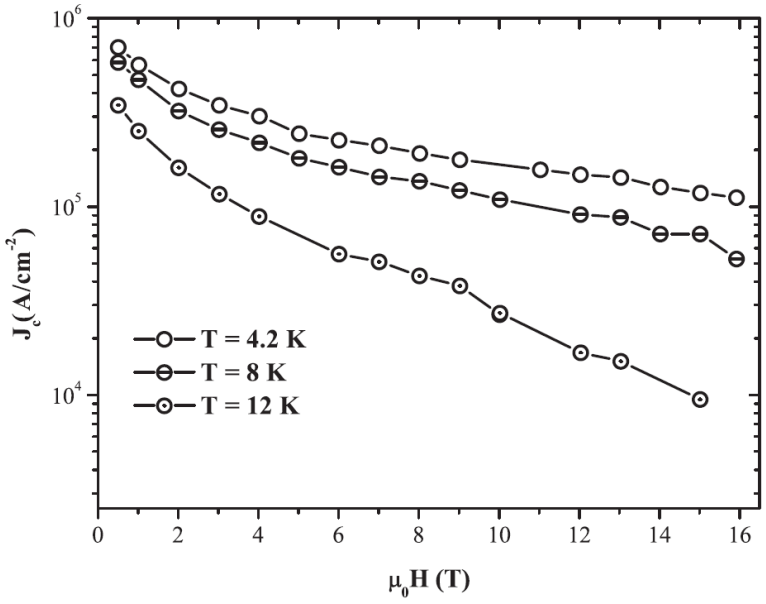

Fig. 3.11: Critical current J_c versus magnetic field up to 16 T at 4.2 K, 8 K, and 12 K.s [41].

Figure 3.11 presents typical critical current density for a film deposited on CaF_2 single crystal. This graph highlights a fundamental characteristic of the phase: J_c shows a very slight decrease as the applied magnetic field increases.

3.2.1 Seed Layer

S. Molatta et al [42] reported that the growth of a seed layer between the substrate and the superconducting film both enhance the crystal and chemical matching between substrate and film, and allows a lower deposition temperature of the phase (significant step towards process simplification and costs reduction of FeSeTe deposition). The seed layer consists of a $FeSe_{0.5}Te_{0.5}$ film presenting worse superconducting properties (i.e. lower T_c, if not the total absence of a superconducting transition), but high quality structure. The growth of the film on the seed layer can be considered substantially homoepitaxial.

We studied the properties of the phase in function of the deposition temperature, in order to optimize the seed layer. Figure 3.12 compares the superconducting transition and the XRD patterns of five films, deposited via PLD on CaF_2 single crystals with a laser frequency of $3Hz$, at different temperatures, ranging from $220°C$ to $450°C$. In panel 3.12(a) we can see the critical temperature is higher when deposition temperature is equal to $300°C$, worsening with both the reduction and the increase of it. Panels 3.12 (c) to (e) show that the FWHM of the rocking curves is lower when the deposition temperature increases, meaning that the out of plane orientation is strongly affected by the deposition temperature: the higher the temperature, the better the orientation.

Optimized deposition conditions for the seed layer were found to be: deposition temperature of $400°C$ and frequency of the laser at 10Hz.

On the seed layer we deposited films at $220°C$ using two different procedures: deposition of the seed layer followed by cooling of the substrate and then deposition of the film, or deposition of the seed layer immediately followed by the deposition of the film during the cooling. In this last case it is possible to assume that an intermediate layer between the seed layer and the superconducting thin film is formed during the cooling of the sub-

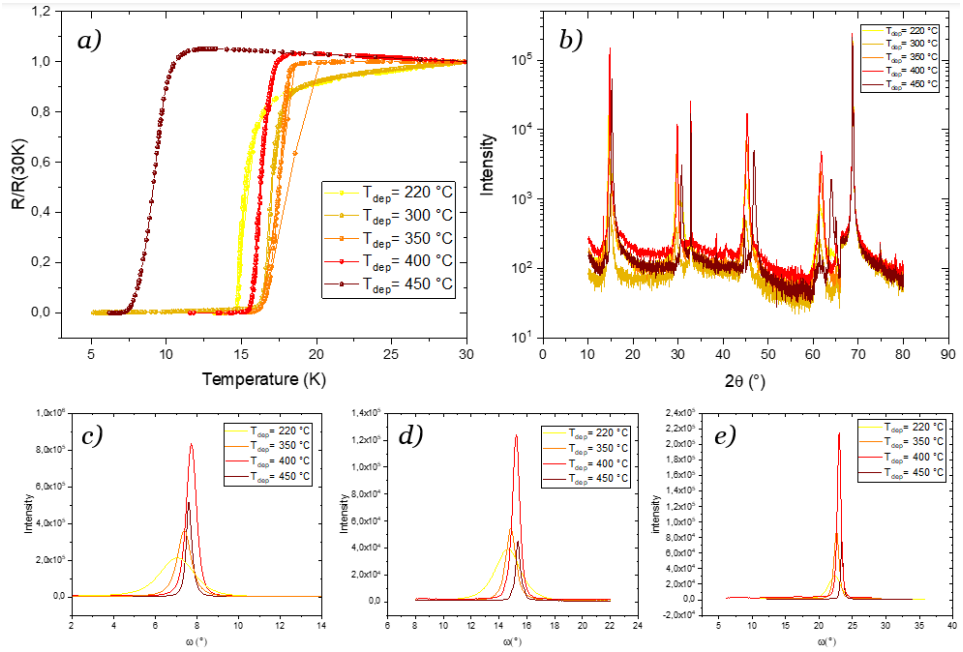

Fig. 3.12: (a) Superconducting transition, (b) $\theta-2\theta$ pattern, (c), (d), (e) rocking curves on Fe(Se,Te) 001, 002, 003 peak respectively, for five samples grown at temperature deposition in a range between $220°C$ and $450°C$

strate; this second solution resulted to be more effective in improving the superconducting properties of the films.

3.3 Single Crystal substrates with CZO buffer layer

Zr-doped CeO_2 (CZO) is grown in ENEA on yttria-stabilized zirconia (YSZ) single crystals using metal-organic decomposition (MOD): CZO precursor solution is prepared dissolving stoichiometric amounts of Ce (III) acetate hydrate and $5mol.\%$ Zr (IV) acetylacetonate in propionic acid. Water and excess of solvent are removed by rotary evaporation: a total metal concentration $[Ce]+[Zr] = 0.3$ M is needed. The solution is then deposited on YSZ single crystal substrate by spin coating and dried for 5 minutes at $120°C$ in air. Finally, samples are thermally treated in flowing 5% $Ar-H_2$ (pyrolysis in air for 30 minutes at $450°C$ and crystallization for 30 minutes at $950°C$ in $0.5l/min$ $Ar-H_2$). The thickness of the obtained samples is around 30 nm. [43]

Fe(Se,Te) deposition on these buffer layer performed in the same way as on

the other single crystals wasn't successful at first, in particular the critical temperature was much lower than that of samples deposited on single crystals: below $10K$, with a enlarged transition, as can be seen from figure 3.14(b), red hollow dots curve.

The deposition of the seed layer between the CZO buffer and the film (described in section 3.2.1) allows the superconductive properties of samples to be greatly improved: by promoting the matching between the substrate lattice and the superconducting film lattice, it helps to achieve critical temperatures comparable to those of films deposited on single crystals.

Figure 3.13 compares the structural analysis of two Fe(Se,Te) films deposited with or without seed layer, on YSZ single crystal substrate with a CZO buffer layer on top. X-rays diffraction $\theta - 2\theta$ patterns show intense ($00l$) Fe(Se,Te) reflections only, together with CZO peaks, confirming the optimal epitaxial growth of the films on these substrates. Peaks of the buffer show a slight shift of 0.1° towards lower angles, suggesting a small oxygen loss during deposition in ultra-high vacuum. Regarding Fe(Se,Te), peak positions among different samples are slightly different, that, together with the dual-phase nature of the film with seed, suggest that in different conditions phases with different lattice parameters are obtained. Since the lattice parameter is linked to the Se:Te ratio (Se-rich lattice are characterized by a lower interplanar distance), we can relate the peak position to the Se:Te ratio. In the case of the film grown on seed, the higher-angle peak is attribute to the seed. The increase of deposition temperature up to $400°C$ enhances the peak shift, suggesting that the Se:Te ratio of the seed layer is higher. This can be ascribed to a progressive tellurium loss with temperature, due to the strong decrease above $350°C$ of the sticking factor of Te atoms arriving at the substrate surface. On the other hand, peaks attributed to the films deposited at lower temperature are shifted towards lower angle, in a position comparable to bulk material. Therefore, the role of the seed layer is not only to promote a sharp crystallinity of the films, but also to preserve stoichiometry transfer from target to film if deposition temperature as low as $220°C$ are considered.

Figure 3.14 compares the electrical characterizations of the two films, compared to a standard on CaF_2 single crystals. The film grown on CZO without seed shows a superconducting transition with $T_c^{onset} = 9.5$ K and $T_c^0 = 6.3$ K, that is a broad transition of $\Delta T_c = 2.6$ K. On the other hand, the

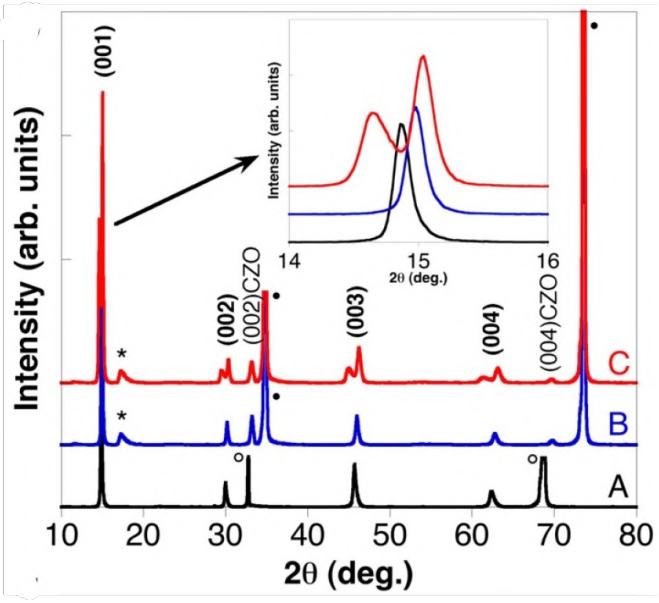

Fig. 3.13: XRD analysis of Fe(Se,Te) films grown on CZO-buffered YSZ substrate without (blue, B) or with (red, C) seed layer. Reference Fe(Se,Te) film deposited on CaF_2 (black, A) is shown for comparison [44].

film with the seed layer shows a quite sharp transition, about 0.5K, with $T_c^{onset} = 17.2$ K and $T_c^0 = 16.7$ K, very similar to the on of the reference ($T_c^{onset} = 18.6$ K and $T_c^0 = 17.6$ K) of a film grown on CaF single crystal. We can conclude that the presence of a seed layer significantly improve the properties of the superconducting film. [44]

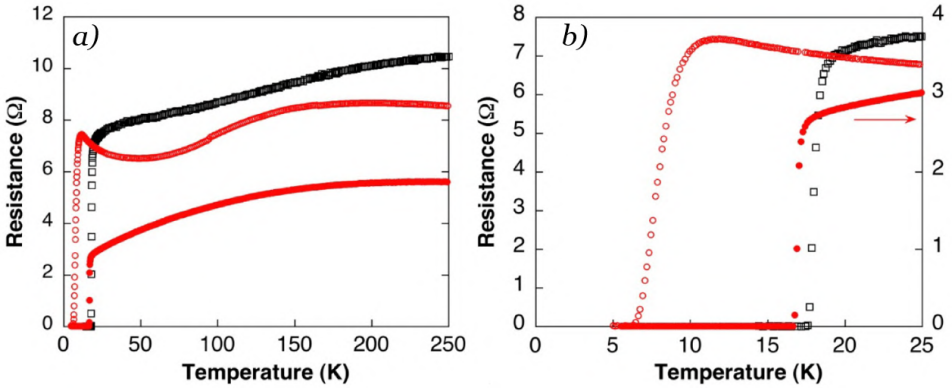

Fig. 3.14: (a) Behaviour of the electrical resistance as a function of the temperature of Fe(Se,Te) film deposited without (open symbol) or with (full symbol) CZO-buffered YSZ substrate (red circle). Reference Fe(Se,Te) film deposited on CaF_2 single crystal substrate (black square) is shown for comparison. In (b), the detail of the superconductive transition [44].

Figure 3.15 compares the $J_c(H)$ curves for a film grown on CZO-buffered YSZ single crystal with seed layer to the same curves for a standard CaF_2 single crystal substrate.

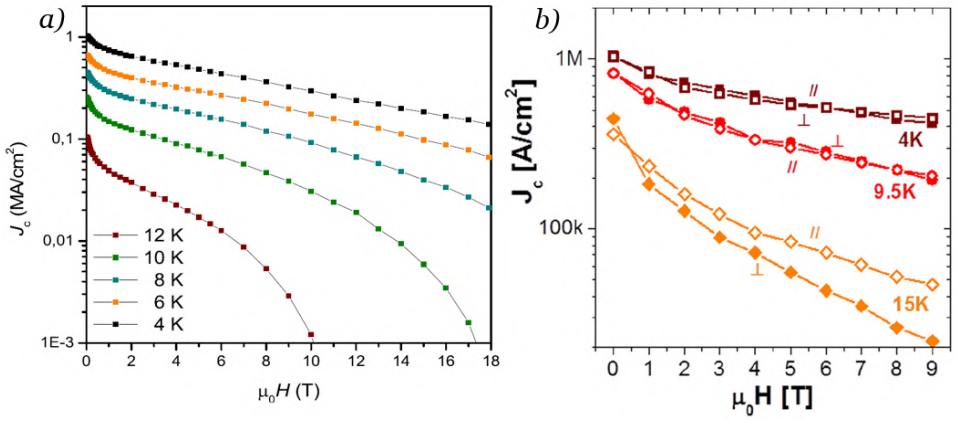

Fig. 3.15: (a) $J_c(H)$ derived from I-V measurements from 4 to 12 K of Fe(Se,Te) film (seed layer+top layer) deposited on CZO buffer layer [43]. (b) [34] For comparison, $J_c(H)$ at 4, 9.5, and 15 K for a film deposited on CaF_2 $H \parallel ab$ (hollow symbols) and $H \perp ab$ (full symbols).

From this comparison we can assert that the seed layer helps achieving critical current densities comparable with those of samples deposited on single crystals.

TEM analysis

In order to better understand the growth of the Fe(Se,Te) film on the CZO buffer layer, TEM analysis have been performed at CNR-IMM institute.

Figure 3.16 shows TEM images of sample grown on a CZO-buffered YSZ single crystal. Figure 3.16(a) presents the cross section of the sample at the bottom we can see the single crystal YSZ on which the CZO layer has grown, and above it the Fe(Se,Te) in which we can see a first layer corresponding to the seed and a second layer corresponding to the actual film. On top is a layer of passivated Fe(Se,Te). Figure 3.16(b) shows the magnification of the interface between Fe(Se,Te) and buffer CZO; it can be seen that the growth of the superconductor is perfectly ordered in the ab-plane, even though the grain boundary of the buffer layer is not perfectly aligned. Finally, figure 3.16(c) TEM image showing the perfect growth of Fe(Se,Te) on a part of the buffer oriented in the ab plane.

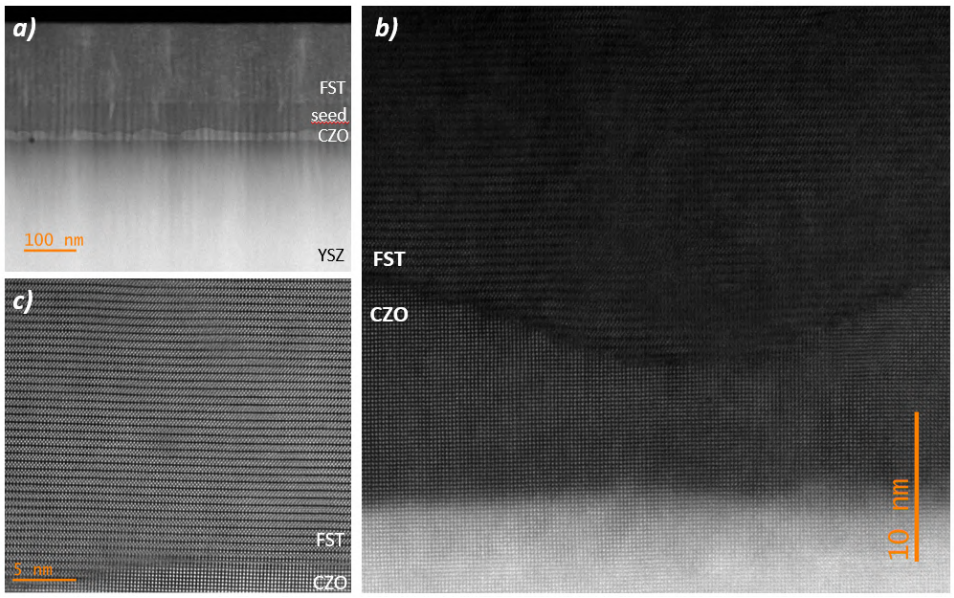

Fig. 3.16: TEM images of a Fe(Se,Te) film deposited on CZO-buffered YSZ single crystal. (a) Cross section of the sample. At the bottom we can see the single crystal YSZ on which the CZO layer has grown, and above it the Fe(Se,Te) in which we can see a first layer corresponding to the seed and a second layer corresponding to the actual film. On top is a layer of passivated Fe(Se,Te). (b) Magnification of the interface between Fe(Se,Te) and buffer CZO; it can be seen that the growth of the superconductor is perfectly ordered in the ab-plane, even though the grain boundary of the buffer layer is not perfectly aligned. (c) TEM image showing the perfect growth of Fe(Se,Te) on a part of the buffer oriented in the ab plane.

3.4 Metallic Templates

After proving the feasibility of the buffer on single crystals, CZO is deposited on NiW(5%wt.) cube-textured tapes by MOD, according to what described in section 3.3, by ENEA.

Figure 3.17 shows XRD $\theta - 2\theta$ pattern of the buffer layer grown on NiW oriented substrate: intense (002) and (004) peaks emerge, with a minor (111) reflection. Out of plane orientation of the buffer is in line with the substrate, with a FWHM of 7° in transverse direction (insert of figure 3.17) [46].

EBSD maps (figure 3.18(a)) shows that Zr:CeO_2 film reproduces NiW microstructure; within each NiW grain the misorientation is below 2° and visible grain boundaries are basically those of the substrate.

Figure 3.19 compares AFM analysis of a Zr:CeO_2 film grown on a YSZ single crystal and NiW substrate respectively. In both cases the film is ($00l$)

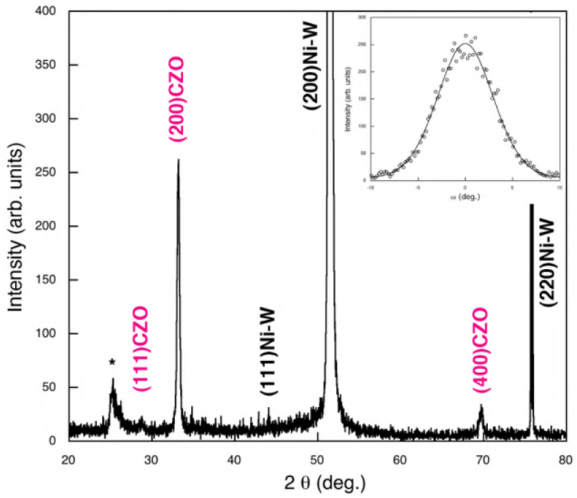

Fig. 3.17: XRD $\theta - 2\theta$ spectrum of Zr : CeO_2-buffered Ni-W substrate deposited by MOD. Asterisk mark instrumental artifact. In the inset, (200) Zr:CeO_2 ω scan in TD.

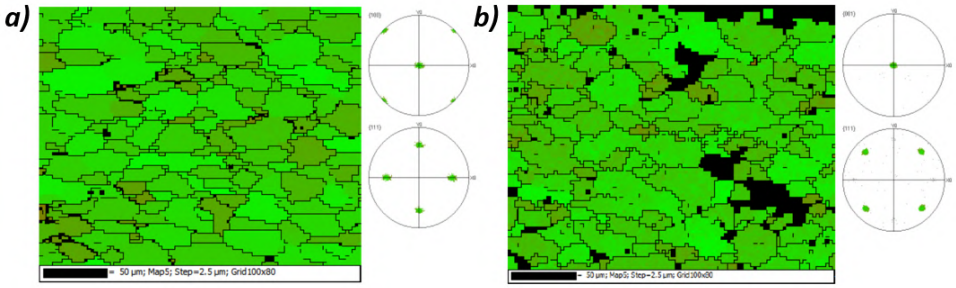

Fig. 3.18: EBSD misorientation map and (200) (top) and (111) (bottom) pole figures of (a) Zr:CeO_2-buffered Ni-W substrate deposited by MOD and (b) of Fe(Se,Te) film grown on Zr:CeO_2-buffered Ni-W substrate. Color indicates deviation from the exact 100<111> orientation (light green). Black lines are grain boundaries above 2° (thin line) and 10° (thick line). Black regions are without EBSD pattern.

oriented, with low values of FWHM. The film morphology is made up of flat, irregularly-shaped grains; typical film roughness is 3 nm (rms).

A fundamental role of the buffer layer is to act as a chemical barrier to prevent poisoning of the superconductor. The nickel present in the substrate tends to migrate into the film during deposition, destroying the superconducting properties of the sample [45]. It is therefore necessary to ensure that Ni does not diffuse through the buffer layer.

I performed X-ray photoemission spectroscopy (XPS) analysis on different samples: a Zr:CeO_2 film on NiW "as grown", and a twin sample that was previously heated up in the PLD chamber, to simulate the thermal treatment

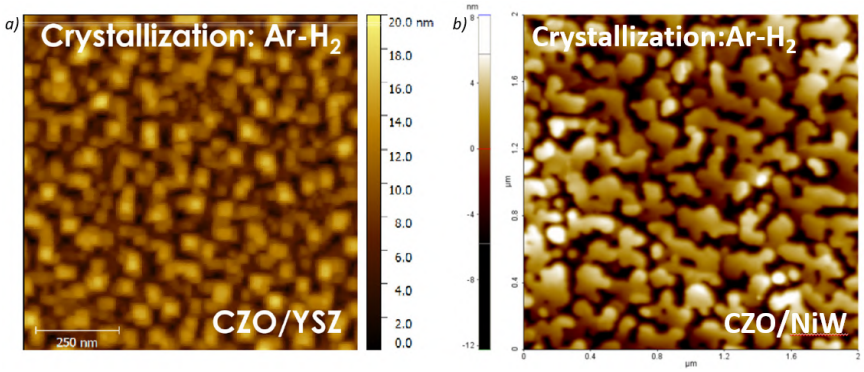

Fig. 3.19: Comparison of AFM on CZO buffered YSZ (a) and CZO-buffered NiW (b). [43]

the substrate is subjected to during the deposition of the Fe(Se,Te) film. Moreover, I analysed via XPS a Fe(Se,Te) sample deposited on a $Zr{:}CeO_2$ buffered NiW tape.

The composition of the surface of the as-prepared sample, the annealed sample, and the Fe(Se,Te) film was investigated using XPS. The XPS instrument is equipped with a hemispherical energy analyzer (model 10-360) and a monochromatic X-ray source (model 10-610) by Physical Electronics. The base pressure of the system is lower than 5×10^{-8} mbar. All the XPS spectra reported were acquired using a monochromatized Al-Kalpha X-ray source (photon energy h_ν=1486.6 eV), the spot was approximately 100 μm diameter, and the photoemitted electrons were collected at an emission angle of 45° from the surface normal.

To evaluate the CZO film's quality and efficacy as a buffer layer, XPS measurements were conducted to analyze the chemical composition of the CZO layer's surface. Additionally, we subjected the tape with CZO deposition to the same heat treatment used for the deposition of the Fe(Se,Te) seed layer. Specifically, the substrate was heated from 300 to 500 K at a linear heating rate of 8 K/min and held at 500 K for 15 minutes. The thermal treatment occurred under vacuum at a base pressure lower than 5×10^{-7} mbar. The position of the element's peak was retrieved from the NIST X-ray Photoelectron Spectroscopy Database [47].

The binding energy was aligned using the C 1s line at 284.40 eV. Moreover, the spectra were shifted vertically for clarity. A Shirley background was considered for the spectra. To determine the energy, the peaks were fitted

with a Doniach Sunjic. All the analyses on the spectra were performed using the city software [48].

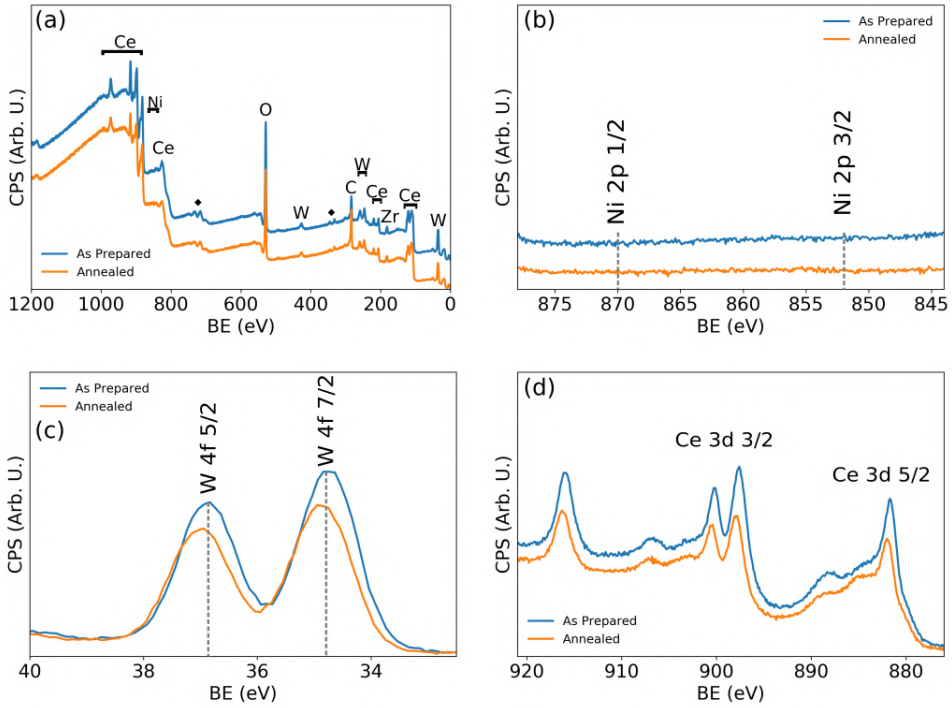

Fig. 3.20: XPS spectra for two CZO films deposited on NiW, the blue line refers to the as prepared, while the orange line to the sample heated up to simulate the thermal treatment that takes place before the deposition. Panel (*a*) shows the survey for the two samples, while panel (*b*), (*c*) and (*d*) are a enlargement of the zone corresponding to the peaks of Ni 2p, W 4f and Ce 3d, respectively.

In panel (*a*) of figure 3.20, the survey spectra of the as-prepared and annealed samples are compared. As it can be seen, they show the presence of the component of the CeO_2-Zr doped buffer layer, and there is no noticeable difference between the spectra of the as-prepared and annealed states, emphasizing the robustness of the buffer layer to the necessary thermal treatments. Panel (*c*) displays the high-resolution spectrum of the *4f* region for the tungsten peak. Also in this case, it can be seen that there is no difference between the as-prepared and the annealed state, suggesting that the oxidation state of the tungsten is not influenced by the heat treatment necessary for the deposition of the Fe(Se,Te) seed layer. For the as-prepared state, the energy of the W *4f 7/2* (34.73 eV for the as-prepared and 34.84 for the annealed) and the W *4f 5/2* (36.85 eV for the as-prepared and 36.97 eV

for the annealed), indicating the presence of WO_3 [49]. Additionally, mixed oxides $NiWO_4$ can be excluded [53]. Interestingly, the XPS measurements show the presence, on the CZO surface, of a non-negligible amount of WO_3 (figure 3.20 (*c*)). The same species was observed in a preliminary XPS analysis of the Ni-W bare substrate (performed by colleagues in the University of Roma Tre) and the high reactivity of Ce with W for the formation of a mixed oxide is well known [50], but its presence on the buffer surface is somewhat puzzling, due to the limited diffusion of W in CeO_2 [51], [52]. While the segregation of WO_3 on the surface of Ni-W can be explained by the natural reactivity of a metallic surface exposed to air, we can only speculate that high-temperature diffusion at the grain boundaries plays a significant role in its migration to the buffer surface. However, its presence does not interfere with the heteroepitaxial growth of the CZO buffer, and neither for the FST film (as we will see in figure 3.21). The high-resolution spectra of the Ce *3d* region are shown in panel (*d*) of figure 3.20. As indicated for the other spectra, in this case, the chemical state of the buffer layer is not influenced by the heat treatment, highlighting once again the robustness of the buffer layer concerning thermal treatments. According to the energies of the peaks and with the analysis by Maslakov et al. [54], they can be ascribed to the CeO_2 oxide. Finally, to prove the efficiency of the buffer layer against the Ni contamination, high-resolution spectra of the Ni *2p* region, shown in panel (*b*), were measured both in the as-prepared and annealed state. In both cases, the spectra show Ni's absence on the buffer layer's surface. The absence of Ni from the surface is crucial, given its detrimental impact on the Fe(Se,Te) film [45]. The CZO can efficiently protect the Fe(Se,Te) film from Ni poisoning.

To further confirm the validity of the CZO film as a buffer layer on this type of substrate, I also performed XPS analysis on the surface of the as-deposited Fe(Se,Te) film, to investigate the chemical composition.

As shown from the survey spectra of figure 3.21 panel (*a*), only the Fe, Se, and Te peaks can be recognized (alongside the oxygen and carbon peaks coming from atmospheric contamination). To confirm the absence of nickel on the surface of the Fe(Se,Te) film, high-resolution spectra of the Ni *2p* region were measured. As evident from these measurements (figure 3.21(*b*)), the absence of nickel on the film's surface is shown, validating the effective-

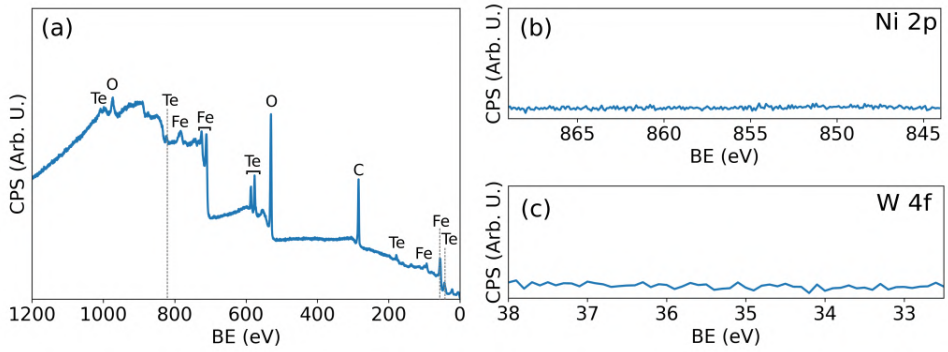

Fig. 3.21: XPS spectra for a Fe(Se,Te) film deposited on a CZO-buffered NiW tape. Panel (a) shows the survey for the sample, while panel (b) and (c) are a enlargement of the zone corresponding to the peaks of Ni 2p and W 4f, respectively.

ness of the buffer layer as a diffusion barrier for nickel. Additionally, high-resolution spectra were measured for the W *4f* region to ensure no diffusion of tungsten atoms from the surface layer of the CZO layer through the film. The results presented in panel (c) confirm the absence of W contamination in the surface layer of the Fe(Se,Te).

The continuity of the $Zr{:}CeO_2$ film has been checked with SEM imaging, to exclude the presence of cracks or holes. Being the film continuous, and without Ni on the surface, I proceeded depositing a Fe(Se,Te) superconducting thin film, together with a seed layer, above the $Zr{:}CeO_2$ buffer. In figure 3.22 $\theta - 2\theta$ XRD pattern of the film is presented; the pattern shows (*00l*) Fe(Se,Te) peaks only (both of the seed and the superconducting film). FWHM of (001) Fe(Se,Te) in TD is 6.6°, in line with both $Zr{:}CeO_2$ and $Ni - W$ orientation.

EBSD analysis, performed in ENEA, in figure 3.18(b) shows a microstructure similar to the one observed in the buffer layer, reproducing Ni-W substrate ones. Sometimes regions without EBSD pattern occur, corresponding to whole substrate grains. They are characterized by a more disordered microstructure, compared with oriented regions in which Fe(Se,Te) grain boundaries are hardly visible. These regions are likely connected with $Zr{:}CeO_2$ film regions showing poor orientation mentioned above.

I characterized the optimized sample on metallic template, measuring the resistivity as a function of the temperature. The transition is shown in figure 3.23.

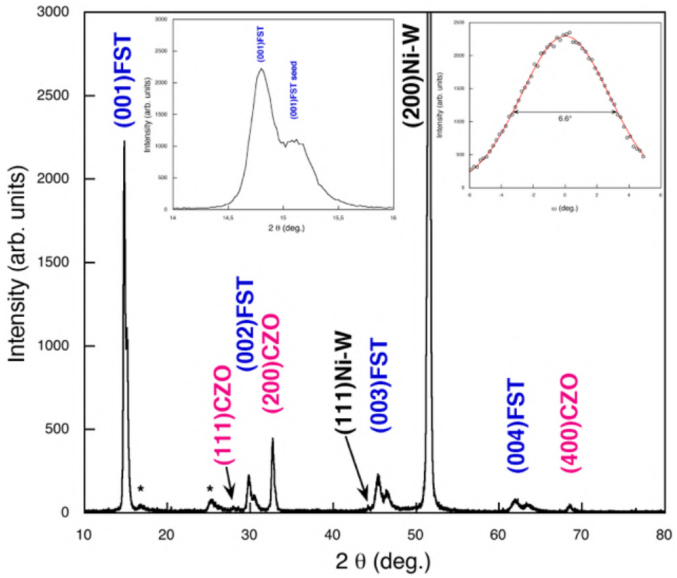

Fig. 3.22: XRD $\theta - 2\theta$ spectrum of Fe(Se,Te) film grown on $Zr{:}CeO_2$-buffered Ni-W substrate. Asterisks mark instrumental artifact. In the insets, detail of (001)Fe(Se,Te) peak (left) and its w scan in TD (right).

This is the first sample that presented a superconductive transition. The critical temperature $T_c^0$is around 11.5 K; it is lower than that of the film deposited by Sylva at al. [27] on NiW tape with a PLD CeO_2 buffer layer, 250 nm thick. However, this is a great result because with a much thinner buffer layer, we obtained superconducting samples.

As for the onset of the critical temperature, this parameter is more difficult to interpret because of the bump that occurs before the transition. The origin of this bump is probably due to the metallic nature of the substrate and the contacting method used for these samples. In particular, I made the contacts for these samples using a bonder, a device that uses ultrasound to weld a thin wire, in my case a silver wire, to the sample.This operation, which is slightly invasive, has the effect that the wire reaches the substrate directly, i.e. it penetrates both the superconducting film and the buffer. In this configuration, when the superconductor is in its normal state, the current will tend to pass entirely through the metal tape. However, when the superconductor begins its transition and its resistance becomes competitive with that of the NiW, the current will tend to split between the two layers. However, the resistance measurement is evaluated by considering the total current flowing through the film. This explains why a resistance spike can

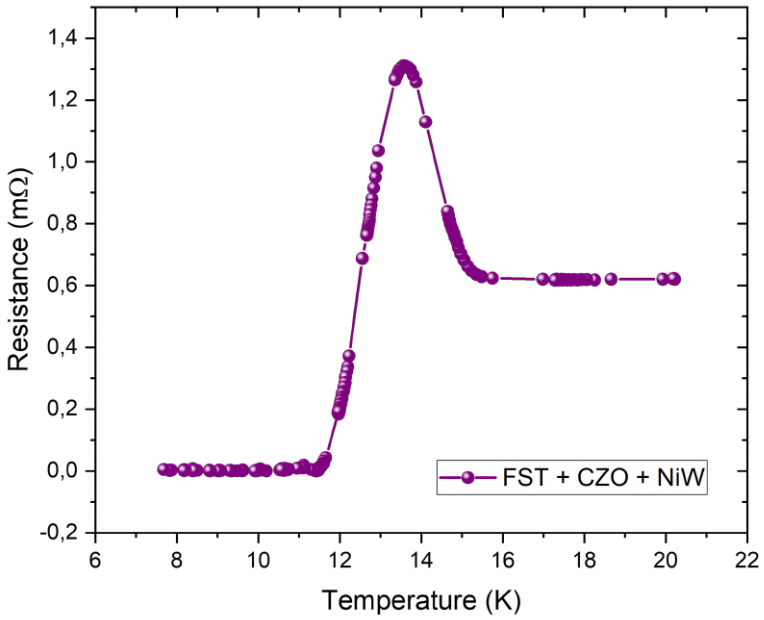

Fig. 3.23: Resistivity as a function of the temperature for the first superconducting sample deposited on CZO-buffered NiW tape.

be observed, which is simply an artefact of the measurement.

According to [27], buffer thickness plays a fundamental role in improving the superconductor properties; in fact, comparing the superconducting transition of a film deposited on 150nm-thick CeO_2 PLD buffer layer and on a 350nm-thick, the latter only reaches zero resistance. A weak point of any chemical route deposition, compared to physical ones (i.e. PLD), is the maximum achievable thickness of the films, much lower in the former type. In the case of CZO, for a single deposition with MOD, we obtain 25nm films. We performed a study of the superconducting properties of the sample in function of the buffer thickness. Thicker buffers were obtained by repeating the deposition twice, resulting in 40 nm thick layers, while thinner buffers (less than 25 nm) were obtained by reducing the heat treatment time.

Figure 3.24 shows resistivity transition of three films deposited on Zr:CeO_2-buffered Ni-W substrate, with a buffer of 40, 25 and less than 25 nm; The thicker film used a double dip coating, while the thinner film using a faster treatment.

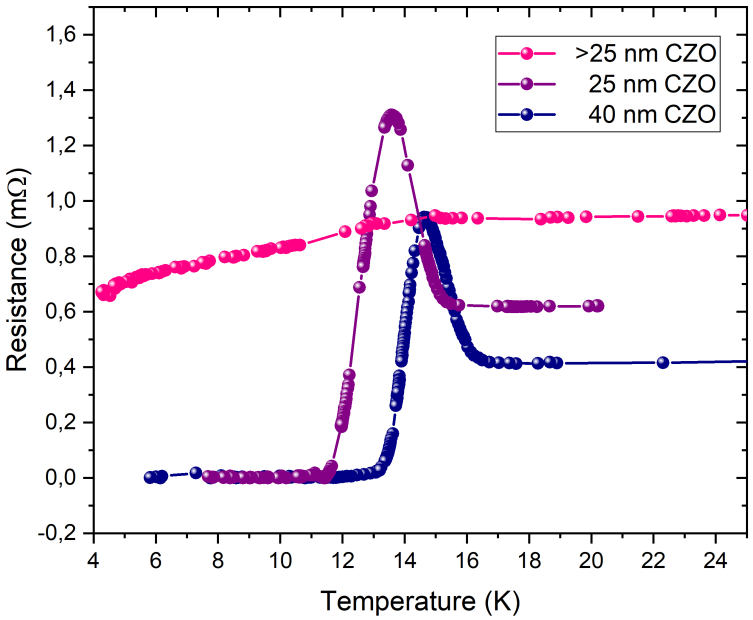

Fig. 3.24: Resistivity-temperature measurements of unpatterned Fe(Se,Te) films grown on Zr:CeO2-buffered Ni-W substrate, thickness of 40 nm (blu), 25 nm (purple) and less than 25 nm (pink).

From this comparison we can conclude that the thicker the buffer, the higher the critical temperature of the transition. The film deposited on 25 nm buffer, as previously mentioned, exhibits a critical temperature $T_{C0} \sim 11.5$ K, while with a buffer 40 nm thick, T_{C0} rises up to $\sim$ 13 K. Another important result is that a too thin buffer is ineffective for the deposition of a superconducting film: the transition actually disappears when the buffer layer is thinner than 25 nm.

The sample deposited on a "standard" 25 nm CZO buffer was patterned using standard optical photolithography as described in section 3.2, to obtain an Hall bar as in figure 3.25, with a bridge $500\mu m$ wide.

Using a 4 wire measurement, I-V curves have been measured in ENEA at different temperatures and up to 18 Tesla, and the corresponding critical current densities have been extracted using a criterion of 1 $\mu V cm^{-1}$. J_c, shown in figure 3.26, is 10^5 A/cm^2 at 4K and in self field, and it is lowering of about two orders of magnitude in 18 Tesla range. There is much room

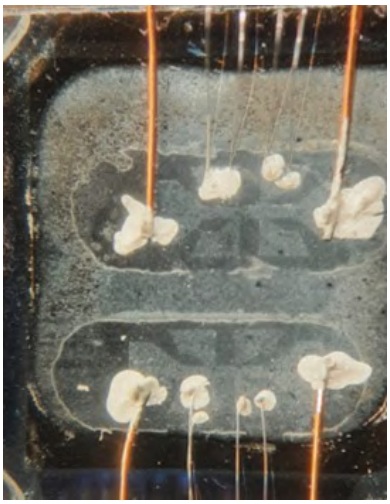

Fig. 3.25: $500\mu m$ wide Hall bar obtained on a Fe(Se,Te) film deposited on a CZO-buffered NiW via optical photolithography

for improvement: this was the first attempt and T_c was relatively low.

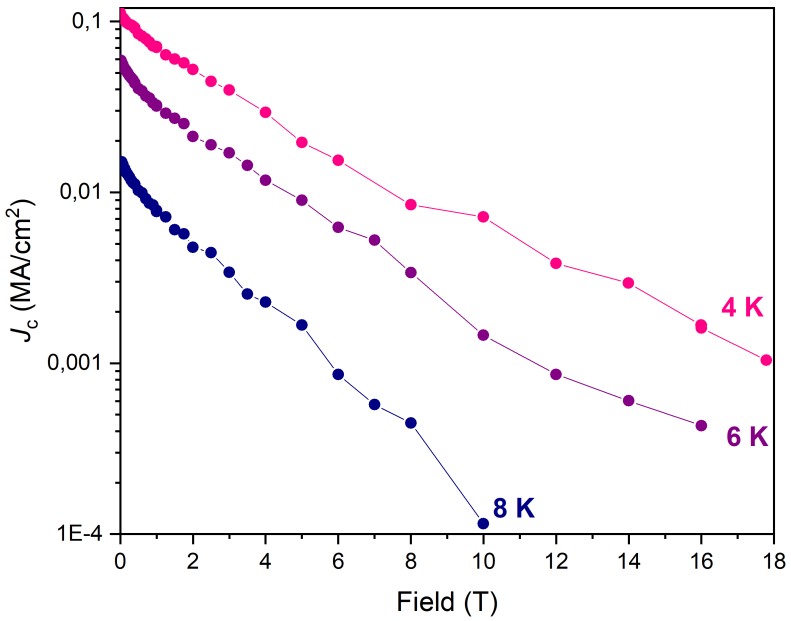

Fig. 3.26: Critical current density of a Fe(Se,Te) film deposited on CZO-buffered NiW tape, as a function of applied field, evaluated at 4.2 (pink), 6 (purple) and 8 K (blue).

What is remarkable is that this is the very first successful attempt of an

entire Fe(Se,Te) home-made Coated Conductor with a very simple buffer layer only 25 nm thick.

Chapter 4

IBS Irradiation: state of the art

Iron Selenium Tellurium can be an appealing candidate for winding magnets for high field. Nowadays, one of the main areas of application of high-field magnets is definitely in fusion plants: the plasma inside a Tokamak is magnetically confined.

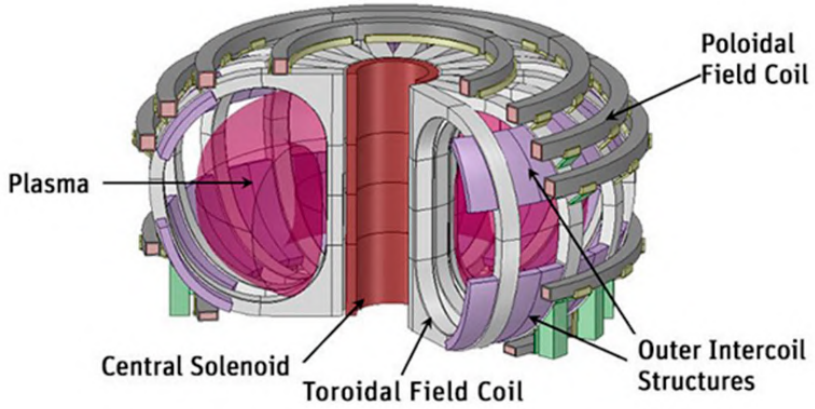

Fig. 4.1: Scheme of a Tokamak for fusion plants. [55]

The environment, when plasma is present, is full of radiation, therefore, understanding the behaviour of the phase under condition of irradiation from different particles is very important.

Superconductors have been irradiated for years, trying to investigate the effects of irradiation with multiple aims: gaining information on fundamental

properties such as gap symmetry and suppression of the critical temperature T_c by impurity scattering [56], investigating vortex physics and flux pinning in view of applications in magnet fabrication [57], and, as mentioned, testing the robustness or deterioration of superconducting properties by irradiation for application in high-energy accelerators or fusion plants.

Irradiation basically introduces defects into the superconductor structure; particle type and energy determine different defect types. Small defects, which enhance the scattering rate of the charge carriers, can be used to perform fundamental studies on superconductors: in iron based superconductors, enhanced scattering provides information on the gap symmetry, a possible sign reversal or nodes in the gap. Larger defects can act as efficient pinning centers for vortices, enhancing the critical current, or diminishing flux creep. It is also been demonstrated that irradiation can be used for improving the critical current in coated conductors on an industrial scale [58]. Finally, irradiation experiments have been carried out to test the suitability of a conductor for operation in a radiation environment.

4.1 Irradiation for Iron Based Superconductors

Due to the different order parameter symmetry of IBS compared to HTS, some of the unconventional pairing drawbacks affecting HTS are less unfavourable in IBS. The effect of impurities is detrimental to T_c in HTS, whereas in IBS the same amount of artificial defects does not affect or may even improve the superconducting properties. Therefore, we can expect iron based superconductors to be harder in a radioactive environment and therefore more suitable for fusion applications.

To verify this hypothesis, it is important to understand the effect that irradiation could have on iron based superconductors.

4.1.1 Correlation between radiation damage and defect structure

Although all defects enhance scattering, a high density of point-like defects is most efficient. Point-like defects are generated by all irradiation techniques, and they are often accompanied by larger defects. Electron irradiation at low temperature is best suited to generate only Frenkel pairs (a vacancy

and an interstitial). Larger defects on the other hand, are more efficient for pinning, especially at high temperature.

Charged Particles

Irradiation experiments on superconductors have been performed with a variety of particles, rest masses ranging from about 0.5 MeV/c (electrons) to around 220 GeV/c (heavy ions); their kinetic energies can range from a few keV to GeV. Charged particles transfer this energy to matter either by interactions via the electronic system or by collision with the nuclei of the lattice. The electronic stopping power S_e dominates for high energy particles, while the nuclear collision contribute the most to the energy loss S_n at low energies. The stopping power is the retarding force acting on charged particles, due to interaction with matter, resulting in loss of particle kinetic energy. It is also interpreted as the rate at which a material absorbs the kinetic energy of a charged particle. S_e generally increases with the particles mass, but is non-monotonous in energy. It has a maximum near the end of the particle's trajectory, where the kinetic energy is comparatively small. Parallel continuous columnar defects with a diameter of few nanometer resulting from local melting are generated at high stopping power, which become splayed at lower stopping power and their diameter is no longer constant along the trajectory. The defects become discontinuous upon a further reduction of S_e, defects elongated along the trajectory and finally nearly spherical defects of few nanometers are formed, which become smaller and irregularly shaped with decreasing stopping power. Electrons, for instance, produce only atomic disorder by displacing single atoms. The penetration depth of heavy charged particles in matter is typically of the order of 20-30 μm, while light particles with very large energies only can penetrate further (centimeter to meter).

Neutrons

Since neutrons are not charged, their stopping power is zero ($S_e = 0$), therefore they interact only via nuclear collision or reactions. While charged particles have a well defined energy in irradiation experiments, defined by the accelerator, neutron sources typically provide neutrons having a wide en-

ergy distribution, In a fission reactor, the neutrons energies can be roughly divided into three groups:

- Fast neutrons: from the fission reaction, they have energies between about 0.1 and 10 MeV;
- Thermal neutrons: they present a Maxwell-Boltzmann energy distribution peaking at about 40 meV;
- Epithermal neutrons: at intermediate energies, they represent moderated neutrons which are not fully thermalized.

Defects can be generated by elastic collisions only if the transferred energy exceeds the binding energy of the lattice atoms (typically a few eV in metals and 10 to 40 eV in ionic crystals), which is maximum (central collision) $\frac{4m_L m_n}{(m_L+m_n)^2}E_n$, with m_L and m_n the mass of the lattice atom and the neutron respectively, while E_n refers to the energy of the incident neutron. Material containing light elements thus suffer more damage from elastic collision than compounds composed of heavy elements (the large amount of oxygen in cuprates could be critical, for example). The realistic minimum energy where defect production due to collision sets in is about 100 eV, thus thermal neutrons do not produce any defects by elastic collisions. If the transferred energy is much higher than the binding energy, (threshold in the order of 1 keV), the displaced atoms collides with other lattice atoms leading to an avalanche-like defect production, which locally melts the lattice. A so-called collision cascade is formed, a spherical defect with a diameter of few nanometers. The collision cascades are statistically distributed and the penetration depth of fast neutrons amounts to tens of centimeters in many materials, ensuring a homogeneous defect structure even in bulk samples. The density of this kind of defects is proportional tho the fast neutron fluence, even if it depends ob details of the high energy neutron distribution. High and medium energy neutrons also produce smaller defects, down to single displaced atoms and interstitial. The density of these defects does not scale with fluence, and in general is much larger than the density of the collision cascades at low neutron fluence.

4.1.2 Fundamental properties

Isotropic scattering is usually desired for the investigation of changes of the fundamental materials properties due to increased scattering. If we imagine that isotropic scattering reduces the anisotropy of all properties, most of the observed changes can be understood, like the change of the gap symmetry, the decrease in T_c, or the reduction of the upper critical field.

Pairing symmetry

The pairing symmetry is of primary importance for a theoretical description of unconventional superconductors. The gap symmetry is often addressed indirectly, for instance by the temperature dependence of the superfluid density, THz spectroscopy, thermal conductivity or by the influence of disorder on the transition temperature. Disorder potentially changes the pairing symmetry by making the gap more isotropic, reducing its largest value (which than decrease T_c) and sometimes enhancing his minima: this was demonstrated for MgB_2, where neutron irradiation progressively reduced the larger gap until it merged with the small one [59].

In most of the iron based compounds, s_{+-} pairing symmetry resulting from antiferromagnetic spin-fluctuations is a popular scenario. It is been reported a transformation from s_{+-} to s_{++} symmetry in Co-doped Ba122 by disorder resulting from 200 keV proton irradiation [60].

Transition temperature

Non magnetic scattering is not pair breaking in single band *s-wave* superconductors and thus do not change the transition temperature. Changes in T_c after irradiation, therefore, either result from non-conventional superconductivity or from some second order effects such as changes in the electronic density of states (DOS). Inter-band scattering between different bands or intra-band scattering with anisotropic gaps do not preserve the energy of the particle and consequently reduce T_c. However, pair breaking and a reduction of superconducting energy gap are not the only possible reasons for a T_c reduction caused by irradiation. The newly created defects cause strain and change the lattice parameter, which in turn can lead to a change in the

Compound	**Particles**	**Fluence** ϕ $[m^{-2}]$	T_c^0 [K]	ΔT_c [K]	$\Delta T_c/\Delta\phi$ $[Km^2]$
$Ba(Fe_{0.9}Co_{0.1})_2As_2$ (film)	200keV p	1.8×10^{19}	26	18	10^{-18}
$Ba(Fe_{1-x}Co_x)_2As_2$	3MeV p	2×10^{20}	21.5	1	5×10^{-21}
$Ba(Fe_{0.93}Co_{0.07})_2As_2$	200MeV Au	7.7×10^{15}	24.4	4.6	6×10^{-16}
$Ba_{0.6}K_{0.4}Fe_2As_2$	3MeV p	5.8×10^{20}	38.6	3.5	6×10^{-21}
$Ca_{0.85}La_{0.15}Fe_2(As_{0.92}Sb_{0.08})_2$	3MeV p	10^{20}	34	3	3×10^{-20}
$FeSe_{0.5}Te_{0.5}$ (film)	190keV p	1×10^{19}	18	-0.5	-5×10^{-20}

Table 4.1: Brief comparison of T_c change for different iron based compounds, resulting from irradiation of different charged particles.The samples are single crystals, unless otherwise indicated. [57]

electronic DOS. Strong intra-band scattering can change the DOS as well by smearing the Fermi surface. [61]

For the vast majority of irradiation experiments on iron-based superconductors, a decrease in the transition temperature has been reported, with the exception of one study on K-doped Ba-122, reporting unchanged T_c after 1.4 GeV Pb irradiation [62], and a work on Fe(Se,Te), reporting an increase of the critical temperature when irradiated with low energy protons [63].

A comparison of the changes induced by a particular irradiation is useful for testing the suitability of a given material in the respective environment (fusion, or accelerator magnets), however, a comparison of the material's sensitivity to disorder is difficult to use for drawing conclusions on the underlying mechanism, since the introduced disorder depends on the material itself. The number of displacements per atoms (*dpa*) is a more suitable measure for this purpose. It's been reported ([64]) that the transition temperature scales quite well with the number of displaced atoms in Nb_3Sn, irrespective of the particle type and energy. For a comparison of either materials or different radiation sources (particles, energies) the knowledge of the respective *dpa* is very valuable. The highest damage per particle is introduced in heavy ions. It is however concentrated along the ion's trajectory mainly, forming extended defects. At low fluences, the superconducting matrix between these defects remains nearly undisturbed and the influence on the transition temperature is small. At high fluences, the large dpa number leads to a fast decreace of T_c.

An important parameter is the temperature during the irradiation process.

Compound	ξ [nm]	λ [nm]	J_d $[10^{10} Am^{-2}]$	G_i	η [%]	$\phi_n t$ $10^{21} m^{-2}$
$Ba(Fe_{0.94}Co_{0.06})_2As_2$	2.35	240	74	2.5×10^{-4}	2.3	3.6
$BaFe_2(As_{0.7}P_{0.3})_2$	2.7	182	110	9×10^{-5}	2.4	3.6
$Ba_0.6K_0.4Fe_2As_2$	1.5	200	170	8×10^{-4}	3.4	3.6
$NdFeAsO_{1-x}F_x$	1.5	200	170	3.5×10^{-2}	0.8	3.7
$FeSe_{0.5}Te_{0.5}$	1.2	560	26	5×10^{-3}	0.32	1.8

Table 4.2: Magnetic penetration depth, coherence length, depairing current density, Ginzburg number and pinning efficiency after neutron irradiation to the given fluence. [57]

In situ defect annealing (i.e. recombination of Frenkel pairs) increases with temperature, local melting and/or phase decomposition on the other hand is favored by high temperature.

Upper critical field

A reduction in mean free path of the charge carriers leads to an increase of the upper critical fields in isotropic *s-wave* superconductors; thus, scattering induced by the defects resulting from irradiation should increase the upper critical field. The mean free path of the charge carriers has to be similar or smaller than the clean limit coherence length for a significant change in B_{C2}. Being the typical coherence length ξ only few nanometers (around 2, see table 4.2) for iorn-based superconductors an even smaller value of the mean free path seems incompatible with the pair-breaking effect of non-magnetic impurities in these materials, and one can expect only a weak effect on the upper critical filed. Indeed, only small changes in upper critical field were observed after irradiation, and the positive effect of an increase in scattering has to compete with the accompanying decrease of the transition temperature. The anisotropy of B_{C2} is reduced, in accordance with the general trend that scattering makes the material more homogeneous.

4.1.3 Critical currents

Irradiation changes the defect landscape in superconducting materials: this can be useful to investigate the resulting change of the flux pinning behaviour and the critical current densities.

Figure 4.2 presents the field dependence of J_c in different compounds at various temperatures and its change after neutron iradiation.

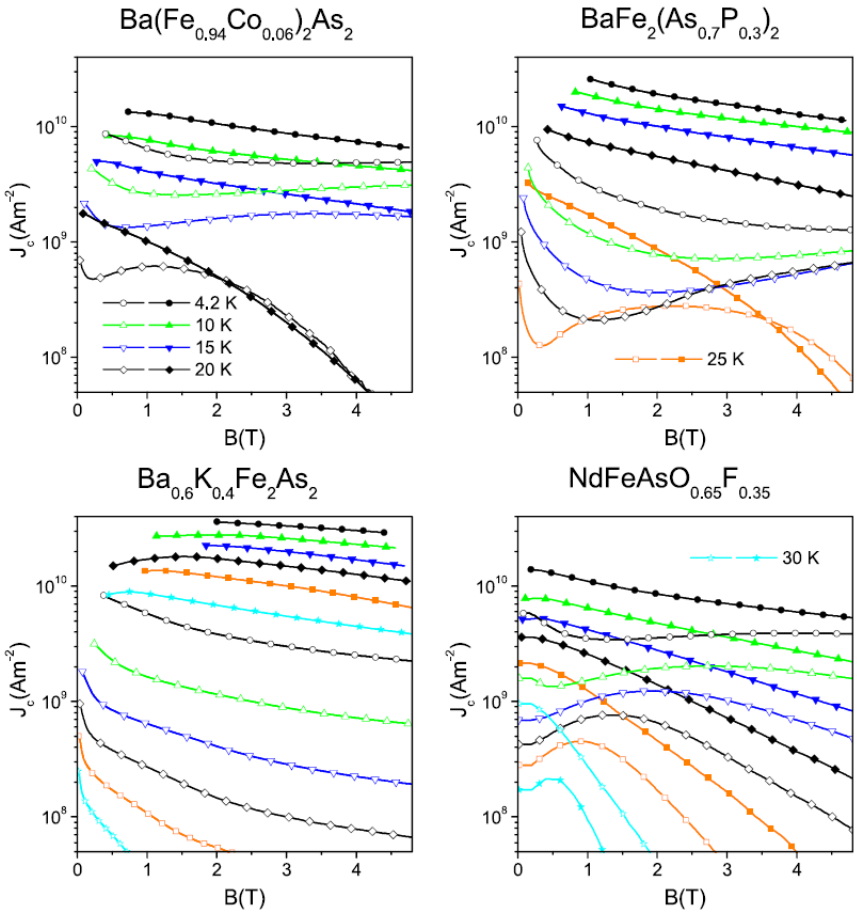

Fig. 4.2: Critical current density in $Ba(Fe_{0.94}Co_{0.06})_2As_2$, $BaFe_2(As_{0.7}P_{0.3})_2$, and $K_{0.4}Ba_{0.6}Fe_2As_2$ crystals. Open and solid symbols refer to the pristine and irradiated ($1.8 \times 10^{21}\ m^{-2}$) samples, respectively. The neutron fluence for the Nd-1111 crystal was $3.7 \times 10^{21}\ m^{-2}$. The same symbols always refer to the same temperature in all panels [57].

The field dependence of the critical current density is non-monotonic, and J_c is in addition non-monotonic in temperature at certain fields. The overall behaviour of J_c in iron-based single crystals seems to indicate that neutron irradiation tends to increase the critical current density, at least for low doses [57]. In contrast, irradiated iron-based superconducting films did not show the positive effect found in single crystals, showing a decrease in both T_c and J_c.

4.2 Fe(Se,Te) irradiation: state of the art

Very few studies have been carried out on the effect of irradiation on the superconducting properties of iron-selenium-tellurium thin films. In this work, Fe(Se,Te) films deposited on different samples (mainly single crystals and single crystals with chemical buffer layer) have been irradiated with both charged particles and neutrons.

4.2.1 Proton irradiation

G. Sylva *et. al.* [41] performed an experimental investigation, carried out with different proton fluences and energies, to understand proton irradiation effect in Fe(Se,Te) thin films. Five 100 nm thick thin films deposited on 001 CaF_2 single crystals have been irradiated, some directly with 3.5 MeV protons, while others with protons decelerated through the interposition of an 80 μm thick Al foil. This deceleration results in an average energy of protons impinging on the superconducting film of 1.43 ± 0.07 MeV. Different fluences have been used.

In all cases, protons crossed the films and are implanted into the substrate. The implantation depth in the CaF_2 substrates are 86 μm without Al foil and 21 μm with. Figure 4.3 shows the implantation profiles.

The average dpa in the films goes from 2.5×10^{-4} to 4.59×10^{-3}.

Figure 4.4 (a) reports J_c values as a function of the field for samples irradiated at different fluences, with the critical current density normalized to the value of pristine samples. The magnetic field was applied perpendicular to the ab plane, temperature fixed at 4.2 K. Samples irradiated directly with 3.5 MeV protons (A and B in figure 4.4) show an improvement of J_c with the increasing dose, while samples irradiated with the Al foil (C in figure 4.4) show an opposite trend. Therefore, J_C does not seem to have a monotonic and unique response to irradiation.

For a better evaluation, J_c was analysed as function of dpa, in order to take into account also the expected damage induced in the film. Figure 4.4 (b) shows J_c values, normalized to the value of the corresponding pristine samples, as a function of dpa at 4.2 K, 5 and 9 T. An increase of J_c is observed for samples irradiate without Al foil; on the contrary, the samples irradiated

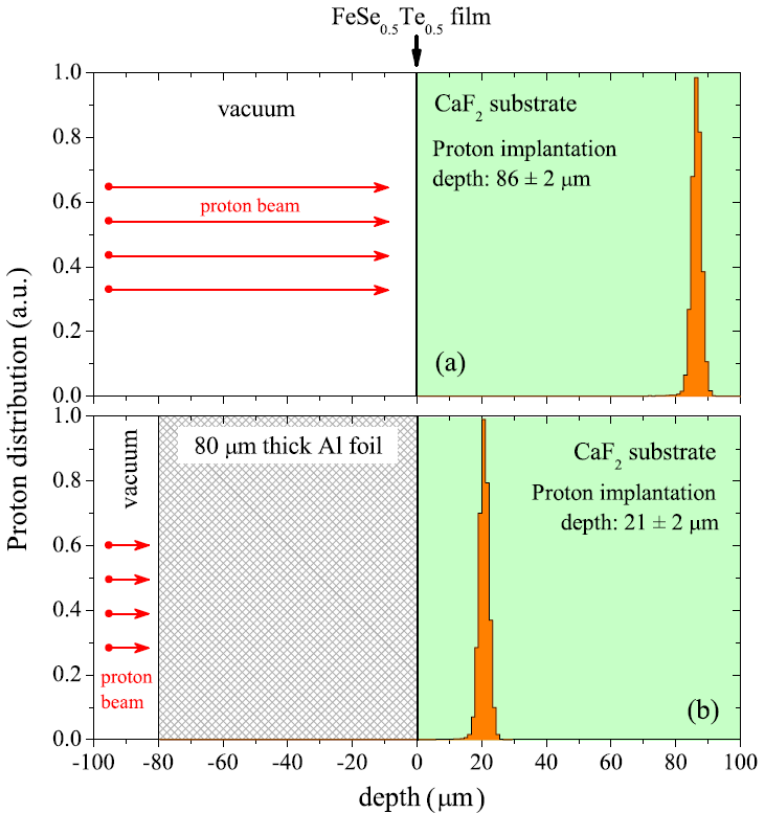

Fig. 4.3: Spatial distribution of the implanted protons (histograms) in the CaF_2 substrate (right regions) (a) without and (b) with the interposition of a 80 μm thick Al foil (crosshatch region) used to decelerate the protons. The zero depth corresponds to the sample surface. [41].

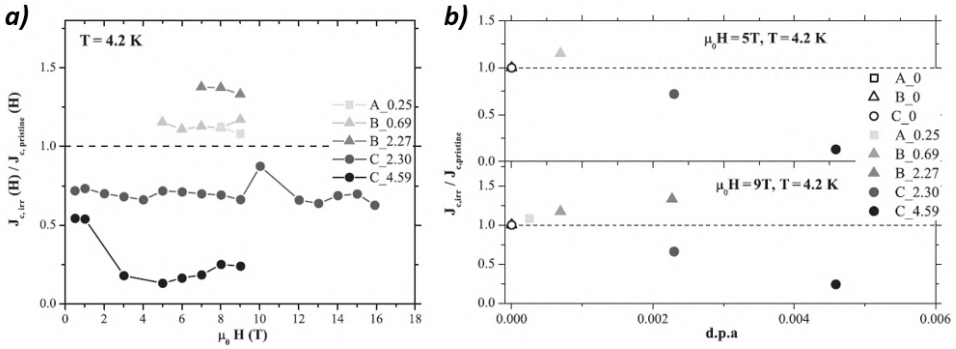

Fig. 4.4: (a) J_c versus magnetic field at 4.2 K for the different irradiated patterns normalised to the values of the relative pristine samples at the same fields. (b) J_c of the irradiated bars normalised to the values of the relative pristine samples at 4.2 K and 5 T (upper panel) and 9 T (lower panel).[41].

with the Al foil show a decrease in J_c for similar dpa. This difference in the irradiation effect could be ascribed to the influence of the different defect distribution in the substrate.

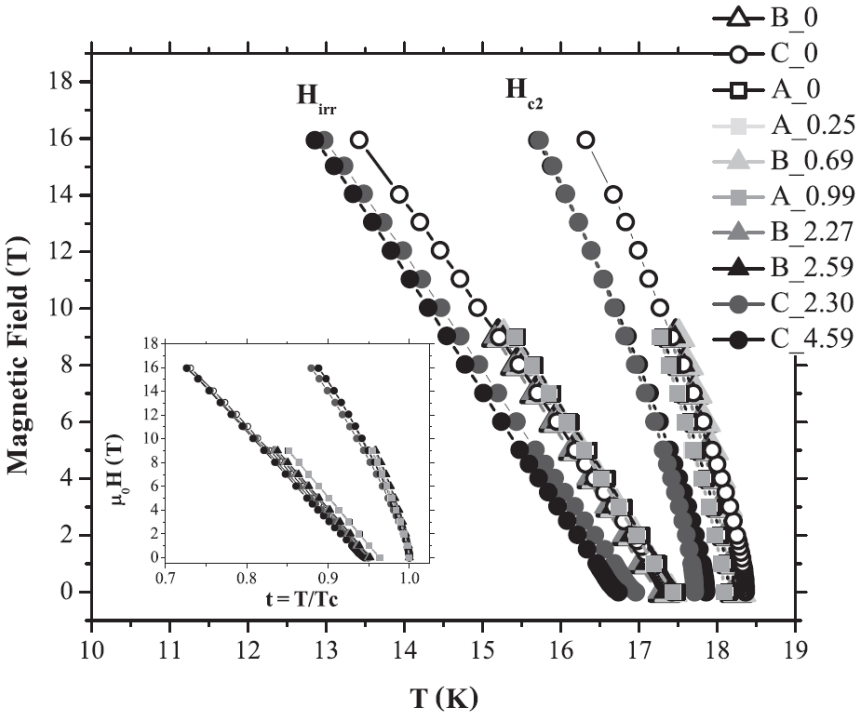

Fig. 4.5: Upper critical field and irreversibility field as a function of temperature for all samples. The inset shows the upper critical field and irreversibility field of all bars as a function of the reduced temperature of the corresponding pristine sample. [41].

From resistivity measurements, the irreversibility field H_{irr} and the upper critical field H_{C2}, both reported in figure 4.5, have been evaluated using the criterion of 10% and 90% of the resistivity value in the normal state above the transition. All the curves show very high slopes near T_c. Irradiation does not significantly change the slope of H_{irr} and H_{C2} curves: indeed, the curves belonging to the same sample are superimposed over each other for samples irradiated directly with 3.5 MeV protons (A and B), while the irradiated with Al foil (C) shows a slight decrease in T_c.

The effect due to 3.5 MeV protons slowed down by a 80 μm thick Al foil are confirmed by A Leo *et. al.* [65], where three samples have been considered, three Hall bars all realized from the same films. One Hall bar is used as reference (sample A in the following figures), while two others have been

irradiated with a fluence of 2.68×10^{16} (sample B) and 5.35×10^{16} (sample C).

The effect of the irradiation process is to increase the sample normal state resistivity as the proton fluence is increased. This effect can be associated to the sample crystal structure changes induced by the proton implantation in the substrate. The reduction of the critical temperature between the pristine sample and the most irradiated one is limited: a reduction of about 0.6 K is observed.

From the comparison of $H_{C2}^{\|ab}$ and $H_{C2}^{\|c}$ curves it is confirmed that the considered radiation process induces small changes in the properties of the material.

For all the samples, *V(I)* curves have been acquired, as a function of the applied magnetic field at three different temperature values (4.2, 8 and 12 K), for both the orientation H $\|$ c and H $\|$ ab [66]. In figure 4.6 the critical current curves evaluated from *V(I)* measurements are reported.

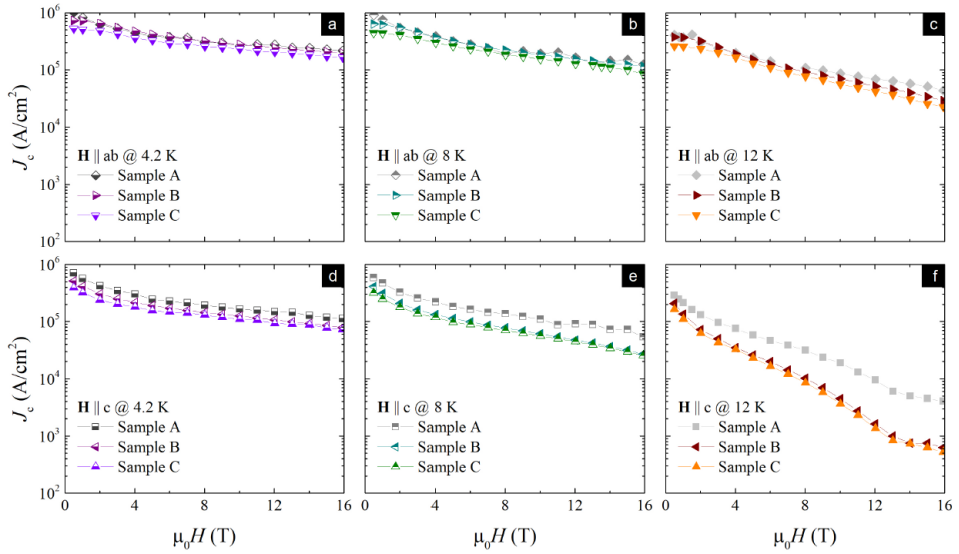

Fig. 4.6: In panels a, b and c the the critical current curve as a function of the applied magnetic field are reported for each of the three samples at 4.2, 8 and 12 K respectively. The field direction in this case is parallel to the superconducting film *ab-plane*. In panels d, e and f $J_c(\mu_0 H)$'s are reported for the field direction parallel to the superconducting film *c-axis* [66].

It is evident that the proton irradiation has an almost null effect on the critical current in the case H $\|$ ab, while for H $\|$ c a decrease in the J_c values

can be observed as temperature increases, and at high applied field.

As a consequence of the variation in the critical current values after the irradiation, also the anisotropy of the critical current results to be modified. Anyway, it is possible to observe that the irradiation process does not modify the general behaviour of the critical current as a function of the angle between the sample and the applied magnetic field.

The suppression in J_c for H $\parallel$ c can be associated with the variation of the strain in the superconducting films due to the position of the defects created in the substrate.

From the study led by G. Sylva *et. al.* [41], it looks like the substrate itself plays a role in determining irradiation effect on superconducting films. Therefore, irradiating Fe(Se,Te) films grown buffers with protons can lead to different results.

T. Ozaki *et al.* [67] irradiated CeO_2-buffered $SrTiO_3$ with 1.5 MeV protons: two films were irradiated with proton doses of 1×10^{15} p/cm^2 and 1×10^{16} p/cm^2. Based on simulations, those doses are estimated to be $\sim 3.2 \times 10^{-5}$ and $\sim 3.2 \times 10^{-4}$ dpa respectively.

The authors reported minimal impact of irradiation on T_c, both via magnetic and transport measurements. This could be to the low fluence, i.e., low dpa.

Figure 4.7(a) presents the magnetic field dependence of transport critical current density J_c with H $\parallel$ c for the film irradiated with a dose of 1×10^{15} p/cm^2. The positive effect of the proton irradiation on J_c at 4.2 K is unambiguous in the magnetic field below 1 T. As the magnetic field increased, the difference between pristine and the irradiated film became smaller. Similar behaviour was observed for the film irradiated with a dose of 1×10^{16} p/cm^2.

A more detailed representation of the pinning efficiency can be obtain from the angular dependence of J_c. Figure 4.7(b) shows $J_c(\theta)$ for the film irradiated with 1×10^{15} p/cm^2 dose, under 1 and 3 T at 4.2 K. The pristine film has a less anisotropic J_c angular dependence: a small J_c-anisotropy, γ_{Jc}, of 1.7 is been observed at 1 T. Upon irradiation, the J_c increase for most of the field orientation, retaining a small γ_{Jc} of 1.7 at 1 T. The J_c suppression at around H $\parallel$ ab would occur because of the reduction in the density of intrinsic pining upon the irradiation.

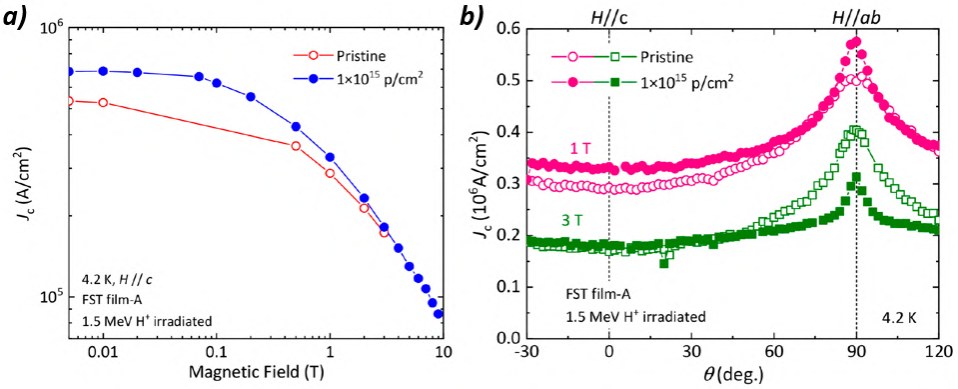

Fig. 4.7: (a) Magnetic field dependence of critical current density J_c obtained from transport measurement at 4.2 K for a FST film pre- and post-1.5 MeV proton irradiation with 1×10^{15} p/cm^2 dose. (b) Angular field dependence of the critical current density J_c obtained from transport measurement for a FST film before and after proton irradiation measured at 4.2 K under 1 and 3 T [67].

Enhancement of the critical temperature for a Fe(Se,Te) film after low energy proton irradiation

T. Ozaki et al. [63] reported a unique result on low-energy proton irradiation effects on a Fe(Se,Te) film deposited on CeO_2-buffered $SrTiO_3$ single crystal: they found out that irradiated film (1×10^{15} pcm^{-2} dose of 190 keV protons) does not show any T_c degradation, in respect to the pristine, rather an increase of T_c by ~ 0.5 K.

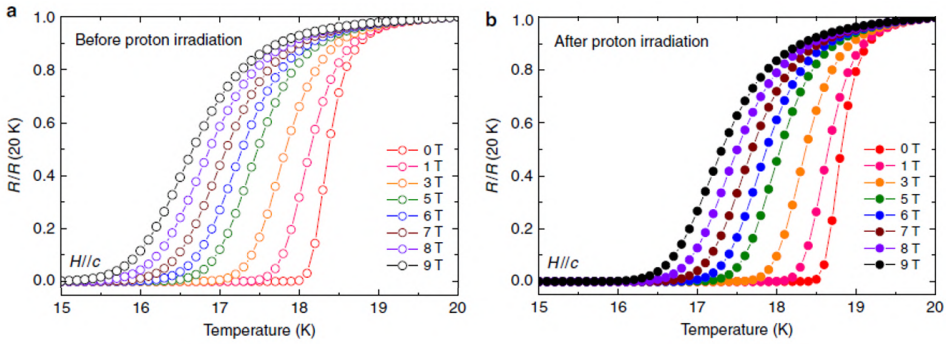

Fig. 4.8: Temperature dependence of normalized resistivity. $\rho(T)/\rho(20K)$ at 0–9 T $\parallel$ c for the Fe(Se,TE) film before (a) and after (b) 190 keV proton irradiation with 1×10^{15} pcm^{-2} dose [63].

Possible explanations can be grouped into three categories:

1. An interface effect;

2. An elimination of the influence of excess Fe at the interstitial sites of the Se/Te layer;

3. A strain effect.

The first point is based on the observation of monolayer FeSe films on STO substrates, but the effect is not relevant for the considered sample: a $\sim$ 100 nm thick film.

The second point is based on post annealing effect; what is more remarkable here is that excess Fe is not present in the sample.

The last point is related to the strain effect on T_c, as pointed out in section 2.4. From TEM analysis performed on the irradiated film they observed splayed cascade defects produced by proton irradiation over the entire film. Given that nuclear scattering events produce angular deviations from the original incident angle as the incident ions proceed through a target material, it is not surprising that light mass proton with a low energy of 190 keV easily tilted away from the original incident angle (0°) and create the disordered cascade defects.

According to Anderson's theorem [68], the T_c and the superconducting density of states are not affected by the non-magnetic impurities created by proton irradiation, whereas non-magnetic impurities can act as strong scattering centers and suppress T_c by pair breaking in s_{+-} superconductors. Given the opposite behaviour in this sample, the authors propose a different mechanism to explain the enhancement of T_c. Besides the clearly visible cascade, there is also a curvature of the lattice fringe inwardly directed, which produces strain field around the cascade defect. Although the size of the cascade defects is about 1 $\sim$ 2 nm in diameter and $\sim$ 10 nm wide, the strain fields are expected to extend far out to the cascade defect, especially in the radial direction and, as a result, can cause the local lattice distortion.

In figure 4.9 the upper critical field $H_{C2}(T)$ and irreversible field $H_{irr}(T)$ for H $\parallel$ c are plotted, before and after proton irradiation. Both H_{C2} and H_{irr} shift to higher T for the proton-irradiated film. When plotted as a function of $t = T/T_c$, H_{C2} and H_{irr} it can be seen that the increase for H_{irr} is even more significant.

A transport study of the angular dependence of J_c due to 190 keV proton

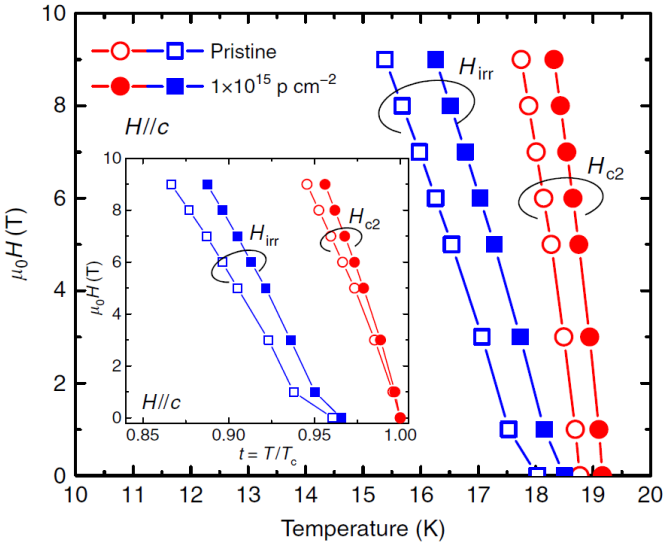

Fig. 4.9: Upper critical field and irreversibility field. Upper critical field $H_{C2}(T)$ and irreversible field $H_{irr}(T)$ (H $\parallel$ c) as a function of temperature up to 9 T $\parallel$ c for Fe(Se,Te) films before and after proton irradiation determined from figure 4.8. Inset: normalized temperature ($t = T/T_c$) dependence of H_{C2} and H_{irr} for the same field orientation [**?**].

irradiation [69] has also been performed. This gives important insight into the pinning effectiveness of the superconducting films.

Small J_c anisotropies γ_{Jc} ($J_c^{H\|ab}/J_c^{H\|c}$) were observed: it's been found out that the anisotropy increases with increasing magnetic field.

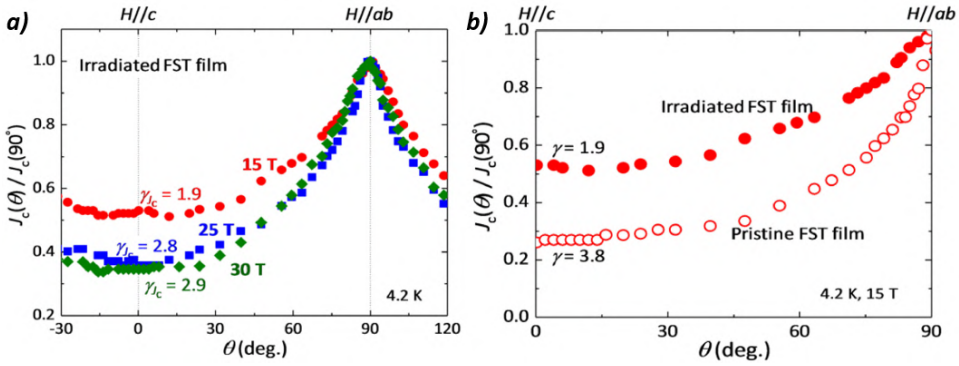

Fig. 4.10: (a) Angular field dependence of the normalized critical current density $J_c(\theta)/J_c(90^\circ)$ at 4.2 K for the 190 keV proton-irradiated $Fe(Se,Te)$ films at 15, 25, and 30 T. (b) Angular field dependence of the normalized critical current density $J_c(\theta)/J_c(90^\circ)$ for the pristine and the proton-irradiated $Fe(Se,Te)$ films at a dose of 1×10^{15} pcm^{-2} at 4.2 K and 15 T [69].

In order to compare the γ_{Jc} in the irradiated film with the one in the

pristine under high magnetic field, the normalized critical current density $J_c(\theta)/J_c(90°)$ is shown in figure 4.10. A reduction in anisotropy (by about a factor of two) is achieved after irradiation with low-energy protons.

The cascade defects observed thanks to TEM analysis and the extension of strain field that provides pinning potential to vortex are found to be much stronger in the *ab*-plane, that inhibits the in-plane motion of vortices and thus leads to strong enhancement of J_c for magnetic field applied along the *c-axis*.

It appears that not only the particle type and energy affect the properties of the films, but the substrate also plays a crucial role in the change in superconducting properties due to irradiation: besides defects created in the film, impinging protons produce modifications of the substrate that in turn have influence on the properties of the film.

4.2.2 Heavy ion irradiation

Irradiation with heavy ions (i.e. Pb or Au ions) creates correlated defects along the ion's trajectory, and a cloud of point-like defects due to secondary electrons generated in ion-atom collisions. Correlated or columnar defects play a fundamental role in pinning of vortex, and thus enhance both the critical current and the irreversibility field, while point-like defects are the main responsible for the increase in resistivity.

D. Torsello *et. al.* [70] tried to gain a comprehensive picture of the effects of different kinds of ion irradiation by using a variety of particles and energies on iron based superconductors single crystals ([71], [70]). They used microwave characterization to investigate the irradiation-induced critical temperature degradation and the increase of normal state resistivity and penetration depth.

In all cases, they found that the behaviour is qualitatively similar (linear decrease) in all iBS, but quantitatively very different for ions and energies that create different types of defects.

Comparing the slopes of the linear relations of the T_c degradation for the different cases can be useful to investigate the intrinsic radiation hardness of a specific material. The authors investigated the response of differently doped iron based material to the same irradiation condition.

Generally, it can be noticed that the higher the energy is, the faster is the degradation of the critical temperature with damage (therefore with the dpa). This could be due to a different efficiency in defect production at different energies or to the fact that dpa alone does not completely account for all the structural consequences of ion irradiation. In fact, for high-energy heavy ions an important mechanism which is not accounted for by dpa is the deposition of energy via ionization, causing deformation, or melting, of the lattice along the ion track, when a given threshold of the electronic stopping power is overcome. This very well known mechanism is responsible for the production of linearly correlated defects and continuous columnar tracks in a variety of materials, including iron based superconductors.

Defects are efficient scattering centers. These defects are typically nano-sized cascades that are generally quite homogeneously distributed throughout the sample, also far from columnar tracks, when present. This is due to the fact that a primary knock-on atom generated along the track will have enough energy to further travel in the material. Therefore, one can assume that generally the whole material outside the columnar defects is modified by irradiation. A different behaviour is shown bu proton irradiated samples.

All these consideretion were valid when irradiating single crystals. However, in the case of thin films, the situation is considerably complicated by the role played by the substrate. As a matter of fact, T_c decreases very little upon irradiation, while the residual resistivity ρ_0 increases considerably [73].

Visualizing the atomic-scale effect of irradiating $FeSe_xTe_{1-x}$ with 249 MeV Au ions revealed two distinct effects: compact nanometer-sized regions of crystal disruption or "columnar defects", plus a higher density of single atomic site "point" defects probably from secondary scattering.

Figure 4.11 compares ^{3}He-refrigerator-based spectroscopic imaging scanning tunneling microscope (SI-STM) results for single crystals of $FeSe_{0.45}Te_{0.55}$ both pristine (a) and irradiated with 249 MeV Au ions (b). This technique consists of making atomically resolved and registered images of the surface topography T($\mathbf{r}$). Figure 4.11(a) shows typical T($\mathbf{r}$) of the TeSe termination layer with individual Te/Se atomic sites clearly visible. A twin sample was irradiated with 249 MeV Au ions using a fluence of 1.93×10^{15} m^{-2} so that the "dose equivalent field" is B_ϕ=4 T (this is the field corresponding to a fluxon per incident ion). However, few-hundreds MeV heavy ions in

metallic iron based superconductors create defect track that are expected to be discontinuous; thus, the actual columnar defect density in a given crystal layer may be lower than the fluence.

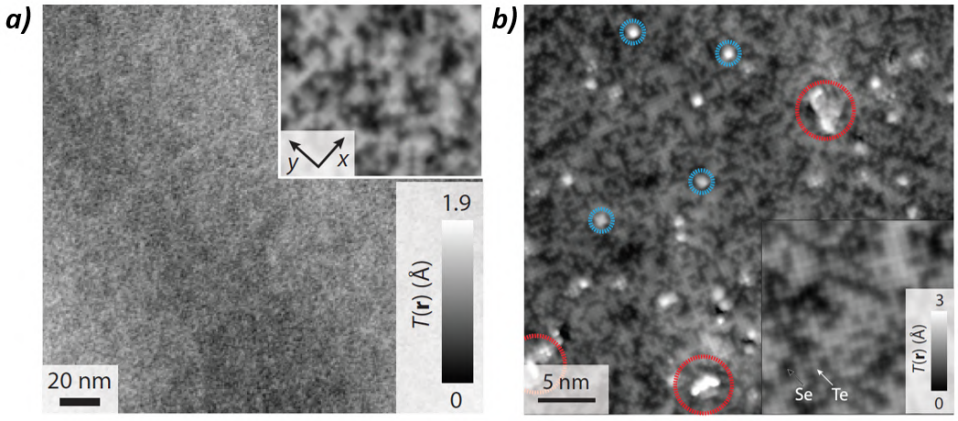

Fig. 4.11: (*a*) Large, atomically resolved constant current topography T(**r**) of $FeSe_{0.45}Te_{0.55}$. The inset shows an enlargement of the atomic lattice using the same color scale. (*b*) High-resolution T(**r**) of heavy ion–irradiated $FeSe_{0.45}Te_{0.55}$. As for the pristine sample, the predominant feature is the binary Se/Te surface appearance (inset). Red and blue circles indicate the columnar and point defects that are both only observed after irradiation [74].

Figure 4.11(*b*) shows high resolution T(**r**) typical of the irradiated $FeSe_xTe_{1-x}$ crystals, in which two striking new features are apparent. The first consists of large (radius ∼1.5 nm) amorphous regions (for example, red circles in figure 4.11(*b*)) with surface coverage equivalent to a matching magnetic field of about 2 T in this field of view (FOV). The second type of feature occurs in larger numbers and consists of an atomic-scale point defect (for example, blue circles) centered in between Se/Te sites, thus, at the Fe site in the layer below the surface. An hypothesis is that the heavy ion irradiation has displaced Fe atoms into these sites. Atomic-scale imaging reveals that columnar defects exhibit an amorphous crystal structure in a region with a diameter of about 3 nm.

T. Ozaki *et. al.* irradiated Fe(Se,Te) film with 6 MeV Au ions with 1×10^{12} $Au\ cm^{-2}$ [75]. Thi low dosage is tree order of magnitude lower than that for proton irradiation discussed in section 4.2.1. Considered samples are 100-130 nm thick Fe(Se,Te) films with a CeO_2 buffer layer on $SrTiO_3$ single crystal substrates; the samples were irradiated at fluence $\phi = 1 \times 10^{12}$ $ion\ cm^{-2}$ with 6 MeV Au^{3+} ions in vacuum at room temperature; the beam was

directed to the film surface at normal incidence.

Figure 4.12 shows the SRIM simulations results of 6 MeV Au ion irradiation into a Fe(Se,Te) film, with a fluence of 1×10^{12} Au cm^{-2}. Figures (a)-(c) present the target depth dependence of Au ion trajectories, a histogram of the ranges of the Au ion and he number of target vacancies from damaged events of Au ion irradiation, respectively. From those simulation it appears that Au ion irradiation would create high and uniform damage in the film [76].

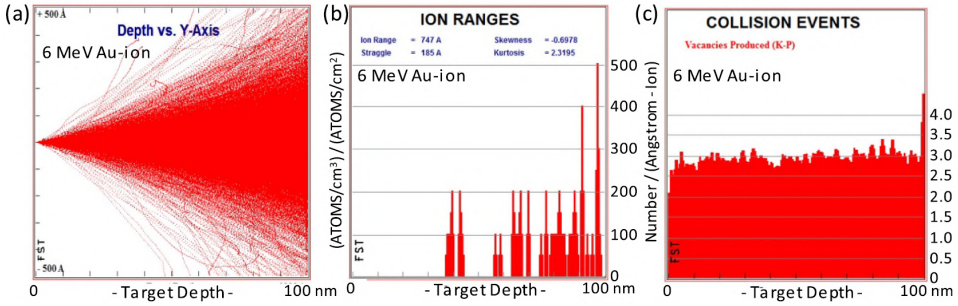

Fig. 4.12: SRIM simulation results of the Au-ion irradiation with 6 MeV into an FST film. (a) Plot of Au-ion trajectories, (b) ion range of Au ions and (c) the damage (vacancy) profile produced by Au ions as a function of target depth [76].

Figure 4.13(a) shows the temperature dependence of the electrical resistivity before and after irradiation. It appears that Au irradiation slightly suppresses T_c by about 0.5 K (from 17.9 to 17.4 K). The simulation using the stopping range of ions in matter software package predicts that the 6 MeV Au ions to a dose of 1×10^{12} Au cm^{-2} could produce 6.42×10^{-3} dpa. The behaviour of the normal state resistivity indicates that this irradiation produces non-magnetic defects.

Figure 4.13(b) presents the magnetic field dependence of the transport critical current density J_c with H $\parallel$ c for the sample before and after irradiation at 4.2 and 10 K. The self-field J_c values are almost the same before and after irradiation at both 4.2 and 10 K. However, as the magnetic field increases, the enhancing effect of the irradiation is clearly visible. Figure 4.13(b) also shows the J_c enhancement $\frac{J_c^{after} - J_c^{before}}{J_c^{before}}$, for the irradiated sample relative to the pristine, for 4.2 and 10 K. At 4.2 K, the J_c enhancement shows gradual increase with increasing magnetic field. At 10 K, the Au ion irradiation yields up to 70% J_c enhancement at 9 T.

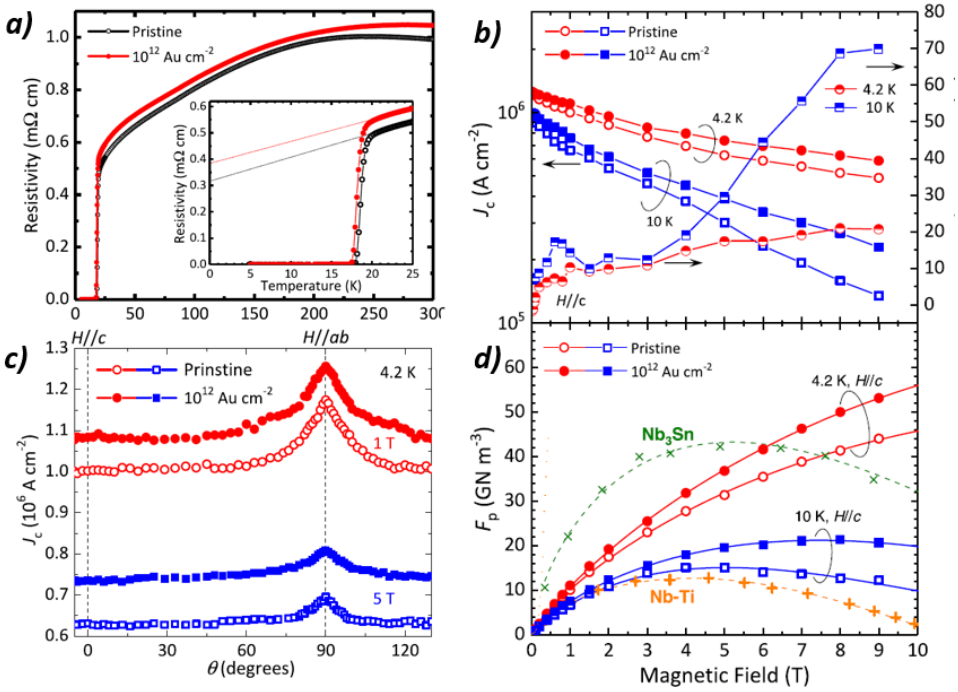

Fig. 4.13: (a) Temperature dependences of electrical resistivity for the Fe(Se,Te) film before and after 6 MeV Au-ion irradiation. Inset presents magnified temperature region near T_c. (b) Magnetic field dependence of J_c at 4.2 and 10 K of the Fe(Se,Te) film in the pristine state and following irradiation with 6 MeV Au-ion in H//c direction. Magnetic field dependence of J_c enhancement for the film at 4.2 and 10 K is shown on the right y-axis. (d) Corresponding magnetic field dependence of vortex pinning force F_P for the films, compared with the data of $NbTi$ and Nb_3Sn wires. (c) Angular field dependence of the critical current density at 4.2 K for the films before and after Au-ion irradiation at 1 and 5 T [75].

Figure 4.13(c) shows $J_c(\theta)$ before and after irradiation under 1 and 5 T at 4.2 K. The pristine film has an isotropic J_c angular dependence up to 5 T. J_c exhibits a broad maximum H $\parallel$ ab and no prominent J_c peak at H $\parallel$ c. Very small J_c-anisotropies $\gamma_{Jc}(J_c^{H\|ab}/J_c^{H\|c})$ of 1.17 and 1.10 are observed at 1 and 5 T, respectively. Upon irradiation, the J_c increases for all orientations, retaining small γ_{Jc} of 1.15 and 1.10 at 1 and 5 T, respectively, indicating that the pinning centers are isotropic and randomly distributed.

Atomic scale analysis with HRTEM revealed the presence of cluster-like defects modified by the Au irradiation over the entire film, clusters with typical size around 10-15 nm.

Thanks to X-ray analysis, it's been possible to determine that the shape of the most defects is anisotropic, with the size along (100) direction larger than

that along (001) direction. The modified structure has a similar lattice to the pristine. However, larger lattice parameters, a ∼0.45 mn and c ∼0.69 nm, are obtained from diffractograms. These defects are different from columnar defects with a diameter of about 3 nm and cluster of point-like defects in $FeSe_{0.45}Te_{0.55}$ single crystals irradiated with 249 MeV Au ions previously described [75].

The SRIM code predicts that the 6 MeV Au-ion irradiation at a dose of 1×10^{12} Au cm^{-2} corresponds to $\sim 6.4 \times 10^{-3}$ dpa. In the case of YBCO thin films, significant degradation begins to occur at 200 keV He-ions dose of 3×10^{14} He cm^{-2}, corresponding to $\sim 2 \times 10^{-3}$ dpa. Fe(Se,Te) appears to be more resistant to irradiation than YBCO.

4.2.3 Neutron irradiation

Of all the different types of irradiation, the one that comes closest to simulating the effect on a superconductor in a fusion environment is undoubtedly neutron irradiation, and in particular fast neutron irradiation. However, obtaining fast neutrons in sufficient doses to simulate the effects of plasma irradiation is not trivial.

M. Eisterer *et. al.* [77] irradiated with neutrons four Fe(Se,Te) films grown on lanthanum aluminate substrates, thickness ranging from 150 to 200 nm. The experiment was performed in the central irradiation facility of the TRIGA-Mark-II reactor in Vienna. Two samples (designated A and B), sealed in a quartz tube filled with ∼150 mbar helium, were exposed to the neutron flux for 7 h and 19 min, corresponding to a nominal fast neutron fluence of 2×10^{21} m^{-2}. This irradiation is expected to produce various defects ranging from single displaced atoms to defects of several nanometres, statistically distributed and uncorrelated. Two samples (labelled C and D) were also measured for comparison).

The temperature dependence of the upper critical field, $B_{C2}(T)$, of samples B and C, and the irreversibility lines, $B_{irr}(T)$, of all samples, are plotted in the upper and lower panel of figure 4.14(a). The irreversibility lines of the irradiated sample A^{irrad} and the pristine sample D are virtually identical in parallel orientation. The irreversibility line of the irradiated B^{irrad} is slightly steeper than $B_{irr}(T)$ of sample D in the perpendicular configuration,

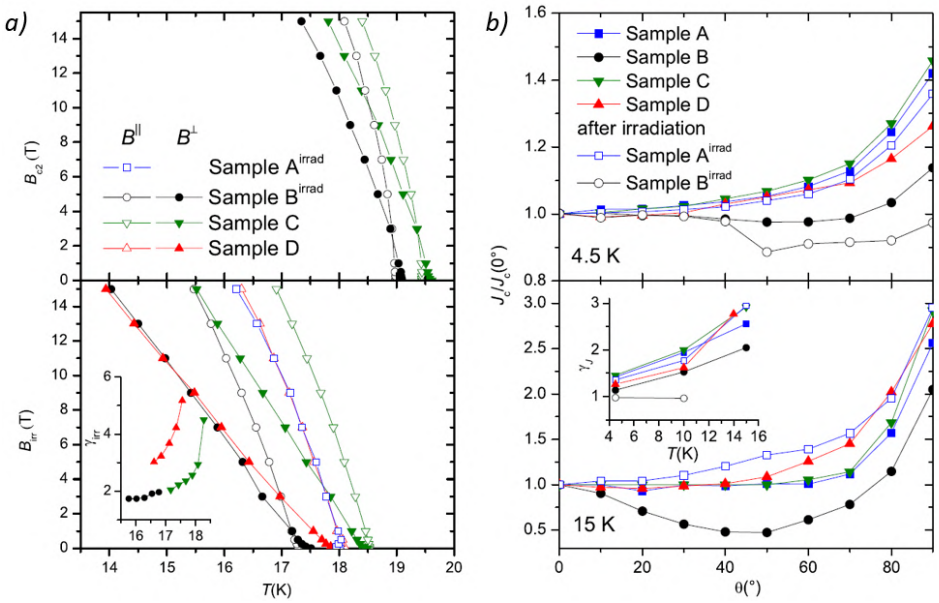

Fig. 4.14: (*a*) Upper critical field (upper panel) and irreversibility (lower panel) lines for both main field orientations. Samples C and D were measured before, and samples A^{irrad} and B^{irrad} after irradiation. The insert shows the anisotropy of the irreversibility field near T_c. (*b*) Angular dependence of the critical currents at 1 T. Data in the upper and lower panels refer to 4.5 K and 15 K, respectively. The J_c anisotropy increases with temperature, as can be seen best in the inset. [77].

but $B_{irr}(T)$ of C is steepest in this orientation. It can be concluded that sample-to-sample variations are larger than the effect of the neutron induced defects.

All the samples, before irradiation, have the same field dependence of the critical current density, but J_c in the best sample is about 85% higher than in the worst. The temperature dependence, on the other hand, is not the same in all samples. The differences must be, at least partly, caused by differences in the pinning landscape. The influence of neutron irradiation is rather small at low temperature (4.5 K), and becomes larger ah higher temperatures. Although the positive effect of the irradiation is unambiguous, since the same sample was measured before and after irradiation, the changes remain within the sample-to-sample variations. In contrast to what happens in other iron based superconductors, pinning is strong in pristine 11 thin films, and therefore not significantly enhanced by the irradiation. Indeed, at highest temperature (15 K), a significant increase of J_c is obtained upon irradiation.

The sensitivity of the critical currents on the orientation of the magnetic field can be better seen by plotting the angular dependence of the critical current density at fixed magnetic field. $J_c(\theta)$ at 1 T (normalized by $J_c(0°)$) in all samples is plotted in figure 4.14(b). The data in the upper panel refer to 4.5 K, while in the lower panel to 15 K. The critical currents monotonically increase with angle and no indication of c-axis correlated defects is observed. The J_c-anisotropy increases with temperature by around one third from 4.5 to 10 K, and is approximately doubled at 15 K (as shown in the inset of figure 4.14(b)).

The effect of disorder, introduced by neutron irradiation, on the upper critical field, the irreversibility field and the critical currents is small and comparable to typical sample-to-sample variations.

Chapter 5

Effect of irradiation on Fe(Se,Te) superconducting films

The second main objective of my work was to try to understand the usability of the Fe(Se,Te) phase for the fabrication of magnets for plasma confinement in fusion power plants. For this purpose, in collaboration with the Politecnico di Torino, I personally participated in several irradiation runs, both with protons and neutrons. In addition, some samples were irradiated with gold ions by the Politecnico di Torino. The irradiated samples were prepared by myself using both single-crystal substrates and buffered samples, with the aim of understanding whether samples deposited on metal foil with a buffer layer can survive in a radiation environment. I also characterized the samples mentioned above, irradiated selectively, also taking advantage of specific patterns, both from a structural point of view, with diffraction analyses, also using machine time at the Bessy II synchrotron in Berlin, and with magnetic and transport characterisations, both before and after irradiation. Some samples deposited on single crystals were characterised by colleagues at the CNR-SPIN institute in Salerno, while some buffered samples were characterised by colleagues at ENEA. Magneto-optical analyses were carried out by colleagues from the Politecnico di Torino, who were also working on simulations of the effects of radiation on films.

5.1 Proton irradiation on Fe(Se,Te) films

5.1.1 Proton irradiation on Fe(Se,Te) films on CaF and CZO-buffered YSZ

Proton irradiation is the simplest to achieve due to the compactness of the accelerator, lower radioactivity and lower cost of operation.

We confronted proton irradiation effects on Fe(Se;Te) deposited both on CaF_2 single crystals (section 3.2) and on CZO-buffered YSZ (section 3.3). All the samples were patterned as described in section 3.2, with either $20\mu m \times 50\mu m$ Hall-bars and rectangular shapes have been designed. The irradiations, with proton energies ranging from 0.5 to 3.5 MeV, were performed in high vacuum and at room temperature at the CN and AN2000 facilities of the INFN Laboratori Nazionali di Legnaro.

Simulations of the damage induced both in the film and in the substrate have been performed at Politecnico di Torino, using the SRIM code [78]. Stopping and Range of Ions in Matter (SRIM) is a well established algorithm, based on a random material assumption and a Monte Carlo approach using the binary collision approximation. The SRIM code is used to simulate material damages and ion implantations for the given irradiaton condition. It also has the capability to compute dpa (number of displacements per atoms). The SRIM calculation, however, does not include thermal annealing effects that happen after creating irradiaton damages, and hence tends to overstimate the number of defects.

Figure 5.1 summarises the proton irradiation performed on different samples, and using different proton energies: it shows the implantation depth of the protons, of different energies, in different samples.

In all cases the protons crossed the films and implanted into the substrate with implantation depth varying from 4.5 to 86 μm, depending on both the type of substrate and the proton energy. [79]

In the superconductor protons produce randomly distributed point defects, and small cascades forming clusters of defects with typical dimension of the order of few nm. Using the same code, the damage in the film in terms of dpa has been estimated following the modified Kinchin Pease approach [81]. The simulations showed that damage is very homogeneous across the 100

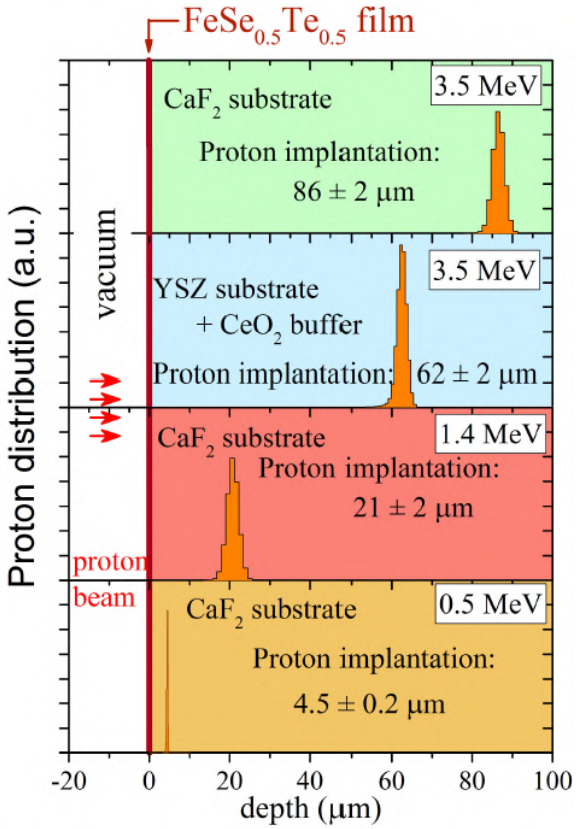

Fig. 5.1: Summary of the four proton irradiation conditions showing the implantation peak in the substrate of the Fe(Se,Te) thin films [79].

nm thick films.

To evaluate the irradiation damage induced in the samples, different measurements were performed. For structural studies X-ray analysis were performed, while to investigate a change in the superconducting properties transport characterisations were performed at CNR-SPIN institutes of Genova and Salerno. Magneto-optical analysis were carried out at Politecnico di Torino.

X-Ray Analysis

Unpatterned samples were investigated by X-ray diffraction to study the strain induced by the substrate after irradiation. The values of the c cell parameter were evaluated from the $(00l)$ diffraction patterns, and the CaF_2 substrate was used as a reference to refine the instrumental resolution func-

tion and the zero-shift parameter. A Thompson-Cox-Hastings pseudo-Voigt function convoluted with an axial divergence asymmetry function was used to model diffraction lines. The obtained values were fixed, and the parameters pertaining to the Fe(Se,Te) thin films (the lattice parameter c and the Lorentzian strain parameter) were refined by imposing a full c-axis texturing. Lattice microstrain along [00l] was evaluated by the refined strain parameters, and the broadening of the diffraction lines was analysed by means of the Williamson-Hall plot method [82].

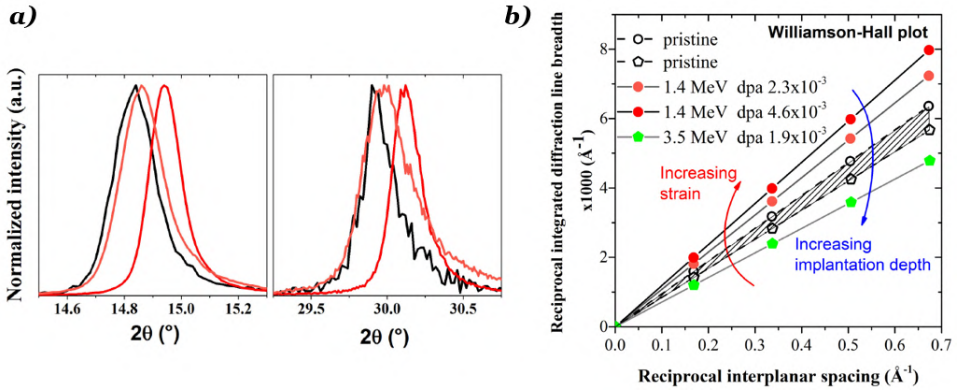

Fig. 5.2: Williamson-Hall plots (b) obtained by X-ray diffraction patterns of Fe(Se,Te) samples on CaF_2 before and after irradiation with 1.4 and 3.5 MeV protons. By way of example, modifications of the diffraction peaks after two irradiations doses with 1.4 MeV protons are shown in (b) for the (001) and (002) reflections (left and right panels, respectively) [79].

The X-ray analysis of the strain induced in the film is reported in figure 5.2(b) . It shows that the irradiation process can increase (shallow implantation) or decrease (deep implantation) the strain in the film, resulting in a worse or better response to the irradiation process of the superconducting material, respectively. It is also notable that the strain is not constant along the thickness of the film due to relaxation. However, since all films have the same thickness, this should not affect the discussion.

Transport Measurements

The electrical transport properties of the micro-bridges were measured in a Physical Properties Measuring System (PPMS) by Quantum Design up to 9 T (CNR-SPIN Genova), and in a Cryogenic Free Measurement System (CFMS) by Cryogenic Ltd up to 16 T (CNR-SPIN Salerno). Resistivity

measurements were performed by the standard four-probe current-biased measurement technique, and critical temperature was defined by the 90% criterion of the normal state resistivity. Critical current values at different temperatures and magnetic field were extracted from voltage versus current characteristics. The same sample has been always measured in the pristine and irradiated state by keeping some of the Hall-bars pristine and exposing the others for different times to the ion beam, to obtain different doses. Let's remember that this procedure is important to avoid sample-to-sample variability issues.

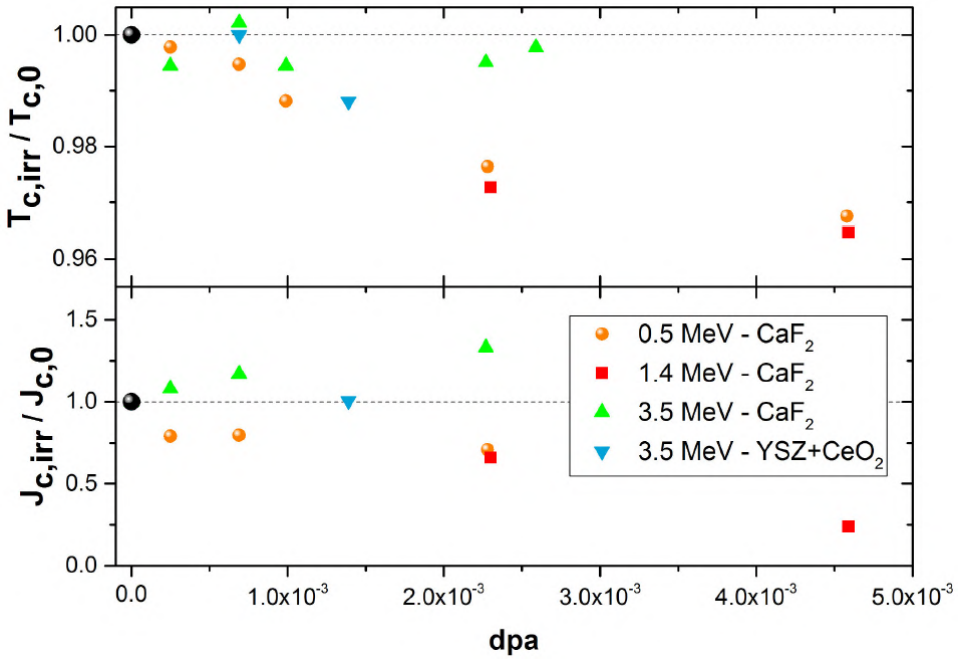

Fig. 5.3: Critical temperature (defined with the 90% criterion) and critical current modifications (at an applied magnetic field of 8 T) due to irradiation as a function of dpa for different energy and substrate combinations resulting in different implantation depths [79].

The modifications of the critical temperature as well as those of the critical current density, are plotted in figure 5.3 as a function of dpa for all the energy-substrate combinations. The four datasets show different behaviour, but it appears that the samples perform better when protons are implanted far from the interface with the film, as shown in figure 5.1.

In particular, for samples deposited on CaF, we observed an increase in the critical current density J_c for the higher proton energy (3.5 MeV), there-

fore when protons implant themselves far from the interface with the film. Anyway, all the fluences and doses studied provoked a negligible decrease in T_c and a very low change in J_c. Apparently, the sample deposited on Zr-CeO_2-buffered YSZ shows no modification of the critical current despite some worsening of the critical temperature (still very limited, $\Delta T_c \sim 0.3$ K for dpa $= 1.38 \times 10^{-3}$).

Magneto-Optical Analysis

Samples deposited on Zr-CeO_2-buffered YSZ single crystals were also characterized at Politecnico di Torino by magneto-optical imaging with an indicator film technique (MOI), that makes use of the Faraday effect to directly visualize the magnetic field distribution [83]. A nonlinear calibration combined with an iterative algorithm allows obtaining the quantitative measurements of the magnetic field and the reconstruction of the magnetic field distribution. In this case, the rectangular patterns were partially irradiated and partially protected with a suitable screen to keep them pristine. The analysis of such samples ensured that a direct comparison could be carried out without differences in terms of thermal contact or distance to the indicator film, and that the observed modifications can be attributed to the introduction of defects by irradiation.

Figure 5.4(a) shows the optical image of the sample and the low temperature magnetic pattern both with an applied magnetic field of 20 mT, and in the remanent state. The irradiated half of the crystal is marked in the figure with a yellow square, however, is also clearly visible from the different optical contrast in the optical image. No distortion of magnetic pattern is observed, whereas a modification would be expected if the critical current had been changed by the irradiation. This observation, directly visible from the MOI image, is quantitatively presented in figure 5.4(c) through the magnetic field profiles in the pristine (blue symbols) and irradiated (magenta symbols) central regions of the remanent state: the profiles overlap with each other and with the theoretical curve predicted by the Bean model. Therefore MOI confirms what was observed by the transport measurements and suggests that the use of a buffer layer might contribute to relax the strain induced by irradiation damage.

We can conclude that proton irradiation affects the superconductor mainly

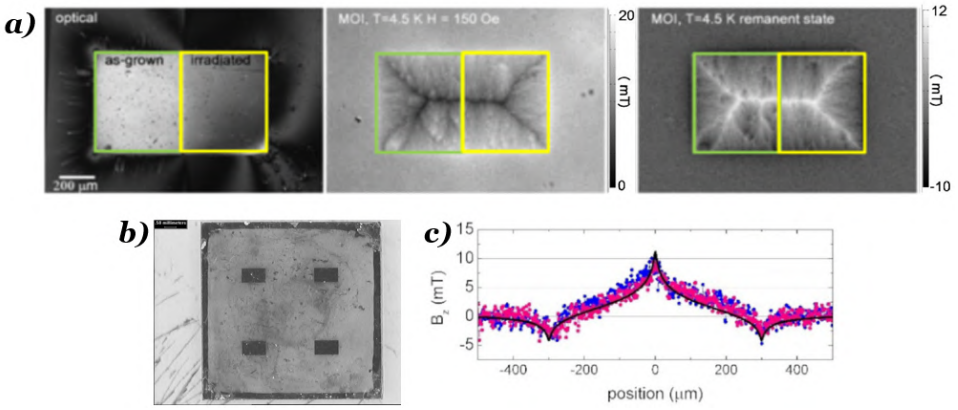

Fig. 5.4: Optical image of the sample (left panel (a)), the irradiated part (with 3.5MeV protons at dpa=1.38×10^3) is identified by the yellow square, in contrast to thwe green one identifying the as prepared part, and MOI quantitative measurements of the magnetic pattern in applied magnetic field and in the remanent state (after a maximum applied field of $\mu_0 H = 20$ mT) at T = 4.5 K (central panel (a)). The magnetic field profiles in the central region of the remanent state, taken across the irradiated (magenta symbols) and the as-grown (blue symbols) parts of the sample are shown in panel (c), together with the expected curve from the Bean model (black line) [79]. Panel (b) shows a picture of the patterned sample.

by introducing strain due to proton implantation in the substrate. This effect is crucial for samples deposited directly on a single crystal, but the presence of the buffer layer helps to absorb the strain and therefore increases the radiation hardness of the material.

A very important consideration is the comparison of the effects that proton irradiation has on Fe(Se,Te) with the effects on YBCO. Figure 5.5 shows magneto-optical analysis before and after irradiation for a YBCO film, irradiated with 3.5 MeV protons with a dpa = $1.42 - 2.8410^{-4}$ [80].

Comparing this figure with the figure 5.4(a), it can be concluded that the YBCO, although irradiated with 5 times less dpa than the irradiation of Fe(Se,Te), undergoes a J_c degradation of more than 80%. It can therefore be said that Fe(Se,Te) is much more resistant to proton radiation than YBCO.

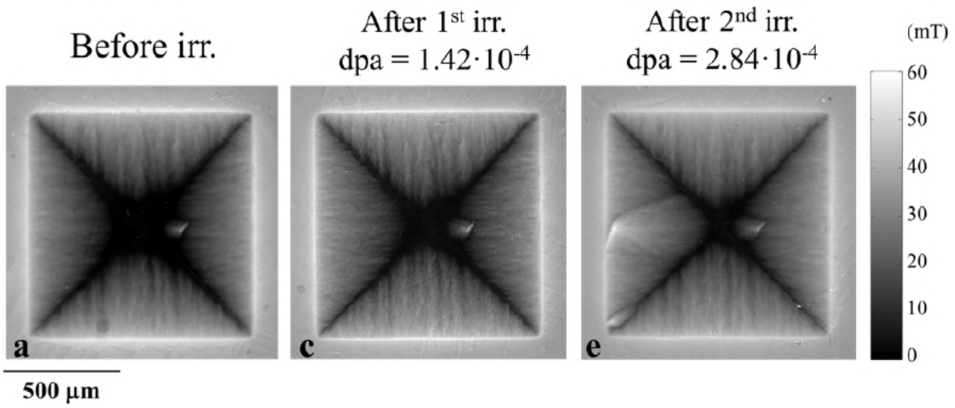

Fig. 5.5: Magnetic field penetration maps obtained by magneto-optical analysis before and after irradiation at T = 25 K for a YBCO film. dpa = $1.42 - 2.8410^{-4}$ [80].

5.1.2 Proton irradiation on Fe(Se,Te) films on metallic template

It is worth mentioning that we have recently been able to irradiate a sample grown on a buffered metal tape with protons of 3.5 MeV.

Due to time constraints, the sample was not patterned prior to irradiation. However, selective irradiation was carried out by covering part of the sample. The superconducting transition had already been measured (to ensure that a good sample was irradiated), so it was necessary to cover the contacts, which were made with silver paste. We also covered an area to be left as a reference for later measurements.

Figure 5.6 shows a diagram of how the sample was covered during irradiation. The sample was characterised by magneto-optical measurements by colleagues at the Politecnico di Torino, comparing the irradiated part with the part that remained covered. Transport measurements will be carried out as soon as the sample is properly patterned.

5.2 Au ions irradiation

5.2.1 Au ions: Fe(Se,Te) films on CaF and STO single crystals

To study the ion irradiation effect on Fe(Se,Te), we started irradiating a film deposited on CaF_2 single crystals with 320 MeV Au ions, with a dose

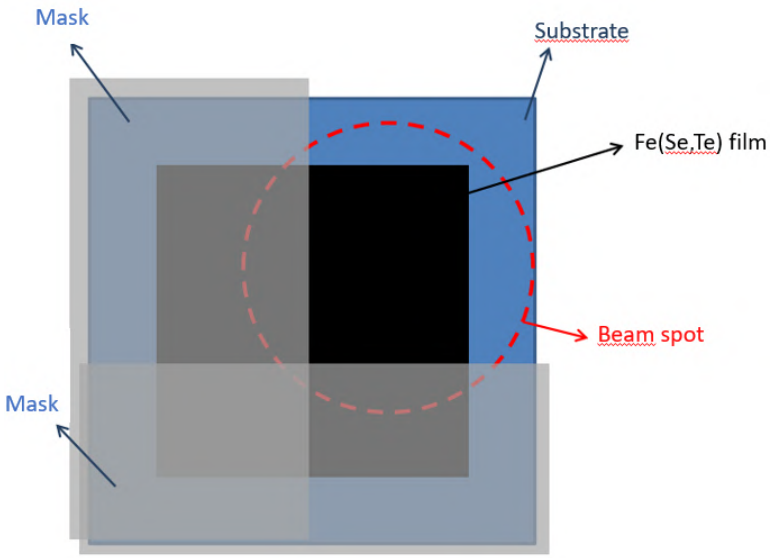

Fig. 5.6: Scheme of the mask used to irradiated the sample deposited on metallic template

of 9.7×10^{10} cm^{-2}. The corresponding "dose equivalent field", that is the field corresponding to a fluxon per incident ion, is B_ϕ=2 T.

Figure 5.7(a) shows an image of the sample prepared for transport measurements, with the unirradiated and irradiated Hall bars highlighted by light blue and dark blue squares respectively. As can be seen, prior to irradiation, the sample was patterned using optical photolitography as described in section 3.2, imprinting nine Hall bars to allow both selective irradiation of the sample (to ignore sample-to-sample variability), and transport measurements.

From resistivity measurements made in an applied magnetic field of up to 16 T, it is possible to evaluate the critical field using the 90% criterion, as shown in Figure 5.7(b) for the unirradiated and irradiated Hall bars. Figures 5.7(c) and 5.7(d) present the critical current densities as a function of field at 4.2, 8 and 12 K for the unirradiated and irradiated Hall bars, respectively. Comparing both the critical field and the critical current densities for the pristine and irradiated Hall bars, it appears that irradiation with 320 MeV Au ions has the effect of ruining the superconducting properties of the sample.

We also irradiated a film deposited on a $SrTiO_3$ (STO) single crystal patterned as in the previous case. In this case we irradiated a part of the

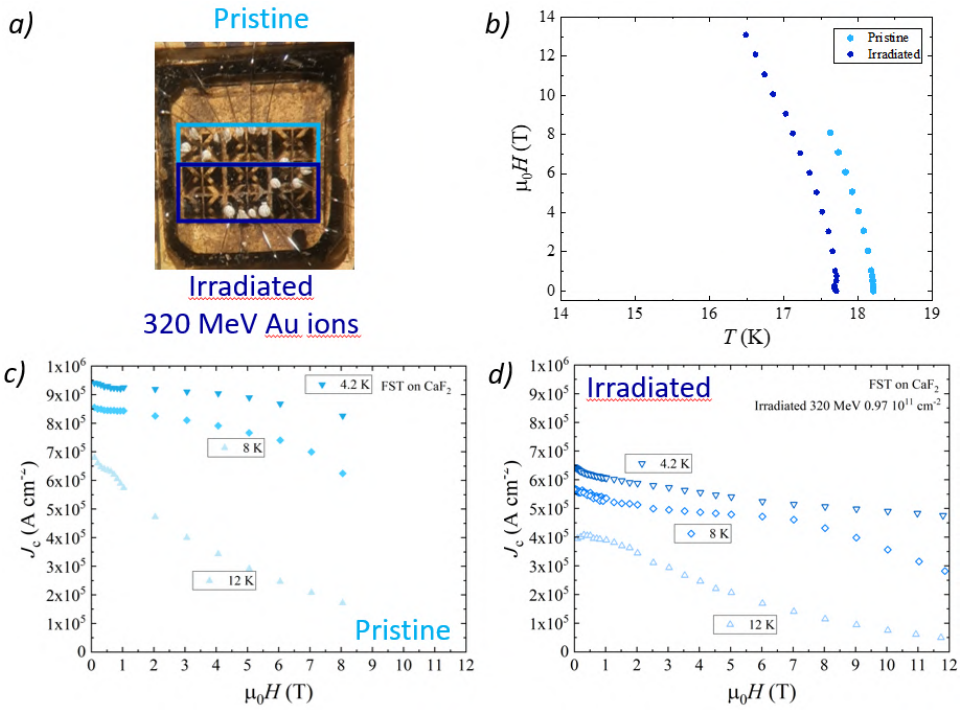

Fig. 5.7: (a) Picture of the sample irradiated with 320 MeV Au ions with a dose of 9.7×10^{10} cm^{-2} (corresponding of an equivalent field B_ϕ=2T) prepared for transport measurement. Pristine and irradiated Hall bars are highlighted by light blue and blue squares, respectively. (b) Upper critical field of pristine and irradiated Hall bars, valuated by resistivity measurements, using the 90% criterion. (c), (d) Critical current densities as a function of the filed at 4.2, 8 and 12 K of the pristine and irradiated Hall bars.

sample with 250 MeV Au ions at a fluence of 9.7×10^{10} cm^{-2}, another part at 2.9×10^{11} cm^{-2} and as usual we covered a third part for reference. The fluences correspond to equivalent fields B_ϕ of 2 and 6 T.

Figure 5.8 shows the upper critical field of pristine and irradiated Hall bars, valuated by resistivity measurements, using the 90% criterion (a), and the critical current densities as a function of the filed at 5 K of the pristine and irradiated Hall bars (b).

The first thing that is evident, as also mentioned in the section 2.4, is that the properties of the film deposited on CaF_2 are better than those of the sample deposited on $SrTiO_3$: both the upper critical field and the critical current density are lower for the sample on STO, in the pristine state. However, it is also notable that the sample deposited on STO seems to be less affected by irradiation.

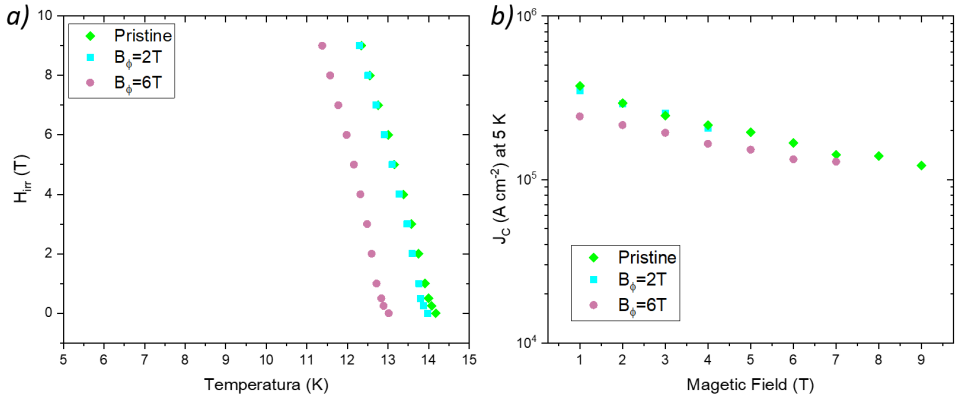

Fig. 5.8: (a) Upper critical field field of pristine and irradiated Hall bars, valuated by resistivity measurements, using the 90% criterion. (b) Critical current densities as a function of the filed at 5 K of the pristine and irradiated Hall bars.

Let's look at the effect of irradiation for an equivalent field B_ϕ of 2T applied to both samples. We can see that while the sample deposited on CaF_2 is affected by this irradiation, as already mentioned, and both the critical field and the critical current density deteriorate, the same dose on the sample deposited on $SrTiO_3$ has basically no effect on the properties, leaving both the field and the critical current density unaffected. In fact, a much higher dose and a higher equivalent field B_ϕ is required to effectively deteriorates the properties of this sample.

It is important to note that the energy of the ions used for the two experiments is slightly different, but similar enough to attribute the different effect to the differences between the samples.

This difference can be attributed to several factors. Fe(Se,Te) films tend to grow differently depending on the substrate. On CaF point-like defects are isotropically distributed in the films, whereas on STO there are some naturally grown columnar defects [34]. The introduction of columnar defects due to Au ion irradiation therefore could have a greater effect on samples grown on CaF (where this type of defect was completely absent before irradiation) than on samples grown on STO (which already had this kind of defect). In addition, the fact that the properties of samples deposited on STO are generally lower since the beginning with than those deposited on CaF_2 makes it more difficult to degrade them further. Furthermore, since heavy ions interact strongly with the substrate itself, as in the case of proton irradiation, we expect that different substrates may be affected differently.

We can therefore conclude that, as with proton irradiation, the effects of Au ion irradiation are substrate-dependent. We can also observe that for thin films deposited on single crystals, the effect of this irradiation, at least for sufficiently high doses, is a deterioration in the properties of the samples.

5.2.2 Au ions irradiation effect on structural properties: measurements at Bessy II at Helmholtz-Zentrum Berlin

To characterise the crystalline structure of micrometric Hall bars of irradiated Fe(Se,Te) thin films deposited on CaF_2 (see figure 5.7(a)), I went to the synchrotron BESSY II at Helmholtz-Zentrum Berlin (HZB) to measure X-ray diffraction with a hard X-ray nanoprobe.

The use of synchrotron light radiation in combination with the lateral resolution provided at the KMC-2 diffraction end station, together with its six goniometer configuration, can provide all the information on the microstructure and their evolution as a function of the irradiated dose. Crucial is the possibility of focusing the beam on a narrow spot on the samples, allowing the characterization of the different areas irradiated with different doses. Using the proper slits, at the KMC-2 diffraction end station, the beam size can be reduced to a $40 \times 40\ \mu m^2$. Moreover, the high photon flux at the beamline is crucial because it ensures a good quality of the signal coming from such small structures. Furthermore, the presence of a 6-circle goniometer coupled with the area detector allows for the 3D-scanning of the peaks, hence detection of microstrains along the different crystallographic directions. All those conditions are impossible to achieve with laboratory equipment.

The aim is to characterise the structural changes induced by ion irradiation on Fe(Se,Te) thin films and on the substrate by implantation of irradiating particles. As shown in section 5.1, these changes in the structure of the films affect the superconducting properties of the film. One of the advantages of the focused beam is that it allows us to analyse the effects of irradiation on the same sample that is only partially irradiated. In this way we can avoid differences due to sample variability and be confident that the observations made are due to irradiation alone.

The KMC-2 diffraction station is equipped with a sample holder with six degrees of freedom, which allowed us to study not only reflections generated

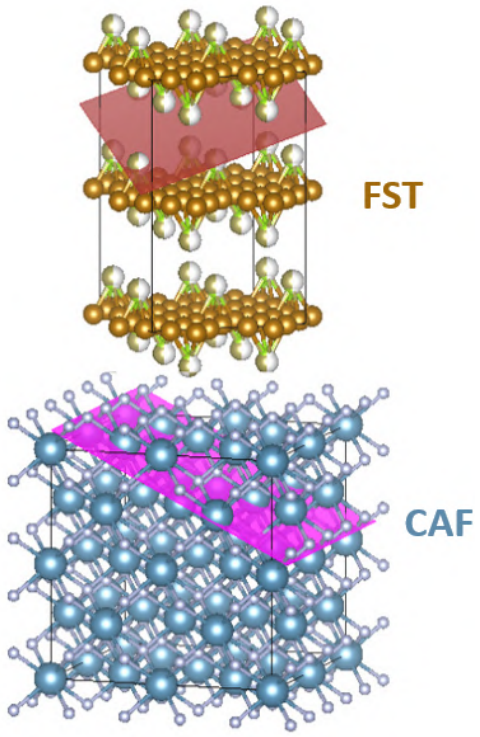

Fig. 5.9: Typical structure of FST (in brown) deposited on Caf single crystal (in blue). In this figure asymmetric planes are highlited, in detail (115) for FST and (422) for CaF

by (*00l*) direction, but also asymmetric reflections of the type (*hkl*). The (*00l*) reflections allow us to calculate the variation of the lattice parameters along the c axis, while the (*hkl*) are useful to evaluate variations of the lattice parameters in the ab plane.

We acquired data on the reflections of symmetrical peaks (*002*) for Fe(Se,Te) and (*200*) for CaF_2, while we chose (*115*) from Fe(Se,Te) and (*422*) from CaF_2 as asymmetrical peaks. These peaks were chosen on the basis of which peaks were accessible, together with an evaluation of their theoretical intensity. Figure 5.9 shows the typical structure of Fe(Se,Te) (in brown) deposited on CaF_2 single crystal (in blue). In this figure asymmetric planes are highlited, in detail (*115*) for Fe(Se,Te) and (*422*) for CaF_2.

After appropriate processing of the data acquired with the area detector, we obtained real-space maps showing the position of the peaks for the film and the substrate, relative to both pristine and irradiated Hall bars. Figure 5.10 shows maps in real space for the peaks (*002*) of the pristine (*a*) and irra-

diated (c) Fe(Se,Te), and the peaks (*200*) of the pristine (b) and irradiated (d) CaF_2.

In order to determine the position and width of the peaks shown in the maps, the experimental data were fitted using a two-dimensional Gaussian. Afterwards, we extracted a profile, considering the maximum intensity along the η direction. In the graphs reported in panel (e) and (f) of figure 5.10, the as-prepared and irradiated peaks are reported for film and substrate respectively.

It is observed that the position and width of the Fe(Se,Te) peak is not affected by irradiation, unlike the substrate. In fact, looking at panel (f), a shift of the peak relative to the CaF_2 towards lower angles when irradiated is observed. This suggests that irradiation by gold ions has the effect of inducing a more pronounced variation of the crystalline parameter along the c-axis in the substrate than is observed for the film.

This is only a preliminary analysis, carried out by comparing two strips on symmetrical peaks only. a more detailed analysis will be carried out, both by increasing the statistics (all 9 Hall bars were measured at the synchrotron) but above all by also evaluating the effects on asymmetrical peaks. By evaluating the relative differences between the position of the Fe(Se,Te) peaks and that of the substrate, we will be able to assess the strain induced by irradiation.

The variations observed before and after irradiation in the crystal structure of the film and substrate can be linked to changes in the superconducting properties of the Hall bars. In this way, we can unravel the interplay between the microstructure and superconducting properties, and thus better understand the effect of irradiation.

5.2.3 Au ions: Fe(Se,Te) films on CZO-buffered YSZ

Politecnico di Torino irradiated three samples I deposited on YSZ single crystals covered by a CZO buffer layer, using 250 MeV Au ions. The three samples irradiated with the Au ion beam at 250 MeV energy are shown in figure 5.11. One sample was patterned with 9 Hall bars with a channel of $20 \times 50 \mu m^2$; three of them were covered during the beam exposure to compare the irradiation effects on the same sample, to exclude sample to

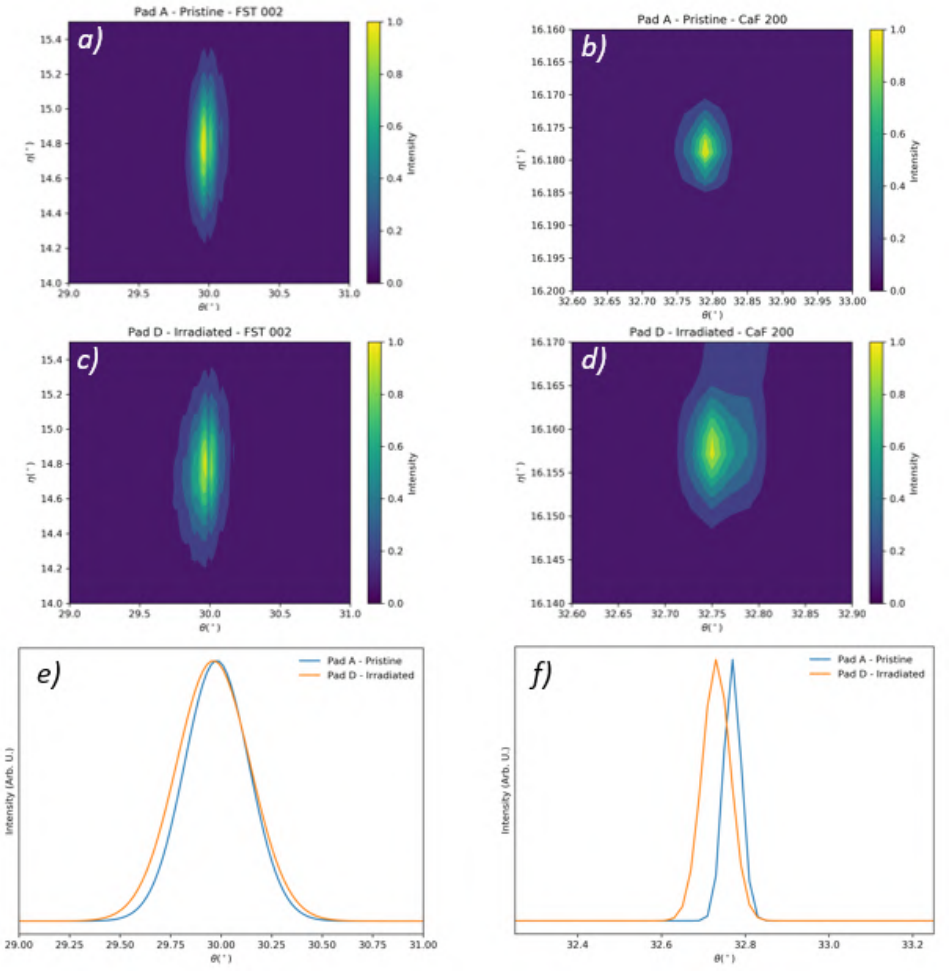

Fig. 5.10: Maps in real space for the peaks (002) of the pristine (a) and irradiated (c) Fe(Se,Te), and the peaks (200) of the pristine (b) and irradiated (d) CaF_2. Panel (e) and (f) show the as-prepared and irradiated profile peaks, compared for film and substrate respectively.

sample variability. Of the remaining six, two were irradiated with a fluence of $\phi = 9.7 \times 10^{10}$ Au ions cm^{-2}, two with $\phi = 1.94 \times 10^{11}$ Au ions cm^{-2} and the last with $\phi = 2.9 \times 10^{11}$ Au ions cm^{-2}, corresponding to equivalent fields of 2, 4 and 6 T, respectively. The other two samples were patterned with two Hall bars with a channel of $50 \times 500 \mu m^2$, to be characterized by ENEA up to 16 T; one sample was irradiated with an equivalent field of 4 T and the other with an equivalent field of 6 T; this latter sample was further irradiated in a second irradiation run, bringing the equivalent field up to 10 T, after a first characterization.

I characterized the sample with 9 Hall bars in a Physical Properties Measuring System (PPMS) by Quantum Design up to 9 T, while the other two samples has been characterized by ENEA up to 16 T.

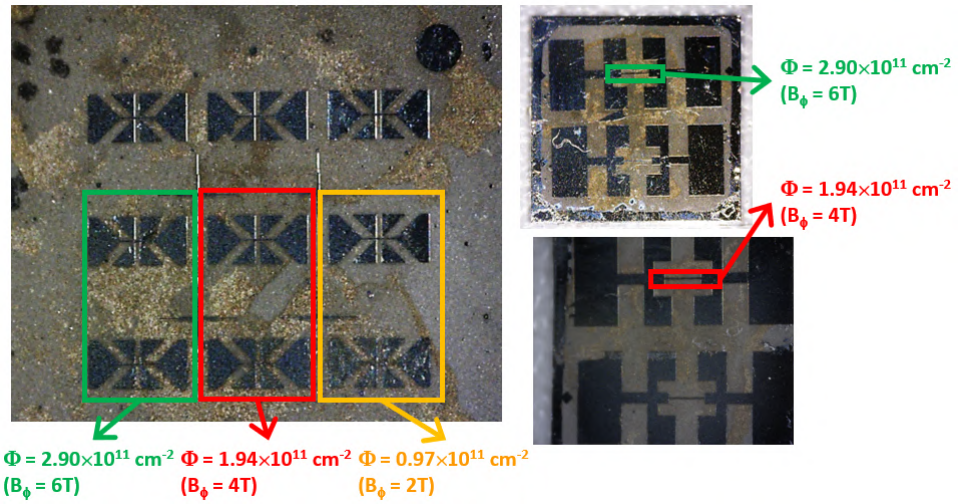

Fig. 5.11: Images of the three 250 MeV gold-irradiated samples, one patterned with 9 Hall bars with a channel of $20 \times 50 \mu m^2$, and two with two Hall bars with a channel of $50 \times 500 \mu m^2$. Irradiated Hall bars are highlighted by colored squares, yellow for $B_\phi = 2$ T, red for $B_\phi = 4$ T, and green for $B_\phi = 6$ T. The channel irradiated with an equivalent field of 6 T for the sample with two Hall bars was irradiated in a second run up to 10 T, after a first characterization.

B_ϕ of 2, 4 and 6 T

I characterized the sample with 9 Hall bars up to 9 T. The resistivity as a function of the temperature for a representative Hall bar in the pristine state, B_ϕ=2T, B_ϕ=4T and B_ϕ=6T is shown in figure 5.12(a).

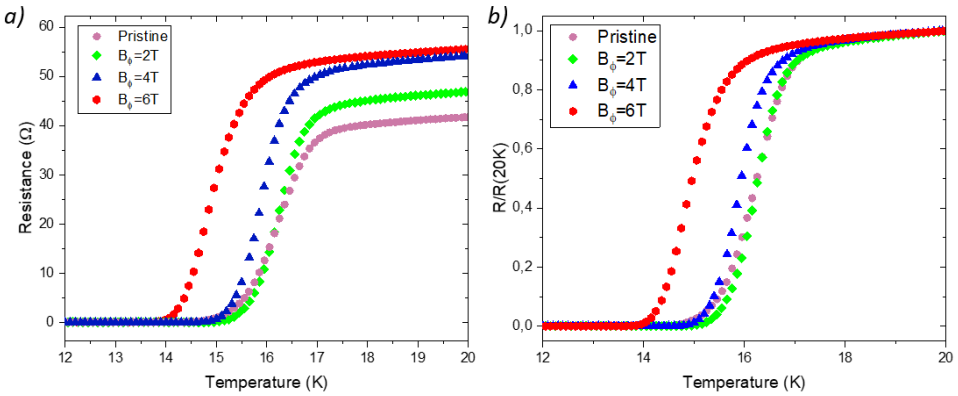

Fig. 5.12: (a) Resistivity as a function of temperature for the pristine and the irradiate Hall bars, with an equivalent field of B_ϕ 2, 4 and 6 T. (b) Resistivity as a function of temperature for the same Hall bars, normalized for the resistance at 20K.

Irradiation has the effect of introducing defects into the superconducting film, and the presence of defects increases the resistance in the normal state. The higher the dose, the greater the number of defects introduced, and hence the higher the normal state resistance, as as shown in figure 5.12(**a**).

To emphasise the shift of Tc with irradiation the resistivities are normalized in respect with their values at 20 K; those values are shown in figure 5.12(b) for each Hall bar.

We observe that the onset of the critical temperature decreases with exposure: the higher the dose (i.e. the equivalent field), the lower the onset. But we can also see that the behaviour of the amplitude of the transition is different: the transition gets narrower for the irradiated strips. ΔT_c is $\sim$ 1.5 K for the pristine Hall bar, and it reduces at $\sim$ 1.2 and $\sim$ 0.9 K for the Hall bar irradiated with an equivalent field of 2 and 4 T, respectively.

This behaviour is also observed by increasing the applied magnetic field.

Figure 5.13 shows the resistance as a function of temperature at increasing applied field (0 to 9 T) for the pristine (a) and irradiated Hall bars ((b) B_ϕ 2 T, (c) B_ϕ 4 T and (d) B_ϕ 6 T). We an observe that T_c^0 is higher for the irradiated Hall bars (B_ϕ of 2 and 4 T), than the pristine one. We can also notice that the behaviour of the four Hall bars is slightly different when a magnetic field is applied.

This is consistent with the behaviour of the upper critical field H_{C2} and of the irreversibility field H_{irr}. These values are obtained by intersecting the

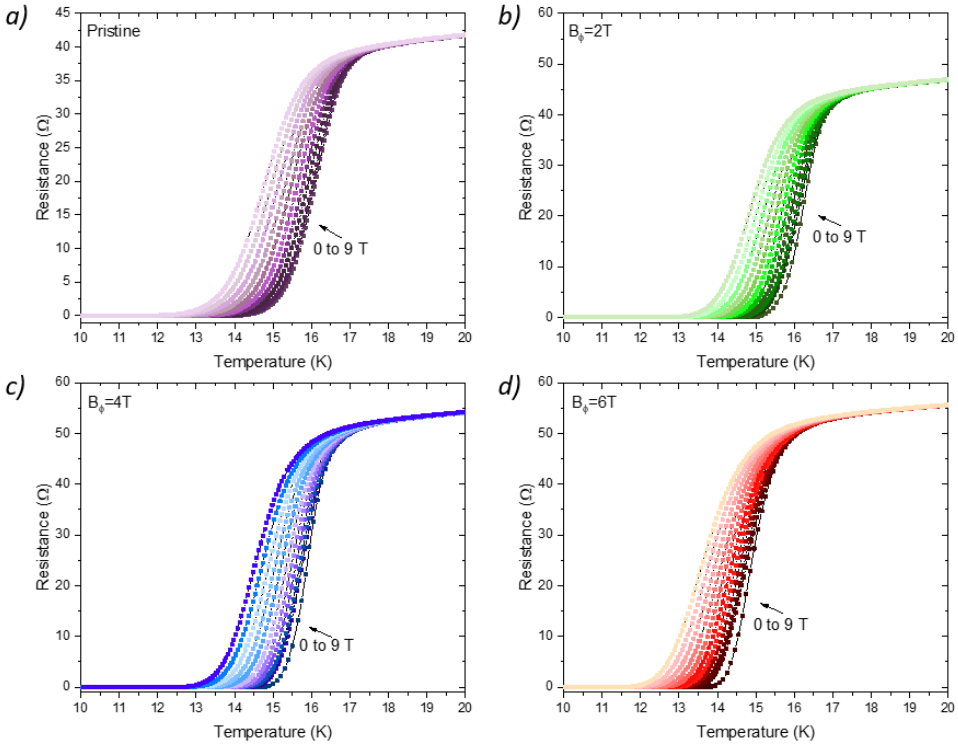

Fig. 5.13: Resistance as a function of temperature at increasing applied field (0 to 9 T) for the pristine (a) and irradiated Hall bars ((b) B_ϕ 2 T, (c) B_ϕ 4 T and (d) B_ϕ 6 T).

two straight lines, the continuation of the normal resistance and the transition; the point of intersection of these two lines is taken as the reference. H_{C2} is calculated as 90% of this value, while H_{irr} is calculated as the 10%. Both are shown in figure 5.14 panel (a) and (b), respectively.

The slope of the upper critical field H_{C2} increases as the dose increases, as can be seen from the figure 5.14(a), that shows the upper critical field H_{C2} as a function of the reduced temeprature t (T/T_c^{onset}). This behaviour was already predicted by the superconducting transition. It is consistent with what has been observed in literature (e.g. in [76]), and also with what we have seen on Au ion irradiated Fe(Se,Te) films deposited on single crystals.

Instead, the irreversibility field shows unexpected behaviour. Typically, high energy Au irradiation has the effect of worsening the irreversibility field as the dose increases. This has been observed, for example, for Fe(Se,Te) films deposited on single crystals. But in this case the irreversibility field increases slightly at least for $B_\phi = 4$T (i.e. a dose of up to $\phi = 1.94 \times 10^{11}$ Au ions

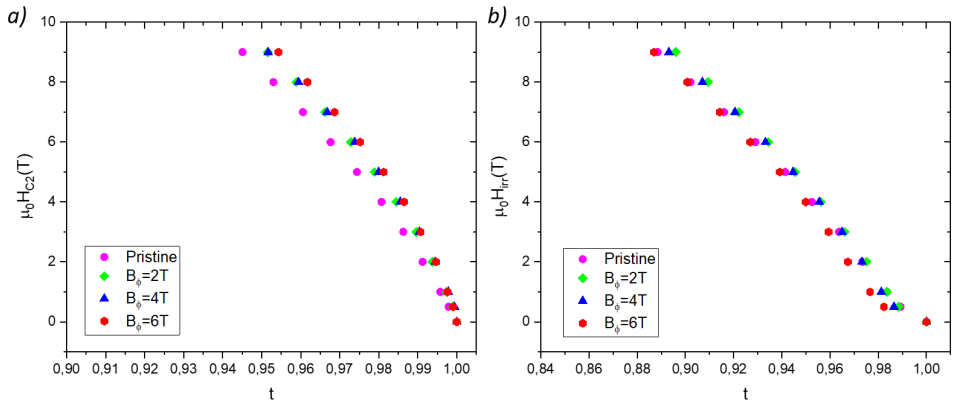

Fig. 5.14: (a) Upper critical field H_{C2} in function of the reduced temperature t (T/T_c^{onset}) for the pristine and the irradiate Hall bars, with an equivalent field of B_ϕ 2, 4 and 6 T, valuated by resistivity measurements, using the 90% criterion. (b) Irreversibility field H_{irr} in function of the reduced temperature t (T/T_c^0) of pristine and irradiated Hall bars (2, 4 and 6 T), valuated by resistivity measurements, using the 10% criterion.

cm^{-2}), as shown in figure 5.14(b), where the ireversibility field is plotted as a funcion of the reduced temeprature t (T/T_c^0), for pristine and irradiated Hall bars. This effect is compatible with the introduction of effective pinning centres.

Figure 5.15 shows the critical current density of the irradiated Hall bar (2, 4 and 6 T) compared to the pristine, as a function of the applied field (perpendicular to the ab plane), at 8 K. From these measurements it is clear that Au ion irradiation has a beneficial effect on the sample itself, improving the critical current density for every dose. It appears that the higher enhancement compared to the pristine state is associated with the lower dose, and then critical current density tends to decrease as the dose increases.

These improvements could be linked to the defects introduced by 250 MeV Au ions irradiation: correlated linear defects. This type of defects can affect the pinning of the superconducting vortices. The improvement in the pinning effect is undeniable and it is particularly evident when observing the change in the critical current density for the different Hall bars.

The increase in H_{irr}, which is compatible with an effective pinning, is also evident form these J_c measurements (figure 5.15). J_c increases in absolute value, but it also changes its behaviour in the applied field, becoming flatter as the field increases.

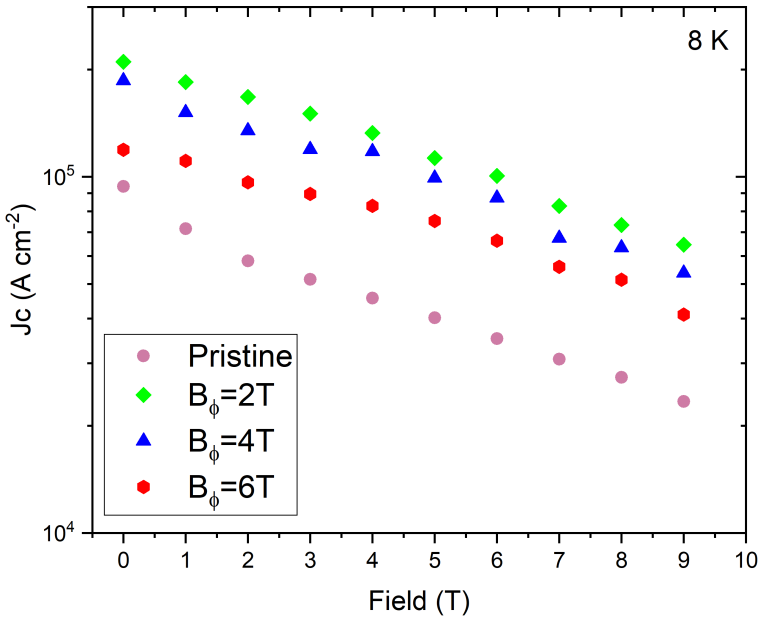

Fig. 5.15: Critical current density of the irradiated Hall bar (2, 4 and 6 T) compared to the pristine, as a function of the applied field (perpendicular to the *ab* plane), at 8 K.

B_ϕ of 4, 6 and 10 T

To confirm the beneficial effect on the superconducting properties associated with Au irradiation, two more samples were irradiated and characterised. The two samples, each patterned with two Hall bars with a channel of $50 \times 500\mu m^2$ (shown in figure 5.11), were deposited in exactly the same condition as the previous one (both for the buffer layer and for the superconducting film). For each sample, one Hall bar was covered during irradiation and measured as the untouched part of the sample. One sample was irradiated with an equivalent field of 4 T and the other with an equivalent field of 6 T. For this last sample, after a first characterisation, a second irradiation run brought the equivalent dose on this Hall bar up to 10 T. The characterization of these two samples have been performed up to 16 T by ENEA.

The resistivity measurements for the two samples are shown in figure 5.16. If we consider figure 5.16 (a), we notice that an irradiation at equivalent field of 6 T lowers the critical temperature. In addition, in this sample we

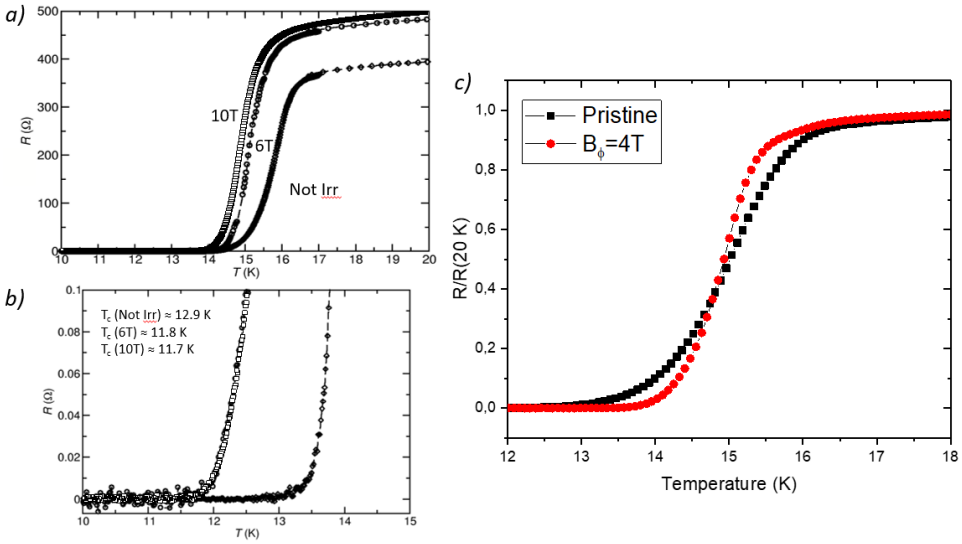

Fig. 5.16: (a) Resistivity as a function of temperature for the pristine and the irradiate Hall bars, with an equivalent field of B_ϕ 6 and 10 T. (b) Transition foot zoom; (c) Resistivity as a function of temperature for the pristine and irradiated with B_ϕ of 4 T Hall bars, normalized for the resistance at 20K.

can see that further irradiation to reach an equivalent field of 10 T seems to further worsen the critical temperature. However, if we look at panel (b), we can see that T_{C0} is indeed equivalent for the Hall bar irradiated at 6 T and irradiated at 10 T, and about 11.8 K, while in the pristine state was about 12.8 K.

Figure 5.16(c) shows the superconductive transition for the last sample, of which one of the strips was irradiated with an equivalent field of 4 T, normalized at the resistance at 20 K. As with the previous sample, we observe a worsening of the critical temperature onset, but a significant narrowing of the transition. In this case, ΔT_c goes from a value of about 3.5 K in the pristine case to one of about 2 K for the Hall bar irradiated at B_ϕ 4 T.

Figure 5.17 shows the critical current densities, at 4.2 and 6K, for the two samples patterned with two Hall bars, measured by ENEA up to 16 T.

Also for these two samples, it appears that Au ion irradiation has a beneficial effect on the transport properties of the films. For both samples the critical current density is increased after irradiation. Thanks to the measurements up to 16 T, the beneficial effect of irradiation on the in-field behaviour is even more evident in these measurements. In particular for the sample irradiated

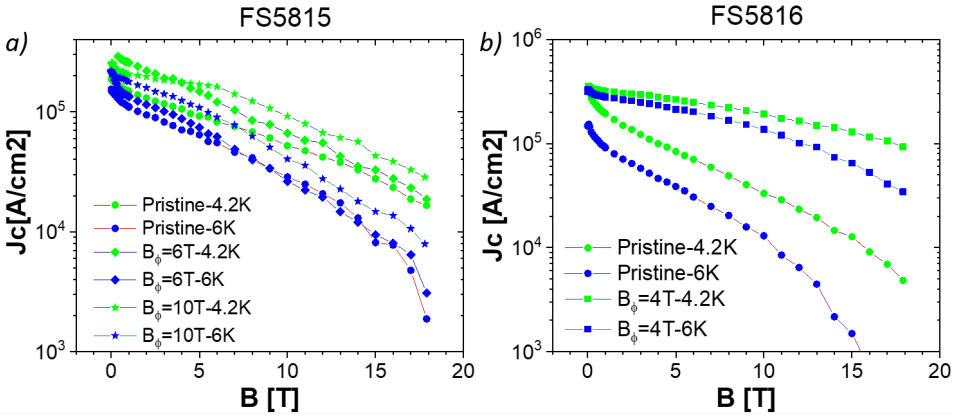

Fig. 5.17: Critical current density of the irradiated Hall bar (of B_ϕ 6 and 10 T (*a*), B_ϕ 4 T (*b*)) compared to the pristine for each sample.

at B_ϕ 4 T. In fact, it can be observed that the critical current density J_c tends to deteriorate, as the magnetic field increases, less in the irradiated Hall bar than in the pristine one.

What we expect from Au ion irradiation is the introduction of correlated defects which has actually a beneficial effect on vortex pinning, especially when the field is in the direction of the defects themselves, i.e. perpendicular to the *ab* plane, as in all the measurements shown above. It may therefore be of particular interest to study how the transport properties of the sample vary as a function of the angle at which the field is applied relative to the *ab* plane of the sample.

Figure 5.18 shows the critical current density J_c as a function of the angle between the *ab* plane of the sample and the applied field (the applied field H is parallel to *ab* when θ=90°).

The pristine Hall bar shows the typical anisotropy, meaning that the value of the critical current density varies when the field is applied parallel to the *ab* plane (i.e. $\theta = 90°$) or perpendicular to it ($\theta = 0°$). The two bumps at $\theta = \pm\ 90°$ mean that the pinning is strong in the in-plane direction, and weaker along the *c* axis.

The effect of gold ions irradiation is to increase the value of the critical current when $\theta = 0°$ with respect to $\theta = 90°$, thanks to the pinning introduced in the direction of the *c* axis. As a result, the anisotropy is lower in the irradiated strips than in the pristine ones.

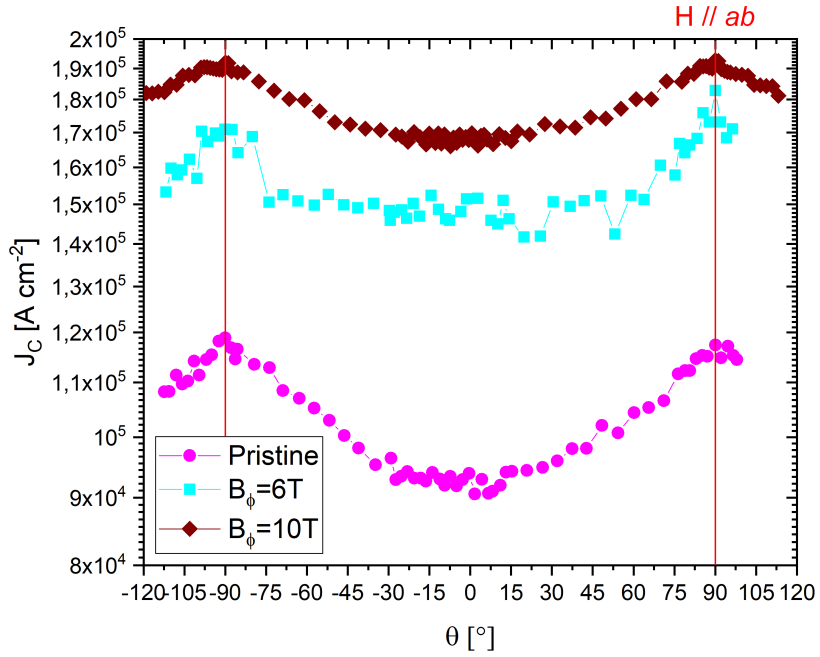

Fig. 5.18: Angular dependence of the critical current density $J_c(\theta)$ evaluated at 5T and 4.2 K, for the undisturbed Hall bar and the one irradiated with the equivalent field B_ϕ of 6 and 10 T.

Figure 5.19 shows the pinning force as a function of the applied field at different temperatures of 4.2 and 6 K, with field perpendicular to the *ab* plane, for the pristine Hall bar, and the irradiated one with B_ϕ=6T. From this graph it can be seen that the pinning force is greater for the irradiated Hall bar than for the pristine Hall bar at both temperatures, proving that the introduction of defects by Au ion irradiation was effective.

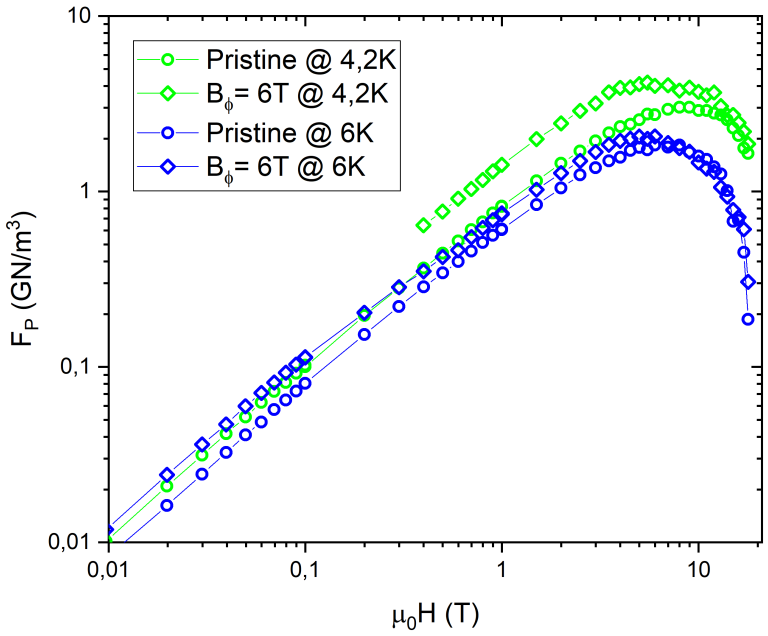

Fig. 5.19: Pinning force as a function of the applied field at different temperatures of 4.2 and 6 K, with field perpendicular to the *ab* plane, for the pristine Hall bar, and the irradiated one with B_ϕ=6T.

5.3 Neutron irradiation

Frascati Neutron Generator

Figure 5.20 shows examples of calculated neutron spectra produced by different fusion facilities. It is clear that, regardless of the tokamak considered, there is a large peak of fast neutrons at 14 MeV released by the plasma. Most neutron irradiation facilities do not reach such energies; the TRIGA reactor [84] spectrum is shown for comparison in figure 5.20.

Frascati Neutron Generator (FNG) is a facility for experiments using neutrons with an energy of 14 MeV, i.e. those produced in nuclear fusion reactions between deuterium and tritium nuclei. These are both isotopes of hydrogen that have one (deuterium) or two (tritium) more neutrons. Similar to the tokamak machines used to study nuclear fusion for energy production, fusion reactions at FNG require sufficient initial energy to start the reaction. To do this, an accelerator of deuterium ions causes them to collide

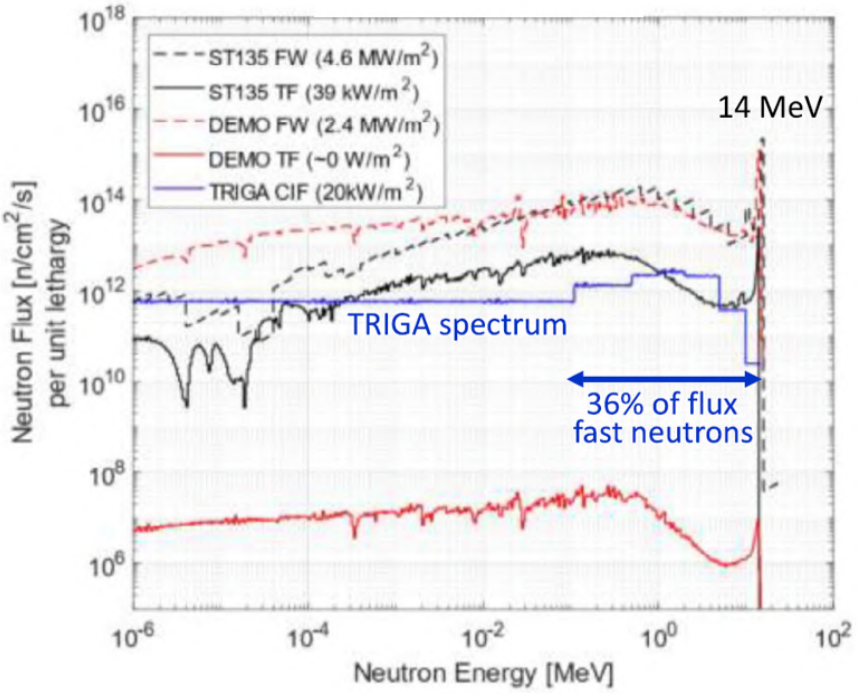

Fig. 5.20: Example of calculated neutron spectra produced by fusion facilities compared to neutrons produced by TRIGA (blue line) [9].

with a target containing tritium, resulting in the fusion of the two nuclei and the subsequent emission of neutrons and helium nuclei. The neutron flux achieved by the FNG is one of the most intense in the world: 10^{11} neutrons can be emitted from the target per second, making the FNG a unique facility in the international scene.

Figure 5.21 shows the simulated neutron spectra at different neutron emission angles and the iso-flux contours, obtained by Monte Carlo simulations.

It can be noted that the neutron spectrum is almost monochromatic. Spectrum broadening is angle-dependent, being the narrowest at θ=90°. The overall broadening of the spectrum at different angles depend on kinematics [85].

We have irradiated two series of Fe(Se,Te) thin films. The first consists of Fe(Se,Te) films deposited on a 5mm×5mm CaF_2 single crystal divided into four equal parts on which thin films have been deposited simultaneously by PLD, so that we can consider them to be virtually the same sample; figure 5.22(a) show the four samples right after deposition. The second

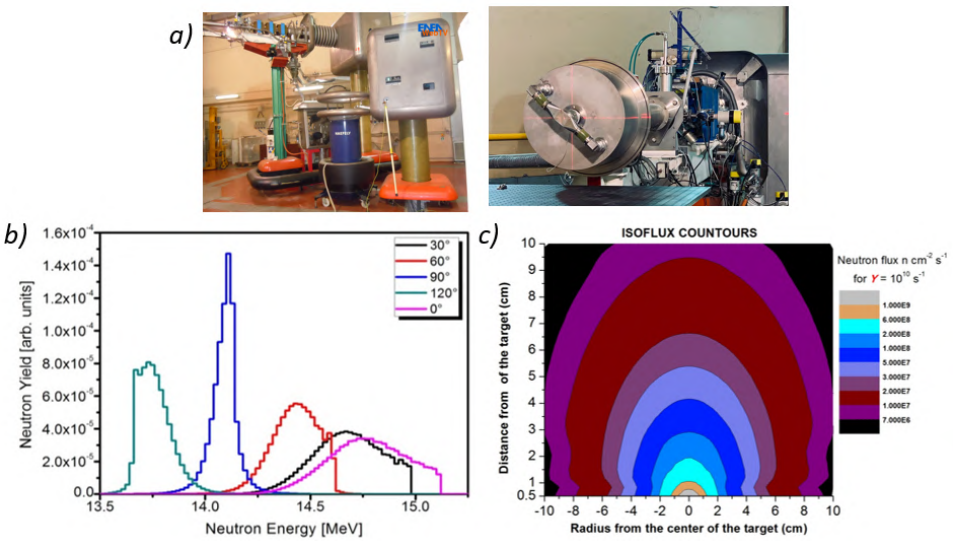

Fig. 5.21: (*a*) The FNG facility; (*b*) example of FNG neutron spectra as a function of the neutron emission angle; (*c*) iso-flux contours of FNG [85].

series consists of four twin samples deposited on CZO-buffered YSZ single crystals. For each series, we irradiated one sample for one, two and three days respectively at the FNG facility, leaving the fourth sample unirradiated for comparison. A representative picture of the samples is reported in figure 5.22(*b*), the pink square highlights the sample deposited on CaF_2, while the blue the sample on CZO-buffered YSZ.

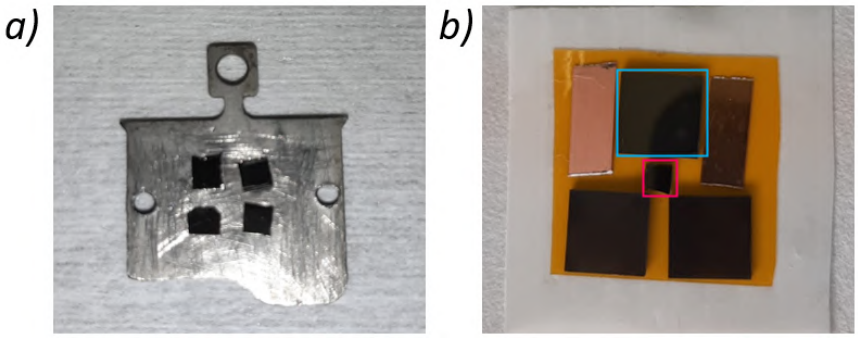

Fig. 5.22: (*a*) Four samples on CaF_2 right after deposition; (*b*) A representative picture of the samples: the pink square highlights the sample deposited on CaF_2, while the blue the sample on CZO-buffered YSZ.

Since there is no real particle beam, unlike previous irradiations, it was not possible to irradiate a single sample selectively, but several had to be irradiated and one of each type kept as a reference. In addition, it was not

possible to measure the samples before and after irradiation with resistivity analysis because we use silver paint to contact the sample, which cannot be completely removed from the sample surface and can cause additional damage during irradiation. Therefore, we cannot ignore the sample-to-sample variability in the case of samples deposited on CZO-buffered YSZ.

The total dose that the three-day irradiated samples underwent was 1.2×10^{14} neutrons cm^{-2}; from this we can roughly say that the one-day irradiated sample received one third of this dose and the two-day irradiated sample two thirds, resulting in 4×10^{13} and 8×10^{13} neutrons cm^{-2} respectively. this quick calculation does not take into account the consumption of the target during irradiation, but is reasonably close to the actual dose.

Figure 5.23 reports the SQUID measurements of two samples deposited on CaF_2 single crystals, in particular the three-day irradiated, in pink in the graphs, and the pristine, in green. The figure shows the zero field cooling (ZFC) measurements (panel (a)) and the magnetisation cycles (panel (b)) of the two samples.

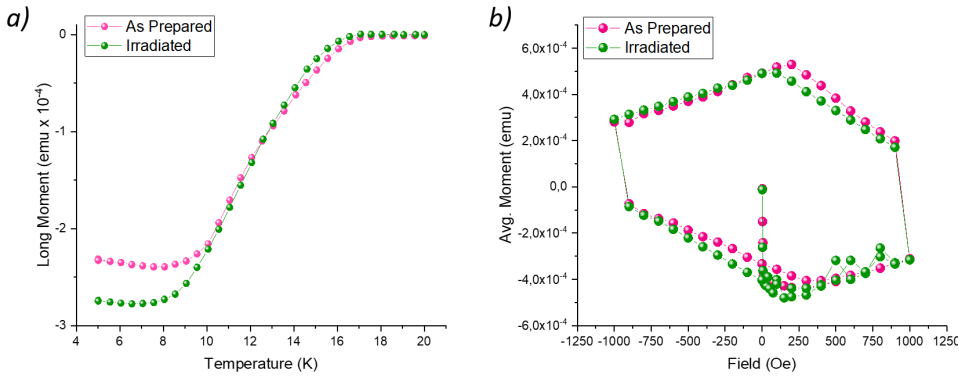

Fig. 5.23: SQUID measurements on samples deposited on CaF_2, pristine (pink) and three-day irradiated (green). Panel (a) shows zero field cooling (ZFC) measurements, to evaluate the critical temperature, while panel (b) shows the magnetisation cycles.

Figure 5.24(a) shows XRD spectra of the four samples deposited on CZO-buffered YSZ single crystals, while 5.24(b) reports the resistivity measurements of the same samples, to evaluate the critical temperature changes after 4×10^{13}, 8×10^{13} and 1.2×10^{14} neutrons cm^{-2} irradiation.

From these measurements it can be concluded that neither the lattice structure nor the critical temperature is affected by neutron irradiation. It appears that the dose of 1.2×10^{14} neutrons cm^{-2} has no effect on Fe(Se,Te)

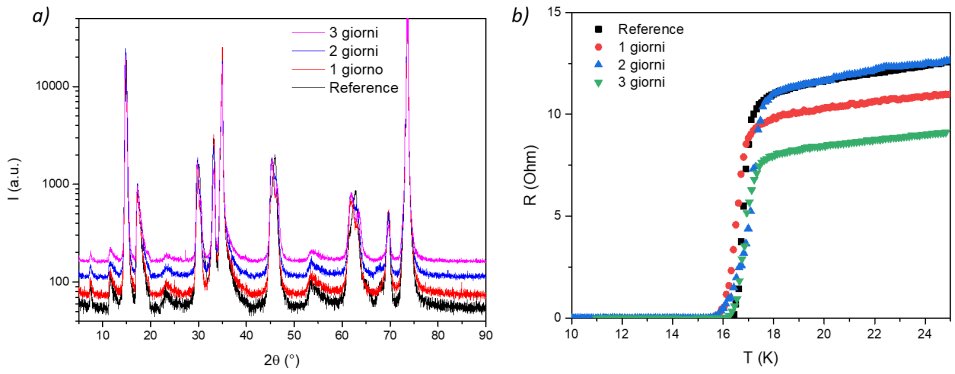

Fig. 5.24: Analysis on samples deposited on CZO-buffered YSZ, for the pristine sample and the irradiated ones. Panel (*a*) shows XRD spectra of the four samples, while panel (*b*) shows the resistivity measurement, to evaluate the critical temperature.

films.

Third harmonic analysis

I measured, before and after neutron irradiation, the series of samples deposited on CZO-buffered YSZ single crystals, analysing the third armonic response of the samples, thanks to the method described in *Appendix A*. A major advantage of this method is that it is a completely non-invasive measurement, which allowed us to analyse the samples before irradiation without the risk of damaging the surface of the sample, for example with silver paste contacts that can be activated during neutron irradiation. It is also more sensitive and provides more information than resistivity.

Figure 5.25 shows normalised peaks of the third harmonics of samples deposited on CZO-buffered YSZ single crystals before (red dots) and after (blue triangles) neutron irradiation with 4×10^{13} (1-day), 8×10^{13} (2-day) and 1.2×10^{14} (3-day) neutrons cm^{-2}, together with the unirradiated sample (first panel). The measurements on this last sample are unchanged before and after irradiation, i.e. in this case simply immediately after deposition and after the time required to irradiate the twin samples. We can therefore be sure that any differences we find in the irradiated samples are due to irradiation and not to ageing.

As far as the irradiated samples are concerned, the first thing we can notice is that the right onset of the third harmonic peak, attributed to the

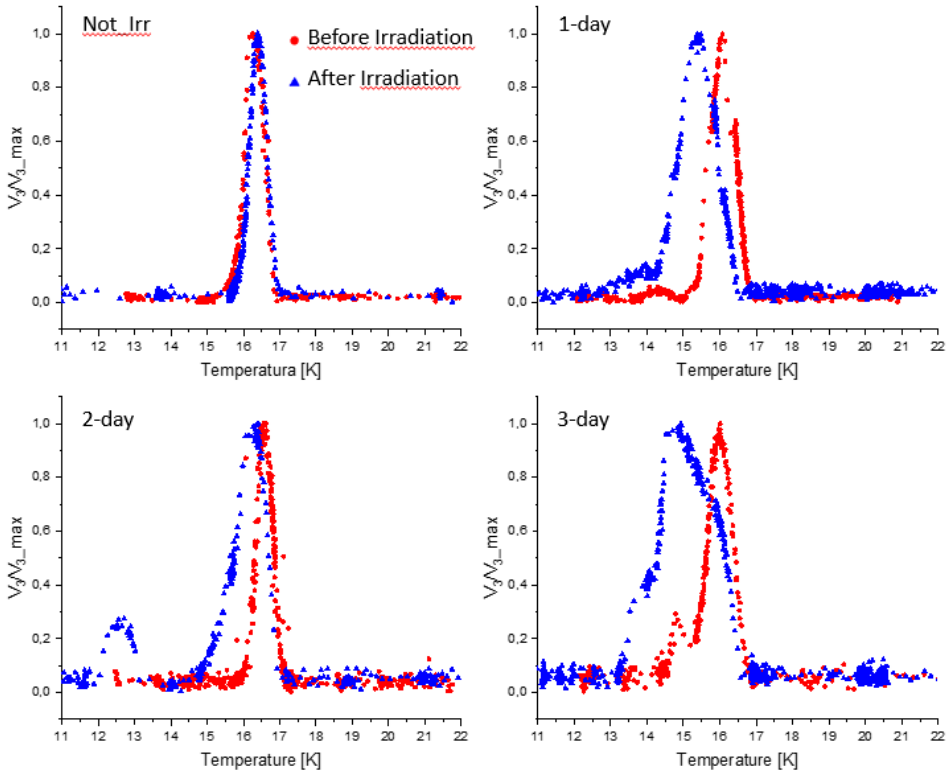

Fig. 5.25: Measures of third harmonics (normalized to the maximum of the peaks) of samples deposited on CZO-buffered YSZ single crystals before (red dots) and after (blue triangles) neutron irradiation with 4×10^{13} (1-day), 8×10^{13} (2-day) and 1.2×10^{14} (3-day) neutrons cm^{-2}. The unirradiated sample is reported for comparison.

irreversibility temperature, does not move for any sample before or after irradiation, confirming what was observed in the transport measurements (Figure 5.24(b)). However, for all the irradiated samples we can see a difference in the shape of the peak, suggesting that neutron irradiation did indeed have some effect on the samples, influencing the properties of the films. In particular, we can see from these measurements that T_c^0 remains unchanged (i.e. the first foot of the peak does not move), which is consistent with the transport measurements. On the other hand, the slight shift of the second foot of the peak can be attributed to a slight worsening of the critical field H_{C1}. H_{C1} is inversely proportional to λ^2, so a decrease in H_{C1} is associated with an increase in λ, i.e. an increase in disorder within the sample.

We should bear in mind that the maximum dose of 1.2×10^{14} neutrons cm^{-2} received by the most irradiated samples is very far from the dose that can be

produced inside a tokamak in 10 years of operation, which is the minimum time that magnets should be guaranteed to work in fusion plants. Further studies at higher fluences are therefore needed.

Chapter 6

Conclusions

The strong growth in the demand for power nowadays requires a strong effort in the search for green and functional technologies for energy production. One promising route is to build nuclear fusion power stations. This solution is closely linked to superconductors: high field superconducting magnets are needed for plasma confinement. Today, fusion power plants using the tokamak design employ low-temperature superconductors (NbTi and Nb_3Sn), for devices such as **ITER** and **DEMO**, and some attempts are being made with high-temperature superconductors (YBCO), such as **SPARC**.

Since their discovery in 2008, iron-based superconductors have proven to be a viable alternative for the production of high-field magnets due to their critical temperatures, good for applications (maximum T_c ∼56 K), and especially for high upper critical fields (H_{C2} above 50 T). Of all the iron-based superconductors, the one I have focused on is iron selenium tellurium, which is very interesting because it is the only one of all the families that does not contain arsenic and has the lowest anisotropy. The requirements for using Fe(Se,Te) in a fusion plant are as follows:

- To be able to obtain a conductor with this phase;
- To understand whether the material can survive so close to the plasma, i.e. in a highly radioactive environment.

My thesis focused mainly on these two aspects:

1. Try to demonstrate the feasibility of a simple coated conductor using the Fe(Se,Te) phase.
2. Test the robustness of this material against irradiation from different charged and neutral particles at different energies.

A coated conductor (CC) is a conductor designed for ReBCO superconductors and is very complex because these materials must be perfectly epitaxial to have good transport properties. A CC consists of a metal tape covered by a series of buffer layers, which act as a chemical barrier between the superconductor and the metal, but above all optimise the epitaxial growth of the superconductor. The superconducting film is grown on top of the buffers. Technical substrates designed for ReBCOs have been used to produce Fe(Se,Te) coated conductors and other iron-based conductors with optimum results. However, for this material to be competitive with ReBCOs, its complexity needs to be reduced.

To obtain a simple coated conductor, I started by optimising the growth of Fe(Se,Te) thin films on single crystals, based on the long experience of the group at the CNR Spin Institute in Genova. The next step was to select the buffer layers to be used. The aim was to reduce the number of buffers to one by finding a material with a good lattice match with Fe(Se,Te) and that could be produced cost effectively.

ENEA has been involved in the production of zirconia-doped ceria thin films as buffers using a chemical technique, a process that is therefore industrially scalable. In order to concentrate on studying the interactions between the superconducting film and the buffer, the latter was first grown on single crystal. I optimised the growth of Fe(Se,Te) films on these samples until I obtained the same performance as the films grown on single crystal. At this point, the final step was to switch to metal templates.

Thin zirconia-doped ceria films were grown by ENEA on textured nickel tungsten (NiW 5%wt.) tape. This type of substrate is much more complicated than the previous ones and it was not easy to obtain samples with good properties because the orientation of the Fe(Se,Te) films is much more delicate.

After several optimisations of both the buffer by ENEA and the film deposition by me, we managed to obtain a series of samples with a very good superconducting transition. This has been the first Fe(Se,Te) CC entirely fabricated in house, with a very simple architecture and a very thin (25 nm) buffer layer. The critical temperature and especially the critical current can be further improved. Nevertheless, this is an excellent result as we have demonstrated the feasibility of a simple, low-cost CC using a buffer layer grown by a technique that can be implemented on a large scale.

In order to use Fe(Se,Te) for winding magnets for nuclear fusion reactors, it is essential to understand the effects of irradiation on its properties. The main type of radiation emitted by the plasma inside fusion power plants is that of neutrons, in particular fast neutrons, i.e. neutrons with an energy greater than 0.1 MeV, up to a maximum of about 14. However, neutrons of these energies are very difficult to obtain in large quantities; the most common way is to use small fusion reactors as sources, but these cannot achieve high energies. Charged particle radiation is often used to simulate the effects of neutron radiation.

Fe(Se,Te) films were irradiated, in collaboration with the Politecnico di Torino, with protons, gold ions and monocromatic fast neutrons (energy 14 MeV). We irradiated both samples deposited on single crystals, to understand the effect of irradiation on the phase, and samples with a buffer layer, to verify whether the presence of the latter intervened in the modification of the properties.

- **Protons**: Several samples on different substrates were irradiated with protons having different energies. The protons, regardless of their energy, pass through the superconducting film and implant themselves in the substrate; the lower their energy, the closer they are to the interface. This has the greatest effect on the transport properties. In fact, the implantation of protons in the substrate modifies the strain the film is subjected to: the more the damaged substrate induces a strain in the film the more the superconducting properties are affected. The use of a buffer layer might help to accommodate the strain and therefore to enhance the radiation hardness of this material. However, both types of samples demonstrated that this material is very resistant to proton irradiation, much more than YBCO, for example.

- **Au ions**: The films were irradiated with high-energy gold ions (250 MeV), which create correlated defects (that tend to become columnar defects as the energy and mass of the ions increase) in the areas crossed by the ions. The introduction of these defects in films deposited on a single crystal degrades the superconducting properties: both the temperature and the critical current. The higher the dose, the greater the degradation. When samples deposited on a buffer layer are irradiated with gold ions, a different effect is observed. In particular, at low doses, we noticed a narrowing of the superconducting transition (i.e. a decrease in ΔT_c) and an increase in the critical current density. As the dose increases, the critical current density tends to decrease. Another significant effect of this irradiation is a reduction in the anisotropy of the samples and an improvement in the behaviour of the critical current density in applied field. Again, the presence of the buffer layer leads to a different behaviour of the irradiated samples.

- **Neutrons**: We irradiated samples deposited with and without buffer layers with fast monochromatic neutrons of energy 14.1 MeV. No differences were observed in the properties of the samples before and after irradiation. This is certainly encouraging, although we must bear in mind that the dose received by the samples was very low. To guarantee the use of a material in a fusion environment, it is necessary to guarantee its survival for at least ten years. The doses obtained in this case are orders of magnitude lower than those calculated for ten years of operation of a tokamak. Therefore, these evaluations are not conclusive to guarantee the usability of this material in fusion power plants.

Future perspectives

We have obtained superconducting films deposited on metal templates, demonstrating the feasibility of a simple home-made Fe(Se,Te)-coated conductor. This is a great result, but more can be done. In particular, neither the critical temperature nor the critical current density are as high as for films deposited on single crystals. This means that there is still room for improvement and we must try to further optimise these types of samples.

It has been shown that the maximum achievable J_c value is 30% of the depairing current density J_d. For Fe(Se,Te) we are very far from 30 %, so it is possible to increase the value of the critical current density of the phase, for example by introducing artificial pinning, which can occur with appropriate types of irradiation, or by doping. During my fellowship at Shibaura Institute of Technology, I began a study of phase doping using both $BaZrO_3$ (following what has been done in the literature for both YBCO and Ba-122) and carbon nanopearls. This work is still in progress.

Regarding the irradiation study of Fe(Se,Te) films, not much literature was available before the start of this work. During this thesis, in collaboration with the PRIN Hibiscus project and the JRA between ENI and CNR, many irradiation experiments have been carried out with different particles, different energies and different substrates, providing a large amount of data on a subject that has been little studied until now.

Further analysis of the effects of irradiation with Au ions in the presence of the buffer layer is necessary to understand the reason for the critical current increases, in addition to the narrowing of the superconducting transition. For example, deep TEM characterisations are planned at the CNR IMM Institute to study the effects of irradiation on the structure of film, buffer and substrate. The characterisation of these samples will continue, trying to analyse other properties in order to obtain further information on the effects that the irradiation may have produced. Furthermore, in order to confirm these results, a second irradiation was carried out by the Politecnico di Torino with 250 MeV gold ions, at doses both lower and higher than those analysed. All these samples will be soon measured.

Irradiations with protons and gold ions have shown how much the substrate determines the effects experienced by the superconductor, so it is very important to study the irradiation on samples deposited on metallic templates. In this respect, a sample has been irradiated with protons of energy 3.5 MeV. In the future, other types of irradiation on this type of sample will be done.

Finally, to verify the possible use of this material for fusion power plants, we need to achieve a sufficient dose of fast neutrons to simulate ten years of plasma irradiation.

The results so far are very promising. It has been possible to produce simple coated conductors of Fe(Se,Te) using methods that are both industrially

scalable and cost-effective. In addition, the radiation hardness of these materials has been successfully tested and they appear to be very resistant to different types of radiation.

Chapter 7

Appendix A

Third Harmonic Analysis

Following G. Lamura *et. al.* [86], we implemented a system to analyse superconducting films measuring the third harmonic response. The temperature behaviour of the first critical field B_{C1} of superconducting thin films can be determined using an inductive and contact-less method. Driving a sinusoidal current in a single coil placed in front of the sample, a non-zero third harmonic voltage V_3 is induced in it when Abrikosov vortices enter the sample. This method has been also proposed to determine the irreversibility line T_{irr}.

As a general feature, the generation of odd harmonics is predicted by the Bean critical state model [87]. Let's consider an ac magnetic field of amplitude h and frequency f generated by a far source is applied to a superconducting infinite cylinder with the main axis parallel to the field direction. As h equals $H_{C1}(T)$, vortices start to penetrate into the superconductor. Under these conditions, a non-linear power law $J \propto E^n$ in the current-voltage curve applies. As a consequence, odd harmonic components are produced in the spectrum of the sample response signal, when it enteres into a region of field and temperature in the magnetic phase diagram delimited by $B_{C1}(T)$ and the irreversibility field $B_{irr}(T)$. In the Bean limit, V_3 is predicted to be proportional to $V_3 \propto h^2 f/J_c$. By increasing the temperature in the superconducting state at fixed h and f, V_3 presents a maximum related to the Bean's critical field H^*.

$V_3(T)$ is strictly equal to zero in the Meissner phase, assumes values different from zero with a bell-shape behaviour in the mixed state below the irreversibilty line, and it is again equal to zero in the flux flow and normal state regimes. The shape of the peak can be used to state the quality of the sample. Figure 7.1(a) presents the third harmonic temperature behaviour respect to a generic superconducting phase diagram. The right onset of the third harmonic peak is ascribed to the irreversibility temperature.

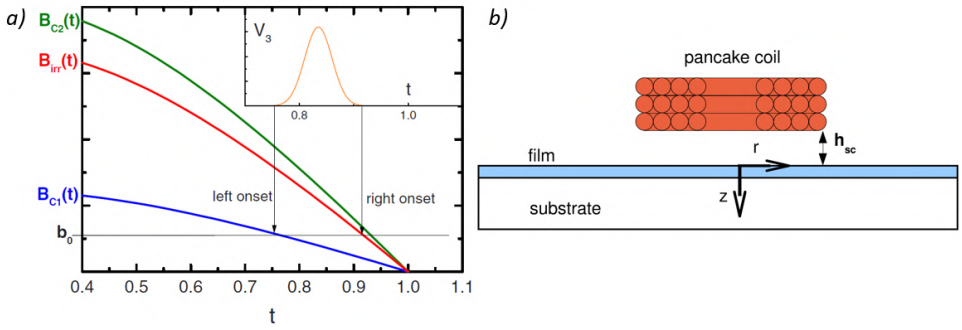

Fig. 7.1: (a) $V_3(T)$ behaviour for an ac magnetic field of amplitude $b_0 = h_0/\mu_0$ for a generic type II superconductor; (b) details of the coil-sample configuration. [86]

A sinusoidal current, the reference signal of a lock-in, is amplified and measured by using a high precision resistor. This signal is injected in a pancake coil located at the end of a cryogenic insert. The sample is placed in front of the coil at fixed distance. Figure 7.1(b) shows a cross-section of the sample.coil configuration. The output signal is filtered by using a low noise filter to reduce the first harmonic component and to avoid any saturation of the lock-in for a better signal-to-noise ratio during third harmonic detection [86].

Bibliography

[1] Kamihara, J. AM. CHEM. SOC. 2006, 128, 10012

[2] Shafranov V"On the history of the research into controlled thermonuclear fusion" J. Russ. Acad. Sci. 44 835–65 2001

[3] https://www.iter.org/

[4] https://alltheworldstokamaks.wordpress.com/gallery-of-external-views/t7/).

[5] Neil Mitchell, Jinxing Zheng, Christian Vorpahl, Valentina Corato, Charlie Sanabria, Michael Segal, Brandon Sorbom, Robert Slade, Greg Brittles, Rod Bateman, Yasuyuki Miyoshi, Nobuya Banno, Kazuyoshi Saito, Anna Kario, Herman Ten Kate, Pierluigi Bruzzone, Rainer Wesche, Thierry Schild, Nikolay Bykovskiy, Alexey Dudarev, Matthias Mentink, Franco Julio Mangiarotti, Kamil Sedlak, David Evans, Danko C Van Der Laan, Jeremy D Weiss, Min Liao Gen Liu "Superconductors for fusion: a roadmap" Supercond. Sci. Technol. 34 103001 (2021)

[6] https://www.fusionenergybase.com/article/measuring-progress-in-fusion-energy-the-triple-products

[7] https://qz.com/1402282/in-search-of-clean-energy-investments-in-nuclear-fusion-startups-are-heating-up

[8] W Iliffe, N Peng, G Brittles, R Batema, R Webb, C Grovenor S Speller "*In-situ* measurements of the effect of radiation damage on the superconducting properties of coated conductors" Supercond. Sci. Technol. 34 09LT01 (2021)

[9] S. Speller Materials Short Courses at 16^{th} European Conference on Applied Superconductivity EUCAS2023

[10] Chao Yao, Yanwei Ma "Superconducting materials: Challenges and opportunities for large-scale applications" iScience 24, 102541 (2021)

[11] Pierluigi Bruzzone, Walter H. Fietz, Joseph V. Minervini, Mikhail Novikov, Nagato Yanagi, Yuhu Zhai and Jinxing Zheng "High temperature superconductors for fusion magnets" Nucl. Fusion 58 103001 (2018)

[12] A Gurevich "Challenges and Opportunities for Applications of Unconventional Superconductors" Annu. Rev. Condens. Matter Phys. (2014)

[13] J Hänisch , K Iida , R Hühne C Tarantini "Fe-based superconducting thin films— preparation and tuning of superconducting properties" Supercond. Sci. Technol. 32 093001 (2019)

[14] H. Hosono, et al. "Recent advances in iron-based superconductors toward applications", Materials Today, Volume 21, Issue 3,2018, https://doi.org/10.1016/j.mattod.2017.09.006.

[15] Igor I. Mazin "Superconductivity gets an iron boost" NATURE|Vol 464|11 March 2010

[16] E. Sarnelli, M. Adamo, C. Nappi, V. Braccini, S. Kawale, E. Bellingeri, and C. Ferdeghini, "Properties of high-angle Fe(Se,Te) bicrystal grain boundary junctions," Appl. Phys. Lett. 104, 162601 (2014).

[17] E. Sarnelli, C. Nappi, C. Camerlingo, E. Enrico, E. Bellingeri, S. Kawale, V. Braccini, A. Leveratto, and C. Ferdeghini, "Properties of Fe(Se,Te) bicrystal grain boundary junctions, SQUIDs, and nanostrips," IEEE Trans. Appl. Supercond. 27, 7400104 (2017).

[18] J Hänisch and K Iida, "Grain Boundaries in Fe-based Superconductors" in P. Mele et al., "Superconductivity", Springer Nature 2020

[19] Hilgenkamp, H. and Mannhart, "J. Grain boundaries in high-Tc superconductors" Rev. Mod. Phys. 74, 485-549 (2002).

[20] Yanwei Ma, Invited EUCAS2019

[21] T. Taen, Y. Tsuchiya, Y. Nakajima, and T. Tamegai "Superconductivity at $T_C \sim 14K$ in single-crystalline $FeTe_{0.61}Se_{0.39}$", Physical Review B 80, 0925022 (2009)

[22] S. C. Wimbush, Flux Pinning in Applied Superconductivity Handbook on Devices and Applications (WILEY, 2015), Chap. 1, pp. 85–87.

[23] K. Iida, J. Hänisch, C. Tarantini "Fe-based superconducting thin films on metallic substrates: Growth, characteristics, and relevant properties", Applied Physics Reviews 5, 031304 (2018), https://doi.org/10.1063/1.5032258

[24] M. Miura, B. Maiorov, T. Kato, T. Shimode, K. Wada, S. Adachi, and K. Tanabe, "Strongly enhanced flux pinning in one-step deposition of $BaFe_2(As_{0.66}P_{0.33})_2$ superconductor films with uniformly dispersed $BaZrO_3$ nanoparticles," Nat. Commun. 4, 2499 (2013).

[25] M. Palombo, A. Malagoli, M. Pani C. Bernini, P. Manfrinetti, A. Palenzona, M. Putti "Exploring the feasibility of Fe(Se,Te) conductors by ex-situ powder-in-tube method" J. Appl. Phys. 117, 213903 (2015)

[26] G Sylva, A Augieri, A Mancini, A Rufoloni, A Vannozzi, G Celentano, E Bellingeri, C Ferdeghini, M Putti and V Braccini "Fe(Se,Te) coated conductors deposited on simple rolling-assisted biaxially textured substrate templates", Supercond. Sci. Technol. 32 084006 (2019)

[27] G Sylva, E Bellingeri, C Bernini, G Celentano, C Ferdeghini, A Leveratto, M Lisitskiy, A Malagoli, N Manca, A Mancini, P Manfrinetti, I Pallecchi, A Provino, M Putti, A Vannozzi and V Braccini "The role of texturing and thickness of oxide buffer layers in the superconducting properties of Fe(Se,Te) Coated Conductors", Supercond. Sci. Technol. 33 114002 (2020)

[28] A Palenzona et al, "A new approach for improving global critical current density in $Fe(Se_{0.5}Te_{0.5})$ polycrystalline materials" 2012 Supercond. Sci. Technol. 25 115018

[29] E. Sarnelli, C. Nappi, C. Camerlingo, E. Enrico, E. Bellingeri, V. Braccini, A. Leveratto, C. Ferdeghini "Fabrication and characterization of Fe(Se,Te) Josephson devices and nanostrips", 2017 16th International

Superconductive Electronics Conference (ISEC), Naples, Italy, 2017, pp. 1-3, doi: 10.1109/ISEC.2017.8314210.

[30] E Bellingeri, R Buzio, A Gerbi, D Marrè, S Congiu, M R Cimberle, M Tropeano, A S Siri, A Palenzona and C Ferdeghini "High quality epitaxial $FeSe_{0.5}Te_{0.5}$ thin films grown on $SrTiO_3$ substrates by pulsed laser deposition", Supercond. Sci. Technol. 22 105007 (2009)

[31] E. Bellingeri, I. Pallecchi, R. Buzio, A. Gerbi, D. Marrè, M. R. Cimberle, M. Tropeano, M. Putti, A. Palenzona, and C. Ferdeghini "$T_C = 21K$ in epitaxial $FeSe_{0.5}Te_{0.5}$ thin films with biaxial compressive strain", Appl. Phys. Lett. 96, 102512 (2010); https://doi.org/10.1063/1.3358148

[32] E Bellingeri, S Kawale, V Braccini, R Buzio, A Gerbi, A Martinelli, M Putti, I Pallecchi, G Balestrino, A Tebano and C Ferdeghini "Tuning of the superconducting properties of $FeSe_{0.5}Te_{0.5}$ thin films through the substrate effect", Supercond. Sci. Technol. 25 084022 (2012)

[33] S. Kawale, E. Bellingeri, V. Braccini, I. Pallecchi, M. Putti, G.Grimaldi, A. Leo, A. Guarino, A. Nigro, C. Ferdeghini "Comparison of Superconducting Properties of $FeSe_{0.5}Te_{0.5}$ Thin Films Grown on Different Substrates", IEEE TRANSACTIONS ON APPLIED SUPERCONDUCTIVITY, VOL. 23, NO. 3, (2013))

[34] V. Braccini, S. Kawale, E. Reich, E. Bellingeri, L. Pellegrino, A. Sala, M. Putti, K. Higashikawa, T. Kiss, B. Holzapfel, C. Ferdeghini "Highly effective and isotropic pinning in epitaxial Fe(Se,Te) thin films grown on CaF_2 substrates", Appl. Phys. Lett. 103, 172601 (2013) https://doi.org/10.1063/1.4826677

[35] M. Scuderi, I. Pallecchi, A. Leo, A. Nigro, G. Grimaldi C. Ferdeghini, C. Spinella, M. Guidolin, A. Trotta, V. Braccini "Nanoscale analysis of superconducting Fe(Se,Te) epitaxial thin films and relationship with pinning properties" Scientific Reports, (2021) 11:20100, https://doi.org/10.1038/s41598-021-99574-5

[36] Dew-Hughes, D. Flux pinning mechanisms in type II superconductors. Philos. Mag. 30, 293–305 (1974).

[37] S. Kawale, E. Bellingeri, V. Braccini, R. Buzio, A. Gerbi, A. Sala, E. Reich, B. Holzapfel, M. Adamo, E. Sarnelli, C. Tarantini, M. Putti, and C. Ferdeghini "Potentiality for Low Temperature—High Field Application of Iron Chalcogenide Thin Films", IEEE TRANSACTIONS ON APPLIED SUPERCONDUCTIVITY, VOL. 25, NO. 3, (2015)

[38] J. L. MacManus- Driscoll, S. C. Wimbush "Processing and application of high-temperature superconducting coated conductors" Nat. Rev. Mater 6, 587–604 (2021)

[39] A Palenzona, A Sala, C Bernini, V Braccini, M R Cimberle, C Ferdeghini, G Lamura, A Martinelli, I Pallecchi, G Romano, M Tropeano, R Fittipaldi, A Vecchione, A Polyanskii, F Kametani, M Putti "A new approach for improving global critical current density in $Fe(Se_{0.5}, Te_{0.5})$ polycrystalline materials", Supercond. Sci. Technol. 25 115018 (2012)

[40] O Guillon,J Gonzalez-Julian, B Dargatz,T Kessel, G Schierning, J Rathel and M Herrmann "Field-Assisted Sintering Technology/Spark Plasma Sintering: Mechanisms,Materials, and TechnologyDevelopments", ADVANCED ENGINEERING MATERIALS,16, No. 7 (2014) 10.1002/adem.201300409

[41] G Sylva, E Bellingeri, C Ferdeghini, A Martinelli, I Pallecchi, L Pellegrino, M Putti, G Ghigo, L Gozzelino, D Torsello, G Grimaldi, A Leo, A Nigro and V Braccini "Effects of high-energy proton irradiation on the superconducting properties of Fe(Se,Te) thin films" Supercond. Sci. Technol. 31 054001 (2018)

[42] S. Molatta, S. Haindl, S. Trommler, M. Schulze, S. Wurmehl, and R. H¨uhne, "Interface control by homoepitaxial growth in pulsed laser deposited iron chalcogenide thin films," Sci. Rep., vol. 5, 2015, Art. no. 16334

[43] L. Piperno, A. Vannozzi, V. Pinto, A. Augieri, A. Angisani Armenio, F. Rizzo, A. Mancini, A. Rufoloni, G. Celentano, V. Braccini, M. Cialone, M. Iebole, N. Manca, A. Martinelli, M. Putti, G. Sotgiu, and A. Meledin "Chemical CeO_2-Based Buffer Layers for Fe(Se,Te) Films",

IEEE TRANSACTIONS ON APPLIED SUPERCONDUCTIVITY, VOL. 32, NO. 4, (2022)

[44] A Vannozzi, S Prili, G Sylva, A Masi, A Angrisani Armenio, A Mancini, V Pinto, A Rufoloni, L Piperno, A Augieri, F Rizzo, P Manfrinetti, V Braccini, M Putti, E Silva and G Celentano "Epitaxial Zr-doped CeO_2 films by chemical solution deposition as buffer layers for Fe(Se,Te) film growth", Supercond. Sci. Technol. 33 084004 (2020)

[45] G Sylva, A Malagoli, E Bellingeri, M Putti, C Ferdeghini, A Vannozzi, G Celentano, S C Hopkins, A Lunt, A Ballarino, V Braccini "Analysis of Fe(Se,Te) Films Deposited On Unbuffered Invar 36" IEEE TRANSACTIONS ON APPLIED SUPERCONDUCTIVITY, VOL. 29, NO. 5, (2019)

[46] A. Vannozzi, L. Piperno, A. Rufoloni, S. Botti, F. Bonfigli, M. Iebole, L. Savio, M. Cialone, A. Masi, A. Mancini, A. Augieri, G. Celentano, V. Braccini, M. Putti "Zr:CeO_2 buffer by CSD on Ni-W substrate for low-cost Fe(Se,Te) coated conductor", Accepted IEEE Transactions on Applied Superconductivity

[47] https://srdata.nist.gov/xps/

[48] https://scripts.iucr.org/cgi-bin/paper?S0021889810030499

[49] J. Shi, D. L. Allara "Characterization of High-Temperature Reactions at the BaO/W Interface" Langmuir 1996, 12, 21, 5099–5108 https://doi.org/10.1021/la960196+

[50] T. Skála and V. Matolín, "Model thin films of Ce(III)-based mixed oxides," Surface and Interface Analysis, vol. 46, no. 10–11, pp. 993–996, Oct. 2014, doi: 10.1002/SIA.5458

[51] Y. Polyak and Z. Bastl, "XPS and factor analysis study of initial stages of cerium oxide growth on polycrystalline tungsten," Surface and Interface Analysis, vol. 47, no. 6, pp. 663–671, Jun. 2015, doi: 10.1002/SIA.5762

[52] T. Skála, N. Tsud, K. C. Prince, and V. Matolín, "Interaction of tungsten with CeO2(111) layers as a function of temperature: a

photoelectron spectroscopy study," Journal of Physics: Condensed Matter, vol. 23, no. 21, p. 215001, May 2011, doi: 10.1088/0953-8984/23/21/215001

[53] Salvati, L. Jr., Makovsky, L.E., Stencel, J.M., Brown, F.R., Hercules, D.M. "Surface spectroscopic study of tungsten-alumina catalysts using x-ray photoelectron, ion scattering, and Raman spectroscopies", Journal of Physical Chemistry, 85(24), 3700-3707 (Nov 1981)

[54] 10.1016/j.apsusc.2018.04.077

[55] https://www.enginsoft.com/expertise/reshaping-the-demo-tokamak%E2%80%99s-tf-coil-with-high-fidelity-multiphysics-cae-and-advanced-mesh-morphing.html

[56] Ghigo G., Ummarino G.A., Gozzelino L. et al. "Effects of disorder induced by heavy-ion irradiation on $(Ba_{1x}K_x)Fe_2As_2$ single crystals, within the three-band Eliashberg s± wave model" Sci Rep 7, 13029 (2017).

[57] M. Eisterer, "Radiation effects on iron-based superconductors," Supercond. Sci. Technol. 31, 013001 (2018).

[58] M. Leroux, K. J. Kihlstrom, S. Holleis, M. W. Rupich, S. Sathyamurthy, S. Fleshler, H. P. Sheng, D. J. Miller, S. Eley, L. Civale, A. Kayani, P. M. Niraula, U. Welp, W.-K. Kwok "Rapid doubling of the critical current of $YBa_2Cu_3O_{7-d}$ coated conductors for viable high-speed industrial processing" APPLIED PHYSICS LETTERS 107, 192601 (2015)

[59] M. Putti, M. Affronte, C. Ferdeghini, P. Manfrinetti, C. Tarantini, E. Lehmann "Observation of the Crossover from Two-Gap to Single-Gap Superconductivity through Specific Heat Measurements in Neutron-Irradiated MgB_2" PRL 96, 077003 (2006)

[60] M. B. Schilling, A. Baumgartner, B. Gorshunov, E. S. Zhukova, V. A. Dravin, K. V. Mitsen, D. V. Efremov, O. V. Dolgov, K. Iida, M. Dressel, S. Zapf "Tracing the s_{+-} symmetry in iron pnictides by controlled disorder" Phys. Rev. B 93 174515 (2016)

[61] M. Putti, P. Brotto, M. Monni, E. Galleani d'Agliano, A. Sanna, S. Massidda "Intraband vs. interband scattering rate effects in neutron irradiated MgB_2" 2007 EPL 77 57005

[62] N. W. Salovich, Hyunsoo Kim, Ajay K. Ghosh, R. W. Giannetta, W. Kwok, U. Welp, B. Shen, S. Zhu, H.-H. Wen, M. A. Tanatar, R. Prozorov "Effect of heavy-ion irradiation on superconductivity in $Ba_{0.6}K_{0.4}Fe_2As_2$" Phys. Rev. B 87, 180502(R) (2013)

[63] Toshinori Ozaki, Lijun Wu, Cheng Zhang, Jan Jaroszynski, Weidong Si, Juan Zhou, Yimei Zhu Qiang Li "A route for a strong increase of critical current in nanostrained iron-based superconductors" Nat. Commun. 7 13036 (2016)

[64] R Flükiger, T Spina, F Cerutti, A Ballarino, C Scheuerlein, L Bottura, Y Zubavichus, A Ryazanov, R D Svetogovov, S Shavkin, P Degtyarenko, Y Semenov, C Senatore R Cerny "ariation of Tc, lattice parameter and atomic ordering in Nb3Sn platelets irradiated with 12 MeV protons: correlation with the number of induced Frenkel defects" Supercond. Sci. Technol. 30 054003 (2017)

[65] A Leo, G Sylva, V Braccini, E Bellingeri, A Martinelli, I Pallecchi, C Ferdeghini, L Pellegrino, M Putti, G Ghigo, L Gozzelino, D Torsello, S Pace, A Nigro, G Grimaldi "Anisotropic Effect of Proton Irradiation on Pinning Properties of Fe(Se,Te) Thin Films" IEEE TRANSACTIONS ON APPLIED SUPERCONDUCTIVITY, VOL. 29, NO. 5, (2019)

[66] A Leo, G Grimaldi, A Nigro, G Ghigo, L Gozzelino, D Torsello, V Braccini, G Sylva, C Ferdeghini, M Putti "Critical current anisotropy in Fe(Se,Te) flms irradiated by 3.5 MeV protons" J. Phys.: Conf. Ser. 1559 012042 (2020)

[67] T Ozaki, T Kashihara, I Kakeya R Ishigami "Effect of 1.5 MeV Proton Irradiation on Superconductivity in $FeSe_{0.5}Te_{0.5}$ Thin Films" Quantum Beam Sci. 2021, 5, 18.

[68] P. W. Anderson "THEORY OF DIRTY SUPERCONDUCTORS" J. Phys. Chm. Solids Pergamon Press Vol. Il. pp. 26-30. (1959)

[69] T Ozaki, L Wu, C Zhang, W Si, Q Jie Q Li "Enhanced critical current in superconducting $FeSe_{0.5}Te_{0.5}$ films at all magnetic field orientations by scalable gold ion irradiation" Supercond. Sci. Technol. 31 024002 (2018)

[70] D Torsello, L Gozzelino, R Gerbaldo, T Tamegai G Ghigo "Scaling laws for ion irradiation effects in iron-based superconductors" Scientific Reports | (2021) 11:5818

[71] D Torsello, R Gerbaldo, L Gozzelino, F Laviano, A Takahashi, A Park, S Pyon, A Ichinose, T Tamegai G Ghigo "Twofold role of columnar defects in iron based superconductors" Supercond. Sci. Technol. 33 (2020) 094012

[72] D. Daghero, M. Tortello, L. Gozzelino, R.S. Gonnelli, T. Hatano, T. Kawaguchi, H. Ikuta "Effect of ion irradiation on surface morphology and superconductivity of $BaFe_2(As_{1-x}P_x)_2$ films" Applied Surface Science 395 (2017) 9-15

[73] D Daghero, M Tortello, G A Ummarino, E Piatti, G Ghigo, T Hatano, T Kawaguchi, H Ikuta R S Gonnelli "Decoupling of critical temperature and superconducting gaps in irradiated films of a Fe-based superconductor" 2018 Supercond. Sci. Technol. 31 034005

[74] F Massee, P O Sprau, Y Wang, J. C. Séamus Davis, G Ghigo, G Gu, W Kwok "Imaging atomic-scale effects of high-energy ion irradiation on superconductivity and vortex pinning in Fe(Se,Te)" Sci. Adv. 2015;1:e1500033

[75] T Ozaki, L Wu, C Zhang, W Si, Q Jie, Q Li "Enhanced critical current in superconducting $FeSe_{0.5}Te_{0.5}$ films at all magnetic field orientations by scalable gold ion irradiation" 2018 Supercond. Sci. Technol. 31 024002

[76] T Ozaki, L Wu, G Gu, Q Li "Ion irradiation of iron chalcogenide superconducting films" 2020 Supercond. Sci. Technol. 33 094008

[77] MEisterer, R Raunicher, H WWeber, E Bellingeri, M R Cimberle, I Pallecchi, M Putti, C Ferdeghini "Anisotropic critical currents in

$FeSe_{0.5}Te_{0.5}$ films and the influence of neutron irradiation" Supercond. Sci. Technol. 24 065016 (2011)

[78] J. F. Ziegler et al., "SRIM - The stopping and range of ions in matter"Nucl. Instrum. Methods Phys. Res. Section B: Beam Interact. Mater. Atoms, vol. 268, no. 11-12, pp. 1818–1823, 2010

[79] D Torsello, M Fracasso, R Gerbaldo, G Ghigo, F Laviano, A Napolitano, M Iebole, M Cialone, N Manca, A Martinelli, L Piperno, V Braccini, A Leo, G Grimaldi, A Vannozzi, G Celentano, M Putti, L Gozzelino "Proton Irradiation Effects on the Superconducting Properties of Fe(Se,Te) Thin Films" IEEE TRANSACTIONS ON APPLIED SUPERCONDUCTIVITY, VOL. 32, NO. 4, JUNE 2022

[80] L Gozzelino, D Botta, R Cherubini, A Chiodoni, R Gerbaldo, G Ghigo, F Laviano, B Minetti, E Mezzetti "Magneto-optical analysis of the critical current density dependence on temperature in proton irradiated YBCO films" 2004 Supercond. Sci. Technol. 17 S500

[81] Stoller, R. E. ; Toloczko, M. B. ; Was, G. S. ; Certain, A. G. ; Dwaraknath, S. ; Garner, F. A. "On the use of SRIM for computing radiation damage exposure," Nucl. Instrum. Meth. B, vol. 310, pp. 75–80, Sep. 2013

[82] J. I. Langford et al., "Applications of total pattern fitting to a study of crystallite size and strain in zinc oxide powder," Powder Diffraction, vol. 1, no. 3, pp. 211–221, Sep. 1986.

[83] L. E. Helseth, A. G. Solovyev, R. W. Hansen, E. I. Il'yashenko, M. Baziljevich, and T. H. Johansen "Faraday rotation and sensitivity of (100) bismuthsubstituted ferrite garnet films," Phys. Rev. B, vol. 66, no. 6, Aug. 2002, Art. no. 0 64405

[84] https://www.ga.com/triga/

[85] A. Pietropaolo, F. Andreoli, M. Angelone, U. Besi Vetrella, S. Fiore, S. Loreti, G. Pagano, R. Pilotti, M. Pillon "The Frascati Neutron Generator: A multipurpose facility for physics and engineering" J. Phys.: Conf. Ser. 1021 012004 (2018)

[86] G. Lamura, M. Aurino, A. Andreone, J.-C. Villégier "First critical field measurements of superconducting films by third harmonic analysis" J. Appl. Phys. 106, 053903 (2009

[87] C. P. Bean, Rev. Mod. Phys. 36, 31 (1964)